UNDERSTANDING THE ELECTRICAL RESPONSE TO APPLIED STRAIN OF POLYMER SUPPORTED SCREEN PRINTED INKS

A Dissertation
Presented to
The Academic Faculty

by

Gabriel Cahn

In Partial Fulfillment
of the Requirements for the Degree
Doctor of Philosophy in the
George W. Woodruff School of Mechanical Engineering

Georgia Institute of Technology
August 2021

UNDERSTANDING THE ELECTRICAL RESPONSE TO APPLIED STRAIN OF POLYMER SUPPORTED SCREEN PRINTED INKS

Approved by:

Dr. Olivier N. Pierron, Advisor
George W. Woodruff School of Mechanical Engineering
Georgia Institute of Technology

Dr. Suresh Sitaraman
George W. Woodruff School of Mechanical Engineering
Georgia Institute of Technology

Dr. Antonia Antoniou, Advisor
George W. Woodruff School of Mechanical Engineering
Georgia Institute of Technology

Dr. Meisha Shofner
School of Materials Science and Engineering
Georgia Institute of Technology

Dr. Samuel Graham
George W. Woodruff School of Mechanical Engineering
Georgia Institute of Technology

Date Approved: May 25, 2021

To my family

ACKNOWLEDGEMENTS

This PhD represents years of dedicated effort, over which I have grown as a person, as a researcher, and as a contributing member to the scientific community. While I have maintained a strong intrinsic motivation to do good work, I owe special thanks to my advisors, who have provided endless support and encouragement. To Dr. Olivier Pierron, for pushing me to think critically through challenging engineering problems, ask the right questions, and shake off pesky presentation habits that I had picked up from working in industry. He has been an excellent teacher, both inside and outside of the classroom. To Dr. Antonia Antoniou, for introducing new analytical techniques that enriched my research findings, and for her boundless positivity. And to Dr. Samuel Graham, who welcomed me into his research group "family," and supported me from my first days at Georgia Tech, through shortfalls in funding, all while simultaneously chairing the entire mechanical engineering department. I hold him as an example of the kind of leadership I aspire to portray.

I would also like to extend my gratitude to my other committee members, Dr. Suresh Sitaraman and Dr. Meisha Shofner, for supporting my PhD development. Dr. Sitaraman not only led the initial Nextflex research efforts, which served as a foundation for my work, but also opened up his lab tools and resources to help keep my experiments moving forward. Some of my closest research colleagues have come out of collaborating with his group, and I truly appreciate the mentorship he has provided over the years.

I want to thank the members of the Graham, Pierron, and Sitaraman research groups, past and present, for making this PhD such a positive experience through shared

accomplishment and commiserations. Particular thanks go to Justin Chow, Ben Stewart, and Rui Chen for their collaborative partnership, Kyungjin Kim, Saurabh Gupta, and Alejandro Barrios for their mentorship, and Nick Hines, Jason Hirschey, and Sam Kim for making a shared office feel less cramped and more like the second home that it was.

I would like to thank the Marcus IEN staff, specifically Eric Woods and Mengkun Tian for their training and guidance in characterizing my composite materials, and especially for taking late night phone calls to help me troubleshoot the FIB tool. Thank you to Dr. W Hong Yeo and his lab for facilitating in-house screen printing of test samples on the back end of my research. Thank you, also, to Dr. Shannon Yee and his group for sharing their enthusiasm of science in regular group meetings.

Thanks to all of the new friends I have made since moving to Atlanta for this program: Danit, Mina, Matt, Will, John, Harper, Chelsea, Randy, Jeremy, Marissa, Rob, Holly, Harbor, Andre, Antonio, Sarrah, and many others. You have helped to keep my life healthy, well rounded, and fun.

Lastly, I want to wholeheartedly thank my entire family for their love and support. To my parents, Rob and Arlene, for unconditional patience and encouragement, and for constantly checking in on me, even when I did not want or need them to. To my brother, Dan, for keeping me in a big picture mindset, and for being one of the only people who did not say I was crazy for going back to school to get a PhD, even though I was.

TABLE OF CONTENTS

LIST OF TABLES

LIST OF FIGURES

LIST OF SYMBOLS AND ABBREVIATIONS

Abbreviations

FHE	Flexible Hybrid Electronics
TPU	Thermoplastic Polyurethane
PCB	Printed Circuit Boards
COS	Critical Onset Strain
FIB	Focused Ion Beam
SEM	Scanning Electron Microscopy/Microscope
PET	Polyethylene Terephthalate
PI	Polyimide
DIC	Digital Image Correlation
RBT	Rigid Body Transformation

Symbols

R	Resistance
ρ	Resistivity
L	Length
h	Cross sectional thickness
w	Nominal print width
A	Cross sectional area
$\varepsilon_M, \varepsilon_{app}$	Applied uniaxial strain
V	Total ink volume
φ	Conductive filler volume fraction
σ	Conductivity
F	Conductive filler packing fraction

t	Fitting Exponent
T, M	Screen threads per inch
d	Screen thread diameter
a	Screen thread rigidity coefficient
e	Emulsion thickness
C_a	Capillary number
H_{max}	Max printed thickness
F_{open}	Mesh aperture fractional open area

SUMMARY

Flexible hybrid electronics (FHE) is a classification of assemblies that describes rigid component islands bridged by interconnects printed onto compliant polymer substrates. They boast continued performance integrity in cases that require repeated elongation, including repeated stretching. The last 20 years have demonstrated exponential growth in the application of such designs in industries such as healthcare, energy harvesting, and smart home systems, driving the need for high volume, low cost, manufacturing approaches. Screen printing composite materials such as polymers with conductive particle inclusions offers electrical function with stretchability, but the performance limits of these materials have yet to be fully explored. This dissertation investigates the evolution of electrical performance of silver-filled polymer inks subjected to uniaxial strain.

This work begins by exploring conductivity of two inks with similar flake volume fractions of ~50% that are screen-printed with a single pass (thickness: 10 μm) onto three different polymer substrates. The normalized resistance increases more rapidly with applied strain for the flexible ink (5025 with an acrylic binder), and has three times greater resistance at 35% strain when compared to the stretchable ink (PE 874 with polyurethane binder). While resistance increase is qualitatively consistent with percolation theory, *in situ* strain map analysis and post-mortem fractography reveal drastic differences in the root causes of the inks' electrical behavior. Both inks form strain localization bands with similar spacing. For the flexible ink (5025), strain localization is accompanied by local necking and silver flake area fraction reduction. For the stretchable ink (PE 874), strain localization

is associated with surface cracking initiated by pre-existing voids, with minimal changes in the silver flake area fraction. A model incorporating strain localization through an evolving Gaussian distribution of flakes with applied strain more closely accounts for the 5025 ink's normalized resistance increase compared to models that assume uniform strain and a uniform flake distribution. Overall, local necking and reduction of the flake area fraction appear to be more detrimental to the resistance than the formation of surface cracks.

Expanding upon the discovery of surface cracks in PE 874, an investigation is made into the origins of electrical performance degradation under uniaxial stretching of a silver filled polyurethane ink (DuPont PE 874) screen printed onto a thermoplastic polyurethane (TPU) substrate. The ink develops surface ruptures at strains of only a few percent, yet remains conductive through continued elongation. It exhibits an increasing sensitivity to surface damage beyond 10% applied strain, ε_{app}, as the trace width, w, is reduced from 2 to 0.1 mm. This lowers the ε_{app} threshold for open circuit failure, from approximately 180% for w = 2 mm down to 25% for w = 0.1 mm. The damage progression remains largely consistent across trace widths: surface cracks coalesce to form longer channels, which grow perpendicular to the direction of elongation. These channels both deepen and widen with increasing ε_{app}, and some become laterally linked. The evolution of the network of interlinked channels is not width dependent, but a width effect manifests as a result of the channels constituting a larger fraction of specimen width for narrower traces. In addition, the narrower traces exhibit reduced cross-sections due to an edge taper – an artifact of the screen printing process – which attenuates deposition thickness by as much as 50% for w = 0.1 mm.

Fatigue response in filled polymers has so far remained largely unexplored, and is essential prior to using in health monitoring applications. PE 874 printed onto TE11C is evaluated under high-strain cycling. In-situ techniques, including 4-point resistance measurement and laser profilometry, are used to correlate changes in electrical performance to the fatigue response. Surface crack formation is extensive upon stretching during the first loading cycle, forming a heavily interconnected crack network at higher strains that does not immediately result in open circuit failure. Resistance increase with cycling is attributed to a gradual deepening of these cracks until their depths approach the film thickness, eventually leading to electrical failure. Fatigue life, the number of cycles required to reach a predetermined electrical performance limit, is shown to be most influenced by the applied strain amplitude. Using a normalized resistance increase limit of R/R_0=500, it is found that 500 μm wide conductive lines endure 23 cycles at 35% strain amplitude, but this becomes over 500 cycles when the amplitude is dropped to 5%. Sensitivity to mean strain, ε_m, is relevant to strain amplitudes below 15%. In this manner, a composite conductor was shown to exhibit crack evolution behavior distinctly different from homogeneous metallic films.

Finally, this dissertation presents modifications to traditional single-pass print processes in an effort to achieve different geometric and architectural outcomes. Existing models for predicting deposition thicknesses fail to capture the complexities of the array of process parameters. Void removal in PE 874 through vacuum, sonication, and calendering operations proved ineffective, suggesting a decrease in volume loading of silver may prevent a porous architecture.

CHAPTER 1. BACKGROUND AND MOTIVATION

1.1 Introduction and Motivation

Electronic devices are prevalent throughout personal and professional life activities; health and environmental monitoring [1, 2], communication [3], energy capture [4] and storage [5] are only a few of the numerous applications in regular use. As these product markets evolve, and new ones emerge, portability and cost reduction, as well as performance improvements are standard drivers for innovation. The potential of flexible designs to meet these needs has been recognized within the field as early as the 1960s [6]. However it has only been in the last 10-15 years when we have seen publications regarding flexible and stretchable electronics rising exponentially, as shown in Figure 1-1.

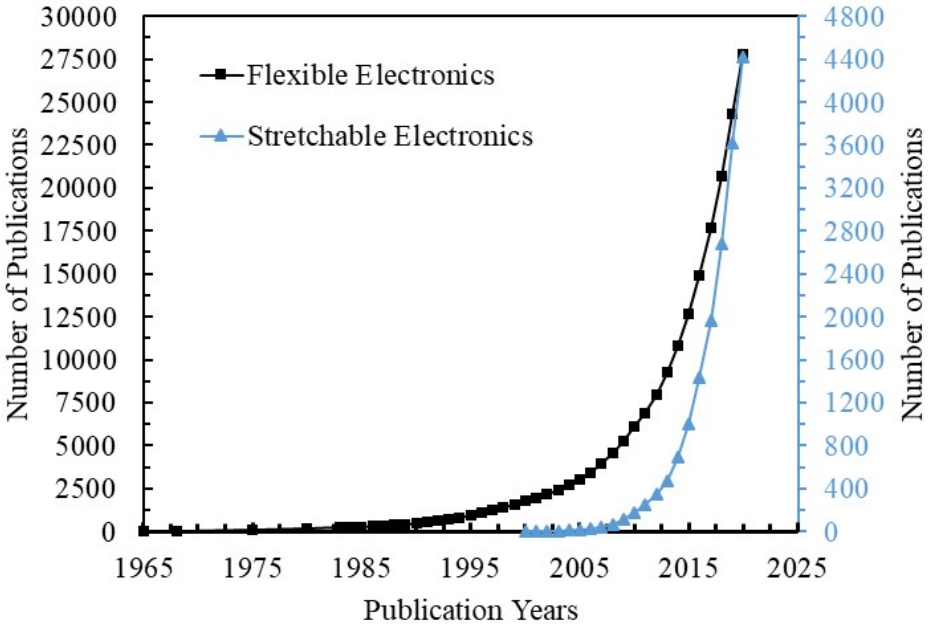

Figure 1-1: Accumulated publications on flexible and stretchable electronics from 1965-2020. Data was extracted from Web of science by use of keywords flexible electronics and stretchable electronics.

This has yielded promising results in foldable phones, smart watches, and a variety of wearable technology applications:

Figure 1-2: Summarized properties of advanced wearable FHE [7]

The critical discriminator between flexible electronics and traditional rigid printed circuit boards (PCB) is their ability to operate effectively after, and often during, exposure to high strain (for example, upwards of 30% and beyond for wearable applications). Several

types of compliant conductors [8] are in development to satisfy strain requirements, each with mechanical limitations.

Metals and carbons have shown promise when deposited as surface film coatings [9-11] onto, or embedded as nanowires [12-14] within, polymeric substrates to form conductive circuit traces. Such films have substantial elastic property mismatch with the substrate and often fail by cracking at low applied strains. Conductive polymers are also useful as films [15-17], and have even been functionalized for actuation [18-20], but may irreversibly deform and de-bond when elongated. More complex architectures are formed when metallic interconnect structures, such as micropillar arrays [21], serpentine lines [22], and buckled films [23], are attached to elastomers, however they are similarly susceptible to irreversible elongation and delamination from substrates. Finally, hybrid conductors describe when conductive filler particles are added to polymers [24-26]. At a certain threshold of filler volume fraction, these independent particles form a cohesive percolation network, across which current can flow. When strained, the conductor volume will initially increase. This phenomenon is relatively isolated to the polymer matrix, resulting in a decrease of conductor volume fraction, which may result in a decrease in conductivity with potential breakdown of the percolation network. Consequently, hybrid conductors with polymer matrices having large Poisson's ratio, ν, around 0.5, are expected to electrically perform better under strain.

FHE are an increasingly prevalent category of devices that describe combining CMOS-based chip components with circuitry printed onto flexible substrates such as polymers, paper, and textiles. In this manner, rigid component "islands" are bridged by compliant interconnects, most often metallic films or hybrid conductors. This represents a

low cost additively manufactured packaging scheme that is deployable with tunable properties in a myriad of ways.

To date, research in polymer supported FHEs has largely been limited to low-strain applications, due to the low critical onset strain (COS) of only a few percent for cracking in homogeneous metallic films. Hybrid conductors theoretically surpass metal films in strain tolerance, but little is known of the mechanical behaviors that govern reliability outside of the low-strain regime. Further research is required to link the architecture of polymer substrates and conductive composite ink makeup to electrical performance evolution under high applied strains.

1.2 Background Information

1.2.1 Monotonic Strain Effects on Electrical Performance of a Conductor

Connecting the observed increase in resistance with the relevant underlying physics is necessary to provide insight, and for enabling future material improvements. First order approximations and models are used to predict electrical performance in hybrid conductors that are subjected to applied strain. The change in resistance due to dimensional changes in a conductor under uniaxial stretch can be found by first using the well-known resistance relationship:

$$R_0 = \frac{\rho L_0}{A_0} \qquad \text{Equation 1.1}$$

where A_0 corresponds to the initial ink cross-sectional area, L_0 corresponds to the initial length and ρ is the material resistivity. For a printed ink trace:

$$A_0 = h_0 w_0 \qquad \text{Equation 1.2}$$

With h_0 corresponding to average ink height, and w_0 corresponding to the ink trace width. Under applied uniaxial strain, ε_M, the ink dimensions change and become:

$$L = L_0(1 + \varepsilon_M) \quad \text{Equation 1.3}$$

$$w = w_0(1 - \nu\varepsilon_M) \quad \text{Equation 1.4}$$

$$h = h_0(1 - \nu\varepsilon_M) \quad \text{Equation 1.5}$$

With L, w, and h denoting the deformed dimensions and ν denoting the Poisson's ratio for the ink. The resistance defined based on the new dimensions is:

$$R = \frac{\rho L}{A} \quad \text{Equation 1.6}$$

Normalizing this deformation-dependent value for relative comparison between experimental samples, and reducing terms, we find:

$$\frac{R}{R_0} = \frac{(1 + \varepsilon_M)}{(1 - \nu\varepsilon_M)^2} \quad \text{Equation 1.7}$$

Critically, this approximation assumes that resistivity of the conductive material remains constant through all values of applied strain.

1.2.2 Percolation Theory For Hybrid Conductors

For composite polymer inks containing conductive inclusions, the volume of the conductor is:

$$V = V_f + V_p \quad \text{Equation 1.8 [27]}$$

where V_f is the volume of the filler material, and V_p is the volume of the polymer matrix. Electrical conductivity of a percolating network of filler material is dependent upon a filler

volume fraction, φ. As the amount of filler increases relative to matrix material, the likelihood of electrical percolation increases, such that it reaches a critical volume content threshold, φ_c, and the composite becomes conductive, having conductivity σ_c at this onset of percolation. Further rise of the filler volume rapidly increases the conductivity, until it approximates close to the conductivity of the filler material itself, σ_m. This volume content dependence is described by Figure 1-3.

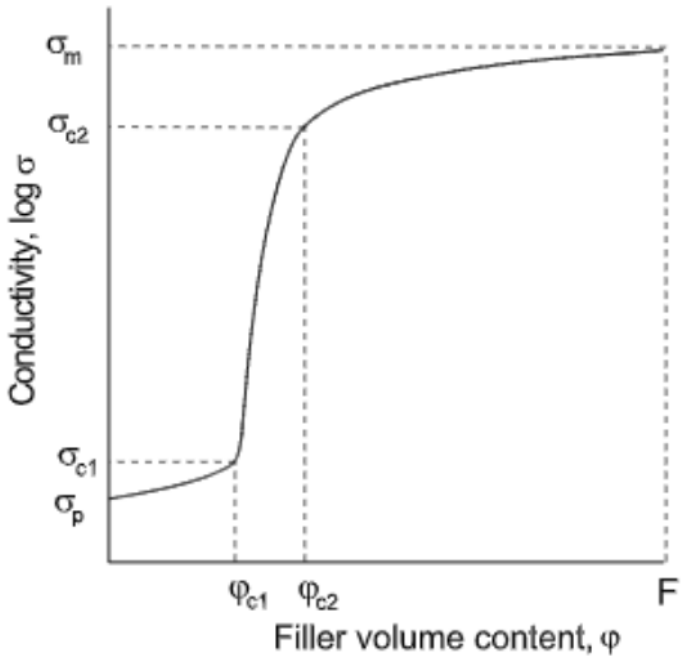

Figure 1-3: Typical dependence of electrical conductivity (logarithm) on conductive filler volume content [27]

In this model, σ_p is the conductivity of the polymer traditionally treated as near-zero. φ_{c1} and φ_{c2} describe the boundaries of the "smearing region" between which conductivity is especially sensitive to filler volume. σ_{c1} and σ_{c2} are the conductivity values associated with this region. F is the maximum packing limit possible for the filler particles, based on geometry, defined by:

$$F = \frac{V_f}{(V_f + V_p)}$$ Equation 1.9 [27]

Given these definitions, conductivity of a composite ink is susceptible to change by applied strain. First, we presume that the Poisson's ratio of the material is less than 0.5, otherwise volume would be conserved. This results in a Poisson effect, by which the conductor volume increases with strain. The conductive inclusions are treated as rigid bodies, while the polymer matrix is considered to be compliant material. As such, the increase in the conductor volume is attributed to the increase in volume of the polymer matrix, which leads to a decrease in the silver flake fraction and, subsequently, a decrease in the electrical conductivity. Therefore, as the strain increases, the conductivity decreases, and the resistance increases. For such models, spacial distribution of filler material is treated as uniform [27]. Ergo strain distribution is uniform, *i.e.*, there is no strain localization. To describe this affine transformation, the expressions for the electrical conductivity according to Mamunya [27] is:

$$\sigma = \sigma_c + (\sigma_m - \sigma_c)\left[\frac{\varphi - \varphi_c}{F - \varphi_c}\right]^t$$ Equation 1.10 [27]

where t represents a fitting exponent to accompany the other system parameters.

1.2.3 Polymer Supported Printed Conductive Inks

A common thread among many flexible solutions is the approach of additively manufacturing devices through techniques such as transfer, inkjet, aerosol, and screen-printing conductive films onto thin polymer substrates. Printing methods have shown great promise in their compatibility with inorganic materials for creating large field transistor arrays [28]. The maturity of the technology allows for high volume production,

compounding the cost and weight savings by drastically reducing the material consumed per unit print. Researchers are pushing the bounds of circuit density and complexity, but struggle with limitations of feature size in reliable designs. Trace widths have shown to be reliably produced by direct print at width resolutions of 100μm[29, 30], 10μm[31], and even 1μm [32]. Others have printed onto pre-strained substrates, achieving reduced trace widths and increased circuit density upon release [33].

It has long been known that free-standing metallic films are prone to rupture at strains below 1% [34]. The strain localization and necking behavior that causes such failure is attenuated when such films are supported by polymer substrates [35], as illustrated in Figure 1-4,

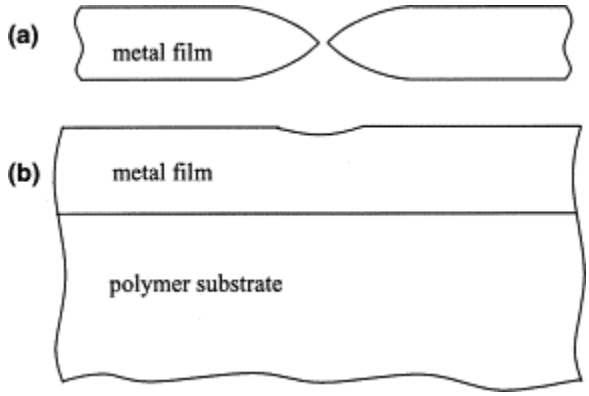

Figure 1-4: (a) Freestanding metal film, in which localization is accommodated by rigid body motion of the ruptured halves (b) Substrate-bonded film, in which local elongation may be suppressed by the substrate [35]

and can be further regulated by film/substrate adhesion [36, 37]. However, the strain delocalization benefit of compliant substrates is finite. One drawback of using thin metallic films as the conductor is their substantial elastic property mismatch with the polymer substrate, often leading to early degradation of the electrical behavior due to cracking [38-

48]. Most supported films rupture below 10% strain [49-51], with a few exceptions reaching 20% [52] and even 50% [53]. Printed design patterns can further increase assembly level stretchability by minimizing strain within the print lines [54, 55]. These conductors are therefore limited to bendable electronic applications, where the maximum strains do not exceed a few percent. Common applications for metal thin films include solar cells [56], energy harvesting devices [57], RFID antennas [58], health monitors [59], and other sensors [60-62].

1.2.4 Screen Printing Theories

Screen printing has been in use for hundreds of years, predominantly as an artistic technique, allowing for high rate printing at low costs. It constitutes the passing of viscous fluid (ink) through the apertures of a fine screen mesh – having been appropriately masked with the desired design – onto a substrate material of choice. This is accomplished by pressing and dragging a semi-rigid squeegee blade tip across the screen, thereby applying sheer force to a leading pool of ink, as illustrated in Figure 1-5. In more recent decades, the practice has been adopted for the production of electronics.

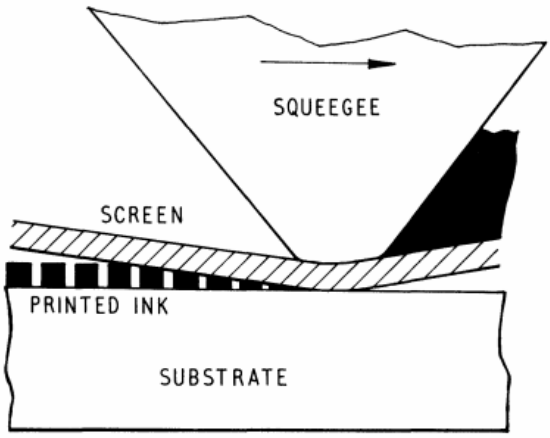

Figure 1-5: Screen printing concept [63]

1.3 Scope of Present Work: Objectives and Governing Hypothesis

Composite conductor materials have shown promise as electrical interconnects for their higher tolerance of applied strain when printed as inks onto polymer substrates [64]. Inclusions have ranged across PZT powders [65], carbon black [66], CNTs [67], and silver flakes [68], among others.

Researchers have successfully demonstrated continuous electrical conductivity of silver flake filled polymer composite inks when subjected to strains upward of 600% [69], though the resistance increases with applied strain. First order approximations and models [27] have been used to predict electrical performance in such hybrid conductors. They assume uniform distribution of filler material, as well as uniform deformation. These models agree with experimental data for low applied strain (<<5%) [26, 70], but not at large strains when non-uniform deformation is expected to occur.

The electrical behavior of compliant conductors under cyclic loading is an important design parameter since ink reliability under repeated loading is expected in medical or structural applications. Common studies that explore conductive composite films' electrical response to fatigue [71-75] correlate in situ resistance measurements to external processing and testing parameters such as thickness of the supporting substrate, resolution of conductive print lines, applied strain amplitudes, and the manner in which strains are applied (e.g. bend vs stretch). Few explore internal deformation mechanisms and electrical measurements under cyclic loading.

Given the simplicity of existing phenomenological models, and the lack of investigation into high-strain conditions, this work seeks to fill in knowledge gaps for the purpose of informing future flexible and stretchable electronic designs. It is hypothesized

that heterogeneities in filler particle size and distribution within the composite ink will lead to localizations in the material as a result of applied strain. In this manner, the conductor is susceptible to failure mechanisms that supersede percolation theory in governing electrical performance evolution.

Hence, this work is divided into three main chapters:

i. Strain Localization

In chapter 3, this thesis articulates the differences in mechanical and electrical responses to monotonic strain between a pair of similar conductive inks supported by a variety of polymer substrates. Leveraging common *in situ* resistance measurement practices during elongation, this work further enriches the data portfolio by coupling optical microscopy and laser profilometry with the experiments. This *in situ*^{2} approach allows for any physical artifacts captured by the imaging to be correlated to the electrical measurements. The collected images facilitate the development of incremental in-plane strain maps of the ink surface, which are then used to identify strain localizations in the ink relative to the applied macro strain. Focused Ion Beam (FIB) cross-sectioning of printed samples before and after experimentation, along with Scanning Electron Microscopy (SEM) is used to draw insights about the architecture of these inks, and what changes manifest beneath the printed surface as a response to applied strain.

ii. Printed Trace Width Effects

Chapter 4 explores the limitations of screen printing conductive traces onto polymer substrates, whereby the printed trace width is varied across tested samples. This geometric parameter is then assessed for general resolution of print, initial electrical capability, and

elongation thresholds for electrical failure. Using data collected from the *in situ*[2] approach, further image processing algorithms are developed to track strain localization artifacts, and draw conclusions about damage evolution and their relevance to printed feature size. FIB/SEM imaging is used to supplement the findings.

iii. High Strain Fatigue Life

This section expands the investigation beyond the single monotonic elongation case into the strain cycling regime, which is more applicable for real world applications. Samples are repeatedly elongated and then partially released in order to capture fatigue life. By varying printed trace width, applied mean strain, strain amplitude, and strain rate, the work identifies the most relevant cycling parameters that influence said life. Comparison of surface profilometry scans after successive sets of cycles helps to articulate the mechanisms that lead to electrical failure in these prints.

CHAPTER 2. EXPERIMENTAL PROCEDURES

This chapter presents the experimental samples and techniques used in the study of electrical performance evolution in screen-printed inks as influenced by applied strain. In addition, it articulates the analytical techniques used to process the data collected from resistance measurements, optical microscopy images, laser profilometry scans and images, and SEM images, to draw conclusions about the relationships between material response to strain and said evolution.

2.1 Sample Characteristics

In this work, 5025 [76] "flexible" and PE 874 [77] "stretchable" inks from DuPont were separately screen printed onto polyethylene terephthalate (PET), Kapton polyimide (PI), and TPU substrates. In the case of 5025, two different formulations of TPU substrates were used: ST604, and TE11C [78]. Both materials are compliant when handled but ST604 is slightly stiffer, indicating a higher modulus. PE 874 was only printed onto TE11C.

Printing was performed at the DuPont Applications Laboratory with tightly controlled proprietary processes that have been optimized over years for the different inks and substrates. Substrate thicknesses were 127 μm for PET and PI. The TPU substrate thicknesses were 89 μm, excluding the temperature stable carrier used as structural support for printing and transportation. A single pass screen print of these inks yields a nominal thickness of approximately 8-10 μm, as reported by the manufacturer. The inks are then cured at 130ºC for 15 minutes. Figure 2-1(a) provides an optical image of 6 specimens printed onto PET with 5025 ink of varying widths from 0.1 to 2 mm. The specimens also

include tick marks spaced 2 mm apart for spatial reference, and test pads for 4-point resistance measurement.

Printed sheets contain 4 sets of each of the 6 trace widths, totaling 24 prints per sheet. Prior to testing, individual test samples are cut from the larger print sheet using the tick marks as guides. For PET and PI samples, cutting was performed using a tabletop paper cutter. The prints on TPU, having too compliant of a substrate for the paper cutter edge, were hand-cut using a circular blade hand tool and straight edge. A single sample measures 10 mm wide by 55 mm long.

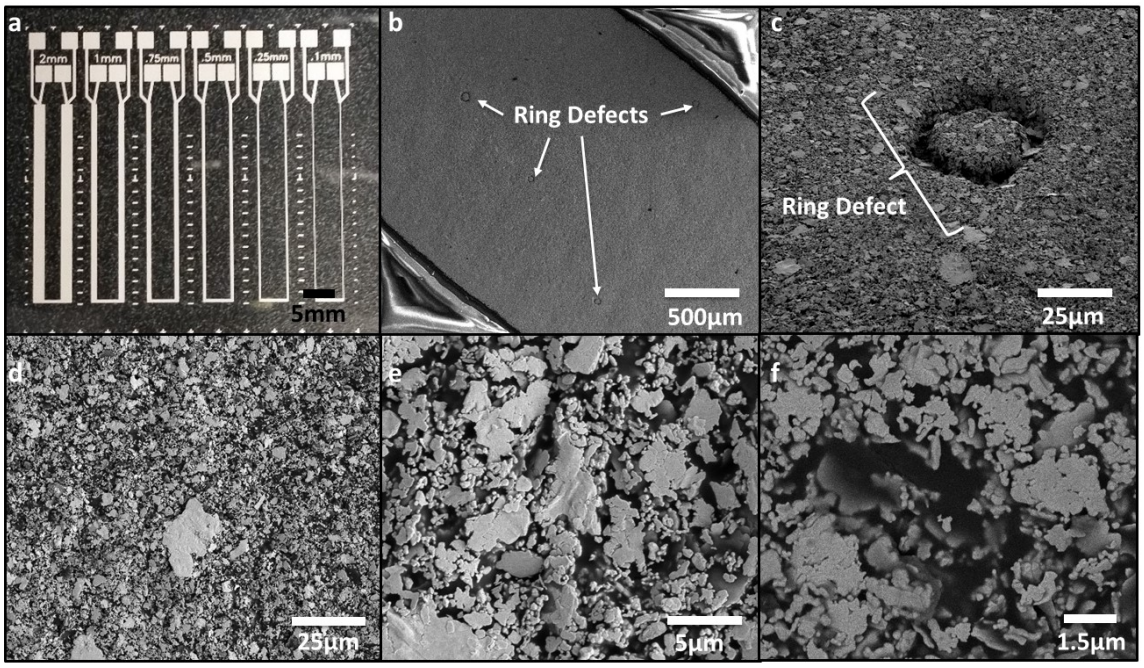

Figure 2-1: (a) Optical image of the 5025 specimens, printed onto PET, showing sample design and trace width variations (b-f) Plane view SEM images of the unstrained ink surface; (b-c) show ring-like defects at two magnifications, while (d-f) show the ink surface at different magnifications. The silver flakes appear randomly dispersed on the surface.

5025 ink is composed of silver flakes embedded in a polymer matrix with an acrylic binder. The reported flake density is 50% by volume. PE 874 contains a slightly higher reported volume fraction of 55% silver flakes, and further differs from 5025 by employing a polyurethane binder. Figure 2-1(b-f) show SEM images of the surfaces of a 5025 print at increasing magnifications. Qualitatively, the surfaces of 5025 and PE 874 demonstrated no distinguishing physical characteristics in the unstrained condition. Ring-like defects on the ink surface (see Figure 2-1(b-c)) were found on both inks. They are attributed to the printing process, and are likely artifacts of emulsion bubbles popping during the printing and curing stages. Flake dimensions qualitatively range from hundreds of nanometers to tens of microns, with no obvious arrangements or concentrations.

The Young's modulus of 5025 is estimated to be 5 GPa, and that of PE 874 is 1.5 GPa. PE 874 is intended to be printed upon TPU substrates, with modulus on the order of MPa, while 5025 is considered more appropriate for PET and PI, whose moduli were measured to be approximately 2.5 and 3.5 GPa, respectively. This is to reduce modulus mismatch between substrate and film. Similarly, Poisson ratios of the hybrid inks are estimated to be 0.33 for 5025, and 0.48 for PE 874. Published sheet resistivity values for 5025 are between 12 and 15mΩ/sq/25μm. PE 874 is <75mΩ/sq/25μm.

2.2 Monotonic Elongation

All *in situ* experimentation was performed using a Linkam TST350 Microtensile Test Stage [79]. The stage provides time-stamped load and displacement measurements, with resolutions of 1 μs, 0.001 N, and 10 μm, respectively. Custom clamps were designed and fabricated using pieces of scrap steel, as well as nylon plastic. The nylon was laser cut

with ports for spring-loaded contacts meant to interface with the four pads of each sample. The steel pieces were water jet cut, and used as bottom clamps, or otherwise wrapped in Kapton tape to prevent accidental electrical connection between the conductive ink and the test stage. The clamps isolate an initial unstretched length of the sample, as indicated by the displacement measurement. This may vary as an initial working length relative to the ultimate applied strain, which itself is limited by the physical range of motion for the stage. The 200N load cell sets the limit for the experimental setup. To avoid sample slippage during testing, PET and PI samples were glued to the bottom clamps using commercial adhesive once they were set to the desired spacing and left to cure before testing. TPU samples were compliant enough for double-sided tape to be effective in this regard. An example of a sample loaded in the stage may be seen in Figure 2-2.

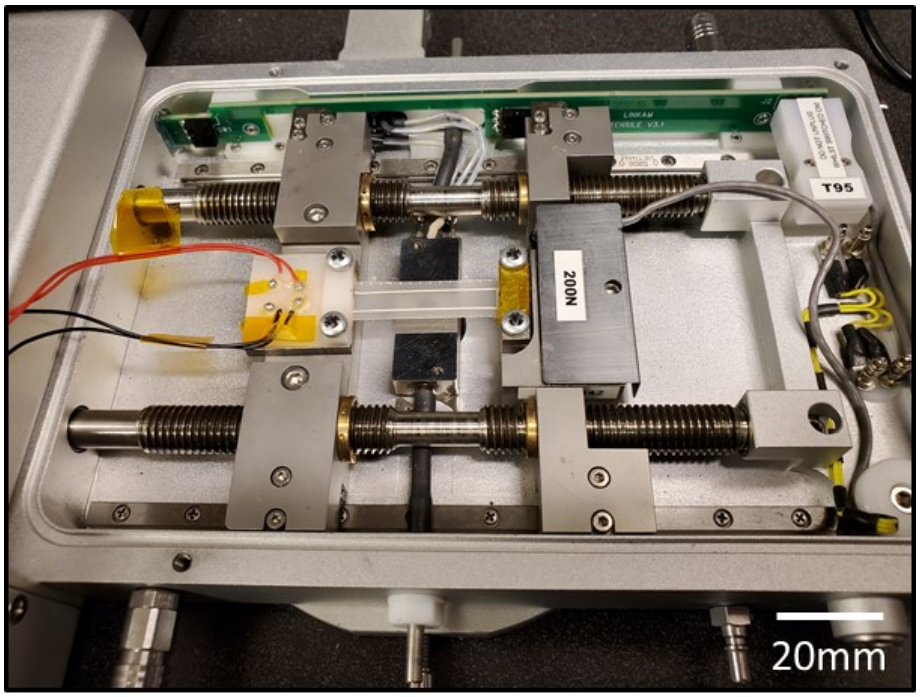

Figure 2-2: 0.5mm wide PE 874 trace printed onto TE11C substrate, cut and placed into TST350 microtensile test stage

Four lead wires extend from the spring-loaded contacts in the nylon top clamp to connections with an Agilent 34401a digital multimeter for *in situ* resistance measurement during elongation of the stage. Resistance measurements are output from the multimeter to the nearest milliohm.

All test parameters, protocol execution, and subsequent data collection was handled through Labview, which allowed for proper time syncing of load and displacement measurements from the tensile test stage with resistance measurements from the multimeter. The sampling rate for data collection was approximately 2Hz. Tests varied from stepped cases – elongating to specific strain values at specified strain rates – to continuous cases, whereby the clamps continued to separate at a specified speed until manually halted at the occurrence of a particular event. An example of this might be an open circuit measurement in the distressed ink, at which point further elongation would no longer yield coupled electrical and mechanical data.

Initial and *in situ* displacement and resistance measurements collected from each experiment were then used to generate normalized resistance (R/R_0) versus applied strain plots. Of critical importance was properly allocating the normalized resistance values to the conductive material being elongated, and not that of the entire sample. As such the sample initial resistance measurement was first distributed along the entire sample print length, and then a fraction of that value proportional to the section between the clamps was taken as the experimental initial resistance. In this manner, all increases in resistance could be tallied and normalized against the experimental initial value. For example, a test sample has a printed circuit length of 76 mm. Given that the pattern is un a "U" shape, the relevant dimension for a sample placed in the Linkam stage would be twice the clamp width, W_{clamp}.

Therefore the initial experimental resistance, R_0, can be taken as a proportion of the total measured resistance in the unstrained condition:

$$R_0 = R_{total,\varepsilon=0} \times \frac{(2 \times W_{clamp})}{76} \quad \text{Equation 2.1}$$

Any change in resistance during the experiment, ΔR, can be attributed to elongation of the sample section between the clamps. As such:

$$R = R_0 + \Delta R \quad \text{Equation 2.2}$$

$$\frac{R}{R_0} = \frac{R_0 + \Delta R}{R_0} = 1 + \frac{\Delta R}{R_0} \quad \text{Equation 2.3}$$

The clamp spacing can reach a minimum value of 16 mm, and the Linkam stage has approximately 58 mm of travel. This allows for the theoretical application of up to approximately 360% strain to a given sample.

2.3 Strain Cycling

The testing protocol for strain cycling was as follows: the resistance changes were monitored in samples that were elongated by applying a maximum applied strain, ε_{max}, and then strain cycled between the ε_{max} and a minimum applied strain, ε_{min}, that was always greater than 0% strain (e.g. Tension-Tension cycling). Controlled parameters for any given test include strain rate (commonly 2% per second), strain amplitude: $(\varepsilon_{max} - \varepsilon_{min})/2$, and mean strain: $(\varepsilon_{max} + \varepsilon_{min})/2$. Data collected was used to calculate normalized resistance (R/R_0) for a given applied strain amplitude and mean strain during the test. Timestamps on

collected data were used to correlate measurements and calculations to specific cycle increments. Individual tests were halted once resistance measurements reached a consistent state of erratic values, or open circuit signals, such that further sampling no longer yielded coupled electrical and mechanical data.

2.4 Optical Microscopy and Laser Profilometry

In order to observe the deformation of the conductive composite thin film, a select number of samples were tested with the Linkam stage while under an Olympus LEXT OLS4000 confocal microscope. This tool captures optical microscopy images, as well as information about the surface topography using the laser profilometer. The optical image is created by digitally stitching the field of view captures across a range of heights, thereby mitigating any compromise in image resolution from features outside the static depth of field of the optical objective. The laser scans give the topography of the view area and output the height measurements across the scanned area. Depending on the magnification used, window size and resolution vary. For example, a 50x magnification objective provides a 256 μm x 256 μm window, with a profile height resolution of 0.24 nm. A 20x magnification objection yields a 640 μm x 640 μm window, with a profile resolution of 0.8 nm. All scans are sized to a 1024 pixel x 1024 pixel image, so scaling adjusts accordingly. The in-plane resolution of the 50x objective is 0.25 μm per pixel, while the 20x objective carries a resolution of 0.625 μm per pixel. This *in situ*[2] setup may be seen in Figure 2-3(a).

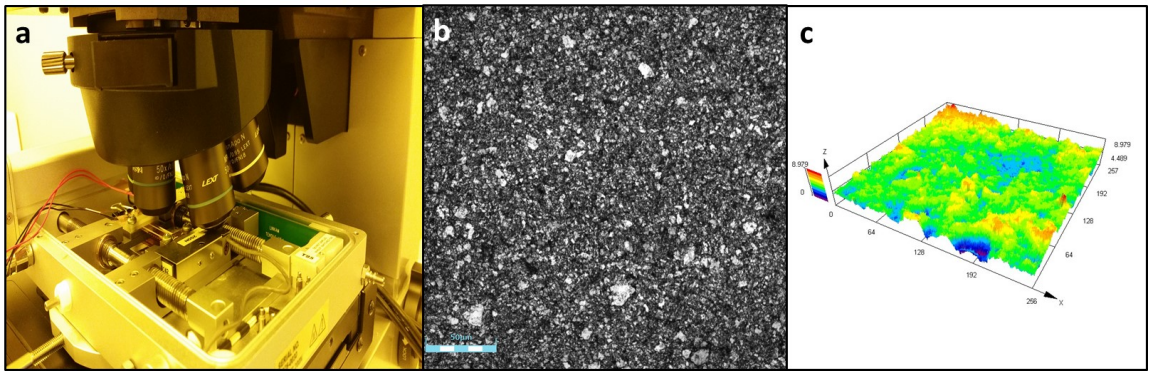

Figure 2-3: (a) *In situ*[2] setup depicting 5025 ink printed onto a PET substrate and loaded into the Linkam microtensile test stage, which is placed underneath the LEXT confocal microscope (b) Optical image of 5025 ink printed onto a PET substrate in the unstrained condition, taken at 50x magnification (c) Profilometry scan output of 5025 ink printed onto PET substrate in the unstrained condition, taken at 50x magnification

In the case of strain cycling, the conditions for the samples tested under the confocal microscope reflected the largest applied strain that could be applied while the normalized resistance under monotonic stretching remained less than 500. We note that there is no clear definition for fatigue life of thin films in the literature. Several criteria have been used, mainly related to an arbitrary increase in normalized resistance (from 2% to 25%) [41, 80]. In this work, we define R/R_0=500 to be a parameter of interest based on our experimental results. Coincidentally, at a normalized resistance of 500, unstable crack propagation has been observed during stretching of brittle thin oxide films deposited on a polymer substrate [81]. For samples tested at a maximum applied strain of 80%, the Linkam stage was rotated so as to avoid collision with other objective lenses attached to the confocal microscope. The angle of rotation was measured before cycling. The test was paused for a few moments at maximum strain of 80% every 10 cycles to allow time to complete the scans, and finally ended after the completion of 100 total cycles.

2.5 In-Plane Strain and Displacement Maps

High magnification optical images were taken in-situ at regular increments of strain. These image sets were then processed using an open source Digital Image Correlation (DIC) software, Ncorr, created at Georgia Tech [82]. This provides a scale agnostic method that monitors changes in features during loading using image registration. Plane view images of the ink samples in the unstrained condition were used as reference images. The flakes and matrix were a natural contrast that was used to track the local displacement field. Ncorr, like other subset-based DIC algorithms, divides a patterned image into smaller areas (subsets) and monitors their movement in subsequent images that are obtained during deformation, e.g. uniaxial stretching of the inks.

The analysis provides in-plane displacements u and v with sub-pixel resolution for each subset center, since deformation in each subset is assumed to be a linear, first order transformation. Both the subset radius, r_s, as well as the subset overlap can be varied. Ncorr obtains in-plane strains from the gradients of a least-square plane fit over a group of subset center points of size w_e from the displacement field.

The DIC parameters, r_s and w_e, were determined from a Rigid Body Translation (RBT) analysis of two reference images of each ink. The reference images were taken prior to each strain test, whereby the translated image was obtained by shifting the sample stage beneath the scope lens by a few millimeters in a single direction. Any deviation from zero (no strain) in the resulting Ncorr analysis will give the uncertainty in the measured displacement or strain under uniform stretch of a given pattern. This error was calculated for different values of the subset radius and strain window with the minimum substep

overlap of 1 pixel, providing a low bound estimate of the error in the strain field assuming that the deformation is uniform. This is illustrated in Figure 2-4.

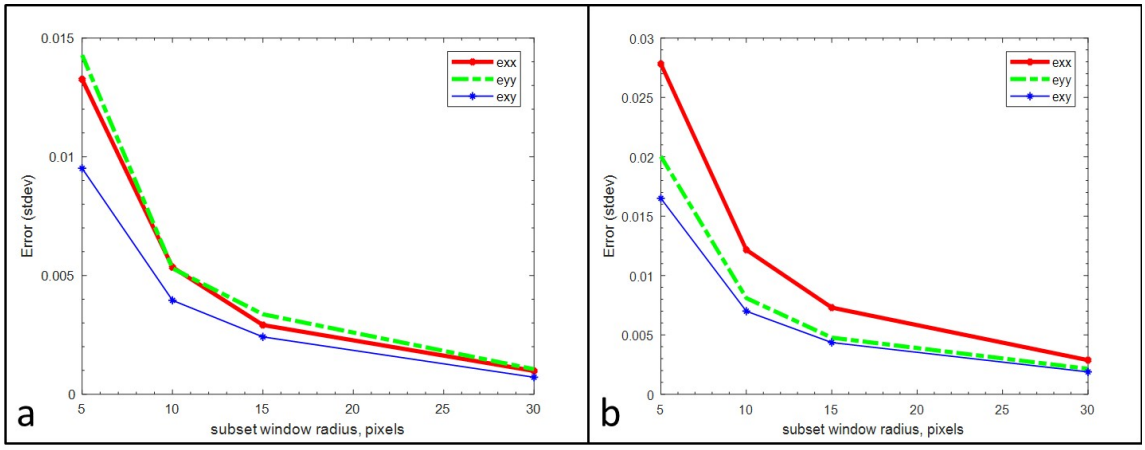

Figure 2-4: Relative error calculations based on subset radius size for (a) 5025 printed ink and (b) PE 874 printed ink

Based on the above evaluation, subset radii of 10 pixels and strain radii of 5 pixels were selected for all subsequent analysis. Given the optical image resolution of 4 pixels per micron, this translates to subset and strain window sizes of 5 sq. μm and 2.5 sq. μm, respectively. The above subset window radius and strain window gave an error of 0.5% for the 5025 and 1.2% for PE 874 in the direction of sample elongation, assuming uniform deformation. Errors may be slightly higher in regions of strain localization.

In the case of strain cycling, the relative positioning of the sample underneath the LEXT microscope objective does not remain constant across every cycle set. As such, the profile scans cannot be compared directly with each other after each cycle. The height profiles need to be translated and possible interpolation is needed before comparing the thin film surface after each cycle. For this purpose, DIC is used. Specifically, we compare topographical images of the surface obtained using the LEXT microscope at different

cycles and compare them with the topographical image at the first cycle. The height profile contours have unique features as can be seen from Figure 2-5(a) contour and Figure 2-5(b) surface height profile of the surface. The topographical images are separated into smaller subsets whose radius, r_s, is 10 pixels, which equals to 5 μm.

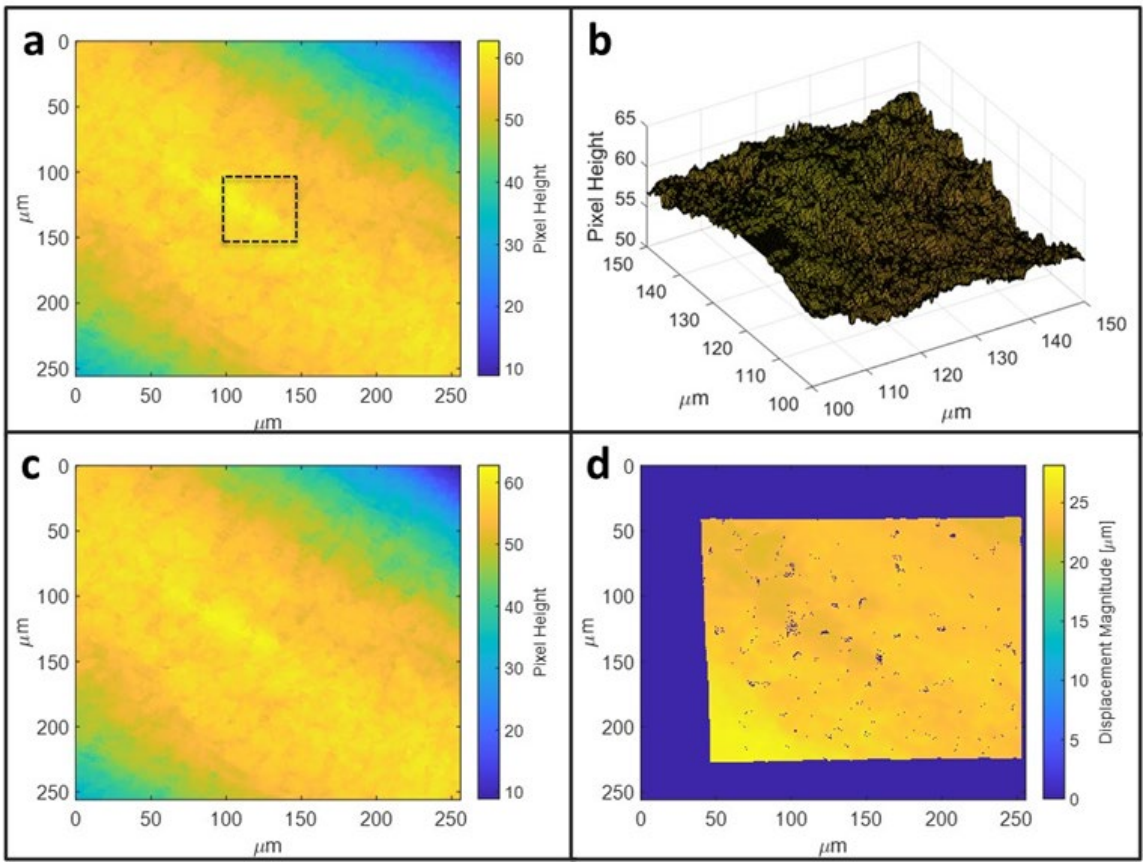

Figure 2-5: Topographical maps of a region of 0.5 mm PE 874 printed onto a TE11C substrate (a) strained to 80%. The region within the dotted outline is selected for (b) 3D rendering (c) 2D profilometry field of the same sample after cycling between 50% and 80% strain 100 times (d) Translation map correlating the shift of the pre and post cycled samples scans seen in inserts (a) and (c). Note that the translation is nearly uniform with a magnitude of approximately 25 μm.

Assuming deformation in each subset to be a linear, first order transformation, in-plane displacements u and v are analytically determined for each subregion center with

sub-pixel resolution. The output gives in-plane translation of each topographical map after each cycle. Such a field can be generated to compare any cycle set increment. Figure 2-5(c) shows the surface after 100 cycles with Figure 2-5(d) showing the relative displacements (of the order of 25 μm) from the first cycle.

2.6 Surface Image Processing for Damage Analysis

Surface crack formation was identified in one of the printed inks as a response to applied strain. These features are observable in images from optical, SEM, or profilometric scans, with cracks appearing far darker than either matrix or flake material. Using Matlab, these images were imported and binarized to emphasize the crack patterns. After tracing over these cracks, the images can be imported back into Matlab where color filtering and object recognition algorithms can track crack formation and growth. The crack patterns can also be assessed for their qualitative impact on conductive paths within the ink. An example of this process may be seen in Figure 2-6.

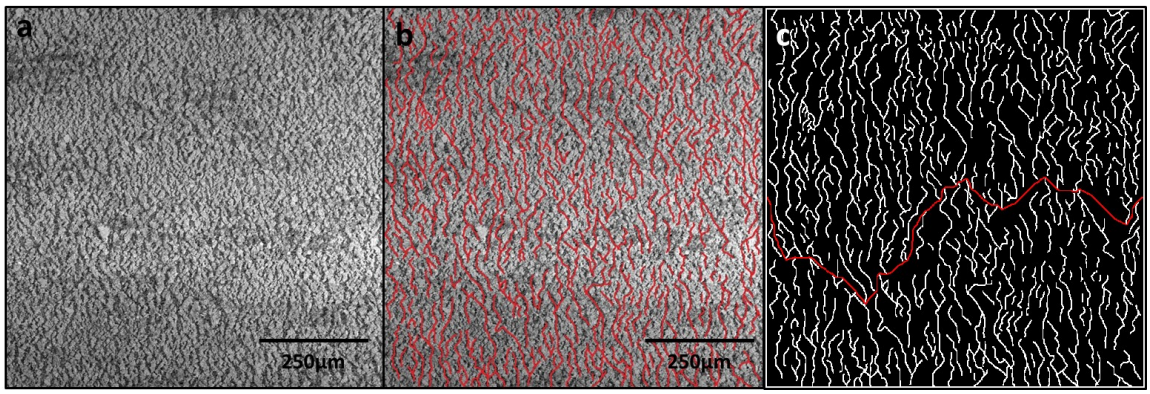

Figure 2-6: (a) SEM surface image of PE 874 printed on TE11C, strained to 200% (b) Tracing of surface cracks (red) on SEM image (c) Shortest path (red) calculated from center-right of image to center-left of image, avoiding surface cracks. Path represents a more than 30% increase in conduction distance for selected view area

2.7 Fractography (SEM, FIB Cuts, Cross Section Analysis)

In order to quantify and understand the architecture (especially the flake volume fraction) of these inks, and their subsequent response to applied strain, cross-sections of specimens before and after mechanical testing were obtained using a focused ion beam FEI Nanolab 200. Gallium ions were used to mill rectangular regions of the ink so as to expose the through thickness ink morphology e.g. height, flake fraction, etc. Platinum deposits of 1-2 μm were placed in cut areas ahead of time to preserve surface integrity. Post experiment cross sectioning also took place for comparative analysis. FIB cuts were initially made at 30 kV and 3 nA, followed by a polishing section cut at 0.3 nA to remove any atomized material that may have deposited onto the section surface during milling at higher current. After sectioning, samples were rotated 52° for SEM imaging. Thickness measurements were corrected for this angle. Imaging took place at 2kV and 0.86nA in order to resolve the non-conductive matrix alongside conductive silver flakes within the cross-sections. This allowed for identification of any true void space within ink architecture.

Once captured, through thickness SEM images were used to identify characteristics of each ink before and after straining. This included ink thickness and area fraction of conductive filler. Using ImageJ [83], a Java-based image processing tool, screen shot images were converted to 8-bit data files. The images were binarized and statistics of the flake area fraction and local ink height were obtained along the width of the sections.

2.8 In-House Screen Printing

In an effort to investigate potential influences of print process on final dry ink architecture, a small number of samples were screen printed on site at Georgia Tech.

Specimens consisted of PE 874 ink printed onto a 0.003” (76.2 µm) thick polyurethane film, as shown in Figure 2-7.

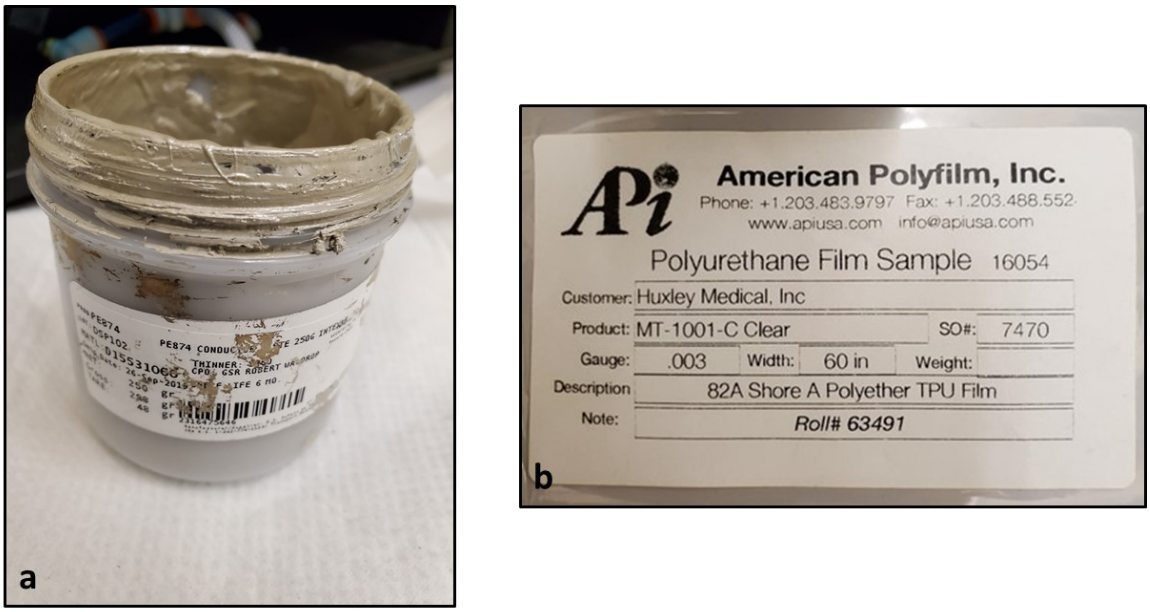

Figure 2-7: (a) 250g container of PE 874 (b) Polyurethane film supplier label

The screen used for this ink, having a stainless steel mesh of thread diameter 0.0009” (22.86 µm) and spaced at 325 threads per inch with a mesh to frame angle of 45°, was provided by Hary Manufacturing Inc. The theoretical wet print thickness reported by Hary for this mesh configuration is 0.001” (25 µm). The same artwork used by DuPont for producing traditional test specimens was applied to this screen, using an emulsion material of thickness 0.0005” (12.7 µm).

The printing procedure occurred as follows: 1) A hand cut sheet of polyurethane substrate was placed over a vacuum stage, and taped in place under vacuum to remove any wrinkles. 2) The screen was lowered over the substrate, and leveled to a position several microns above the substrate. (3) The screen was then hand-flooded with wet PE 874 ink,

to confirm all mesh apertures were filled and, also, to limit waste ink with each print. (4) A semi-rigid squeegee blade was pressed and dragged across the print in a single pass, with sufficient pressure to force contact between the screen and substrate. (5) The screen was lifted up away from the substrate, and the substrate with newly printed design was taken for cure. These steps are illustrated in Figure 2-8 below:

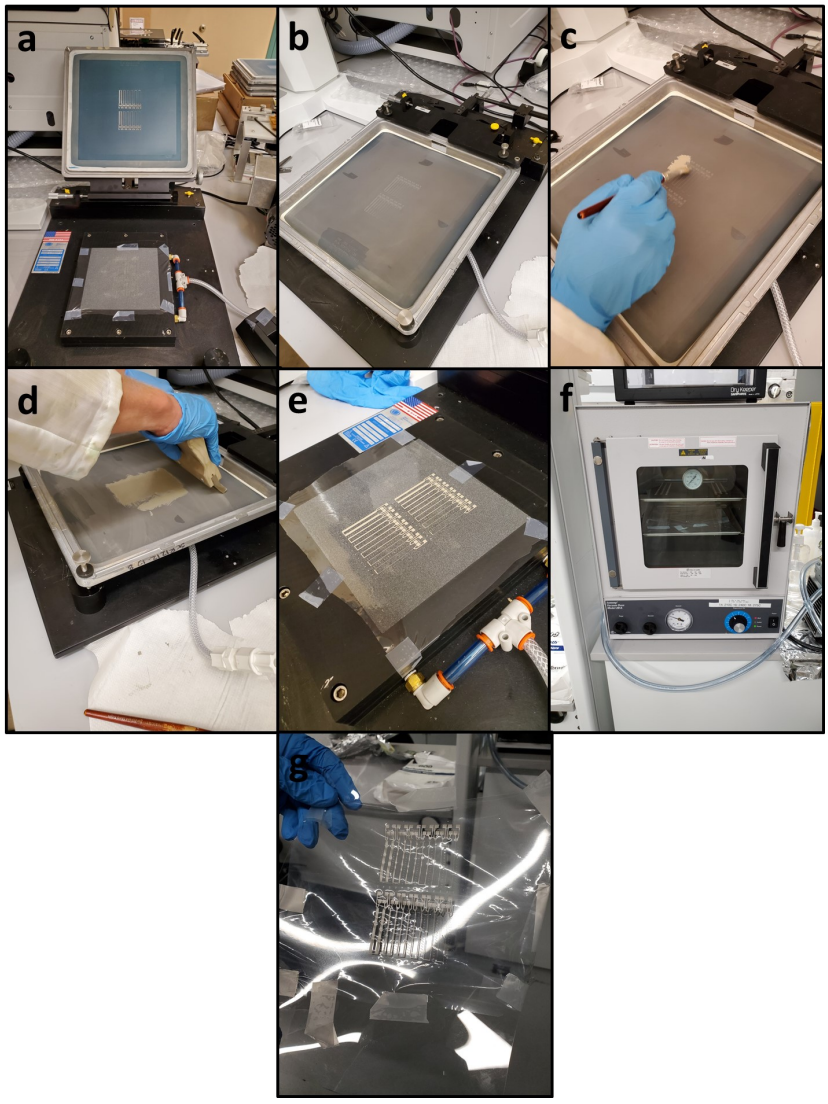

Figure 2-8: In house screen printing process (a) Substrate placement on vacuum stage (b) Screen placement and leveling (c) Flooding screen apertures with wet PE 874 (d) Hand printing (e) Completed wet print (f) Chamber for temperature/vacuum cure (g) Completed wet print

Some prints went through additional processing, consisting of modified procedures in the cure phase. A subset of in house prints were either cured in a vacuum environment at standard temperature and duration, held in a vacuum for at least an hour prior to vacuum cure, or sonicated for a total of 10 minutes, in 20 second intervals, prior to vacuum cure. The sonicator setup and vacuum gauge reading are shown in Figure 2-9:

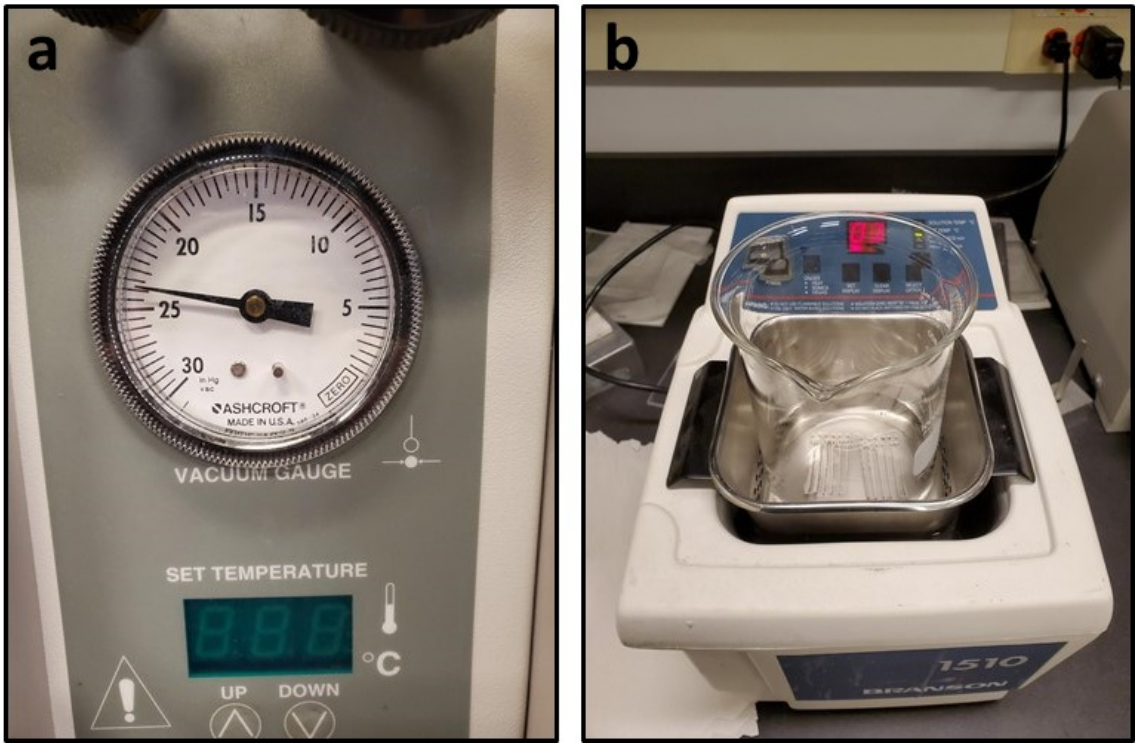

Figure 2-9: (a) Vacuum gauge reading of ~24in. Hg, standard for all cure operations of in house prints (b) Sonication setup for in house prints

CHAPTER 3. THE ROLE OF STRAIN LOCALIZATION ON THE ELECTRICAL BEHAVIOR OF FLEXIBLE AND STRECHABLE SCREEN PRINTED INKS ON POLYMER SUBSTRATES

Originally Published in Acta Materialia, Volume 10, May 2020

In this chapter, both flexible (5025) and stretchable (PE 874) inks were subjected to monotonic elongation in the *in situ* and *in situ*^{2} setups described by 2.2 and 2.4. This encompassed every combination of ink and substrate available. Strain maps derived from surface images captured localization trends. Fractographic analysis pre and post mortem offers insights into the architecture of the inks, and the physical changes that manifest due to applied strain.

3.1 Initial characterization

Figure 3-1 compares the respective cross sections of undeformed 5025 and PE 874. In both inks we can see high dispersal of silver flakes, comparable to that of their surfaces. Flakes are observed to vary significantly in dimension, from several μm to hundreds of nm long. Qualitatively, a large proportion of long flakes, those measuring several μm, are oriented horizontally in line with the print direction. This is potentially due to shearing forces imposed during the screen printing process, and orientation that can occur during the drying process. It is also important to note that this cross-sectioning reveals inherent defects (voids) within the PE 874 that are not found in 5025. A possible reason for the presence of voids is the high filler loading of the PE 874, at 55 v. When the filler loading is greater than the maximum packing fraction for random, loose packing (akin to the tap

density), estimated to be 53 v%, voids are created within a coating due to the porosity of polymer. The filler particles do not pack down densely during drying, and air is subsequently incorporated into the coating.

The average initial thickness for 5025 is 9.1 μm, with standard deviation of 0.75 μm, while it is 11.8 μm for PE 874, with standard deviation of 1.1μm. Given these thicknesses, a sample ink trace width of 2 mm, trace length 72 mm, the resistance is predicted using Equation 1.1.

Given the sheet resistivity values reported in 2.1, the predicted resistance values are between 1.2 and 1.5 Ω for the 5025 samples, and less than 5.7 Ω for the PE 874 samples. Average measured resistances are 2.2 Ω with standard deviation of 0.17 Ω for 5025 and 2.8 Ω with standard deviation of 0.47 Ω for PE 874. The higher measured resistance in 5025 suggests that thickness measurement taken from the cross-section cut does not reflect the average value within the ink given the variability in thickness (several microns) observed from surface roughness measurements.

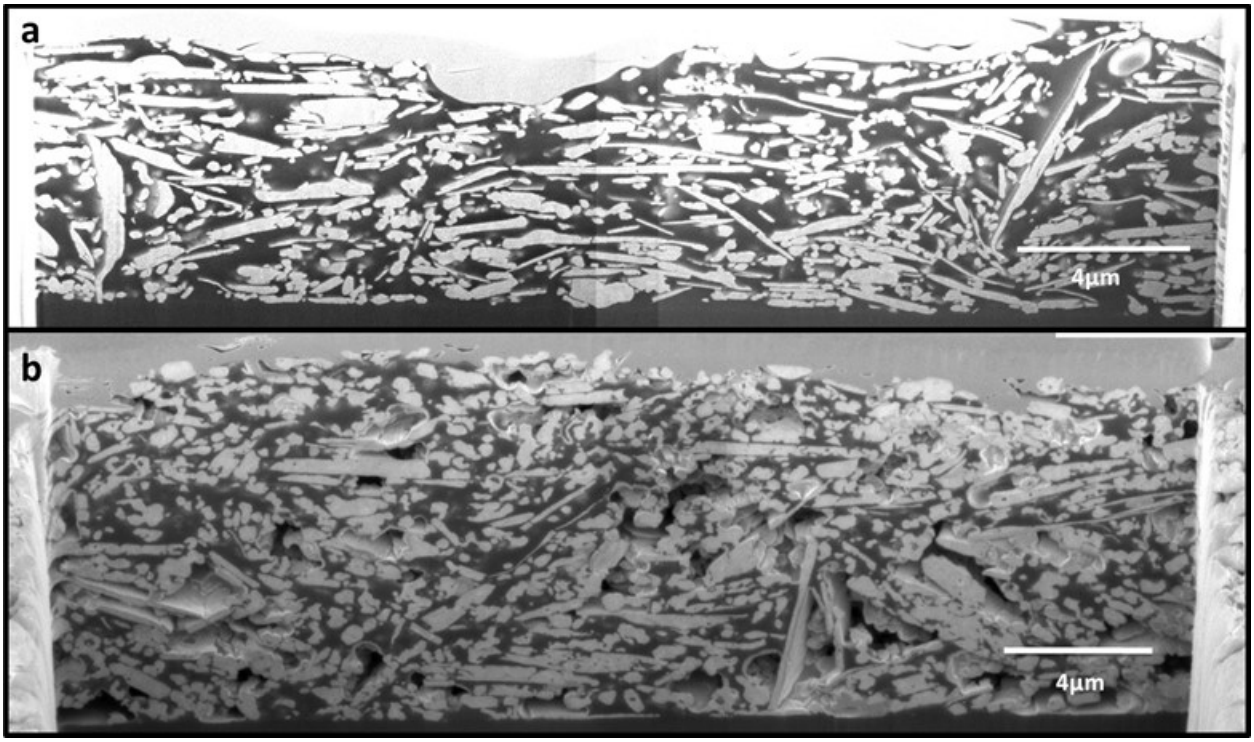

Figure 3-1: SEM cross sections of hybrid inks, taken at 52° tilt: (a) 5025 flexible ink, unstrained (b) PE 874 stretchable ink with voids, unstrained. The silver flakes appear light gray in color while the binder is darker gray. Voids are apparent in PE 874 as darker (nearly black) areas.

The initial FIB cross sections were used to calculate flake area fraction distributions. Applying a normal distribution to flake fraction values over the entire cross section, 5025 presents a mean filler fraction of 49%, with standard deviation of 9%. Mean flake fraction in PE 874 is higher, at 54.5% with standard deviation of 10%. The average void area fraction is 17% for PE 874; these voids vary in size, orientation, and aspect ratio. The smallest measure roughly 0.5 µm in diameter. Larger voids are as long as 6 µm, but are extremely narrow, measuring only about 0.3 µm across.

3.2 Normalized Resistance vs. Strain

The resistance in both flexible and stretchable inks increases with applied strain. As the initial unstrained resistance value is different between samples, the resistance values measured under strain are normalized with the undeformed resistance value. Figure 3-2(a) shows the normalized resistance with applied strain for both inks onto the three different substrates. The normalized resistance of the flexible ink has a similar evolution when printed on PET and PI, but for the TPU substrates (TE11C and ST604) the normalized resistance increased at much higher rates. This is expected, given that 5025 is not meant to be used with TPU, due to large elastic modulus mismatch inducing cracking. The stretchable ink (PE 874) did not exhibit a sensitivity to the substrate upon which it was printed, as all of its performance plots closely overlapped. These data highlight the importance of substrate on the electrical behavior under strain, especially for stiff inks on soft substrates. The rest of this chapter focuses on data obtained on PET substrates, in order to compare the ink behavior.

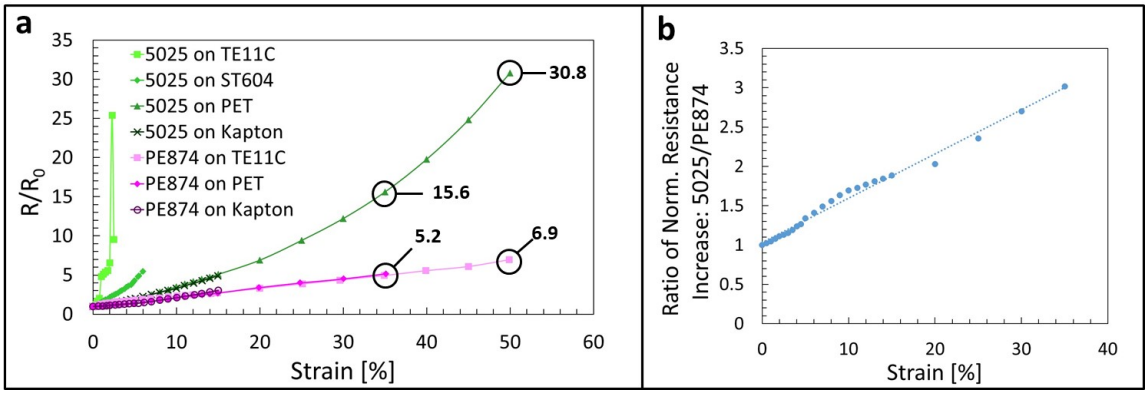

Figure 3-2: (a) Normalized resistance with applied strain for the two Ag inks screen printed on different substrates (b) Ratio of relative resistance increase with strain between 5025 and PE 874 printed onto PET.

Both inks on PET have a linear increase with resistance up to 20% strain, after which the resistance for 5025 rapidly increases. PE 874 performed much better with respect to applied strain than its 5025 counterpart. Figure 3-2(b) plots the ratio of normalized resistance values between 5025 and PE 874 when strained on PET. The disparity in electrical performance appears to increase linearly, such that by 35% applied strain the normalized resistance increase is 3 times more for 5025 than for PE 874.

3.3 Strain Localization

Figures 3-3(a) and 3-3(c) show optical images of the surface of the two inks on PET from 0 to 15% strain (additional ink-substrate strain evolution plots may be seen in Appendix A). When supported by this substrate, PE 874 develops surface cracks that are visible starting ~5-7% applied strain, while 5025 exhibits no discernible changes in the optical images with applied strain. The cracks for PE 874 are broadly distributed throughout the image, which suggests a universal response in this ink.

Figures 3-3(b) and 3-3(d) show the in-plane strain along the stretch direction (E_{xx}) up to 15% applied strain. Color bar scaling is set from 0-100% strain. In both cases, we see that strain localizes in narrow bands that are initially oriented perpendicular to the direction of applied strain. For 5025, the localization begins at low applied strain levels. At 7% applied strain, the strain within the localization bands is 4 times greater than the applied strain for 5025 and 3 times greater than the applied strain for PE 874. The strain in between the bands is much lower and some regions within the bands can remain undeformed (have zero strain). Please note that very low levels of strain are within the resolution limit of the current optical imaging setup and the pattern used e.g. the natural contrast between flakes

and binder. We also note that the strain within the localization bands can be even greater than a factor of 3 or 4 from the applied strain since the in-plane "local" strain is averaged over the subset window size and strain window size. The spacing of the localization bands is periodic and two-dimensional Fourier transformation of the strain field was used to identify the band spacing to be 28 μm for 5025, and 32 μm for PE 874. Moreover, as the applied strain increases beyond 10%, the individual localization bands begin to also combine along the lateral direction.

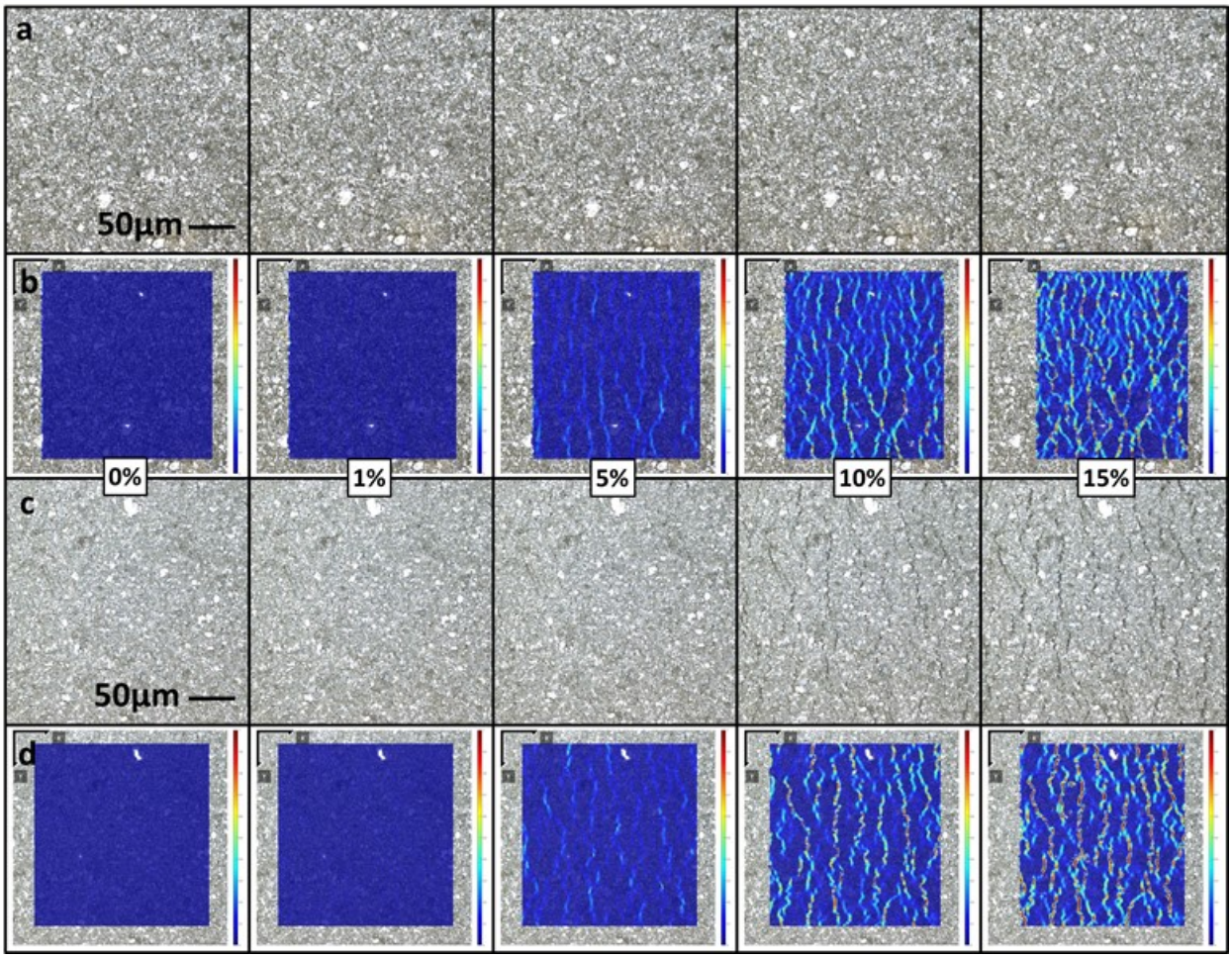

Figure 3-3: Optical imaging and strain field calculations for 5025 and PE 874 under applied uniaxial far field strain values of 0%, 1%, 5%, 10%, and 15%. (a) 5025 "flexible"

ink optical surface images (b) 5025 strain field overlay (c) PE 874 “stretchable” ink optical surface images (d) PE 874 strain field overlay

As the bands interconnect, above 15% applied strain, the integrity of distinct localization bands breaks down, especially for 5025 so that more areas of the ink are involved in accommodating the macroscopic applied strain resulting in a more even distribution of the field. Strain is therefore accommodated in more regions, contributing to largely uniform reduction in thickness for 5025. Since PE 874 exhibited surface cracking, Poisson effects are superseded and significant thickness reduction is not expected, as shown next.

3.4 Fractography

Given that far-field applied strain is largely accommodated through localized band formation for both inks, SEM images of post-test plan and through thickness cross-sections (after tests to 35% applied strain) were taken to further understand the differences in damage behavior between the two inks. Figures 3-4(a) and 3-4(c) show the plane-view surfaces for each ink after 35% strain. There are marked differences from the initial SEM top view images of Figure 3-1. In 5025, significant debonding between silver flakes and the matrix (that can be better seen on Fig. 7(a)) have occurred. Moreover, some regions have undergone extreme reductions in ink thickness (see Figure 3-4(b)) that appear to also have a lower flake density compared to surrounding ink space. For PE 874 cracks are present throughout the area, with spacing of approximately 30 μm that coincides with the initial localization spacing identified from the strain maps (see Figure 3-3).

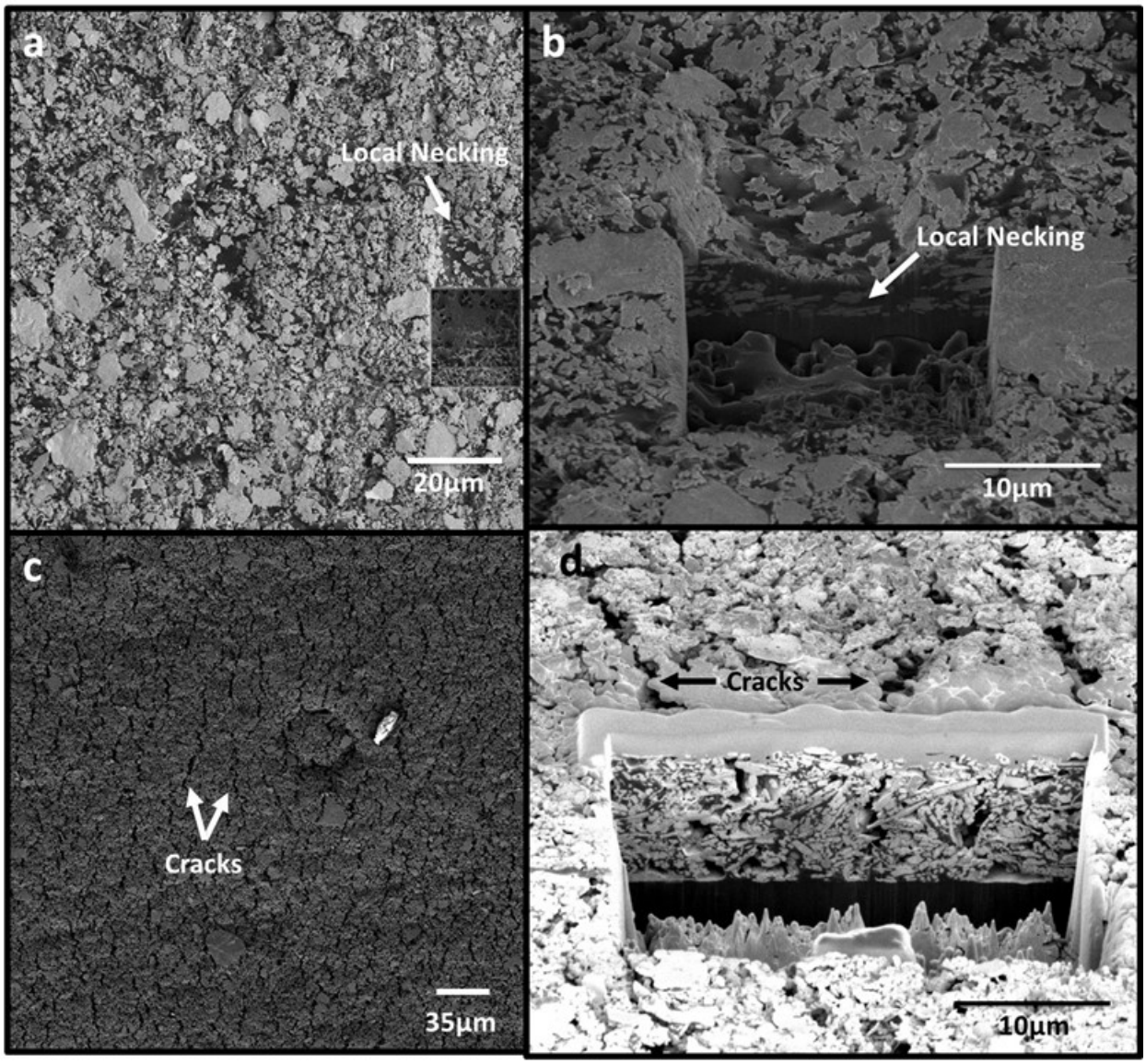

Figure 3-4: Low-magnification top-down or inclined SEM images of hybrid inks, post 35% strain: (a-b) High strain localization in 5025 flexible ink (c) Manifestations of surface cracking in PE 874 stretchable ink (d) Alignment of internal voids with surface cracks in PE 874

Figure 3-5 shows two cross-sections of 5025 and PE 874. For 5025 the same flake-matrix debonding observed at the surface is seen within its thickness. The overall ink thickness decreased to approximately 4-6 µm, however within the local necking areas, thickness decreased to as low as 2 µm. In contrast, in PE 874 the thickness only decreased

to approximately 10 μm, with no local necking. Of particular note is the apparent coalescence and growth of voids within this ink. Orientation and spacing of expanded voids coincide with that of the surface cracks observed. To summarize, the fractography results highlight that significant plastic deformation occurs with 5025, resulting in large thickness reduction resulting in local necking. These large plastic deformations are consistent with the widespread debonding observed between flakes and matrix. In contrast, the widespread cracks observed with PE 874 have little plastic deformation in their vicinity, as evidenced by the small thickness reduction in these areas. Instead, damage/deformation is localized within these cracks. For the two inks, there is therefore a difference in flake distributions and thicknesses that should impact electrical resistance increases differently.

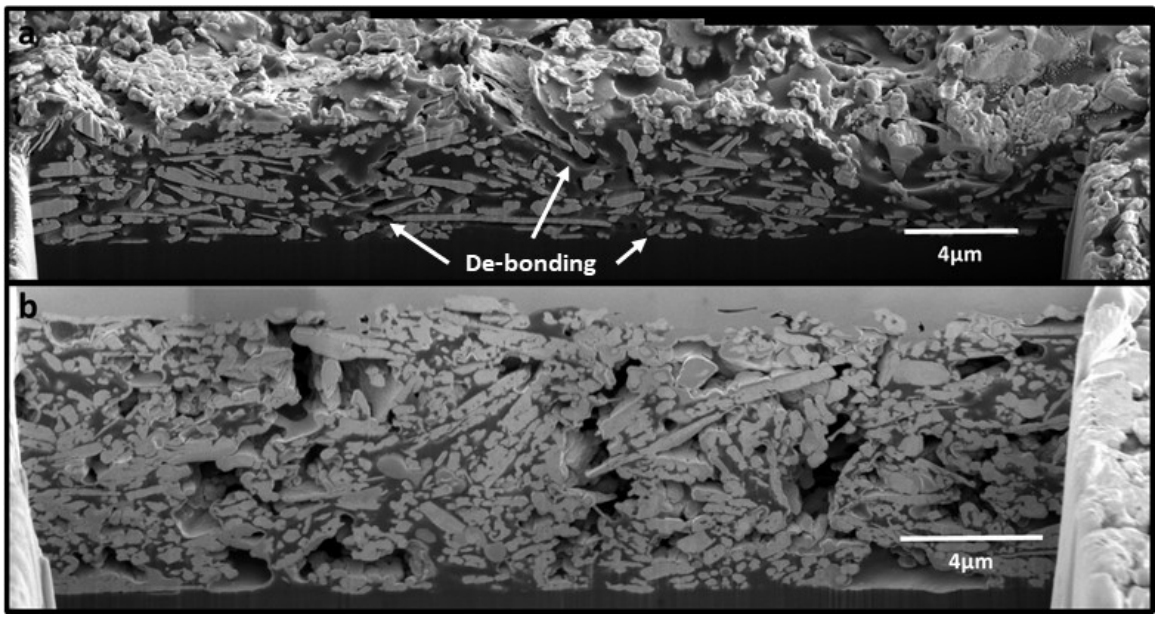

Figure 3-5: SEM cross-sectioned areas of hybrid inks, post 35% strain: (a) Flake-matrix debonding and extreme thickness reduction in 5025 flexible ink (b) Expanded and oriented internal voids in PE 874 stretchable ink

Figures 3-6 and 3-7 compare the height and flake area fraction distribution plots obtained from the binarized cross-sections shown in Figure 3-1 and Figure 3-5, for 5025

and PE 874, respectively. The silver flake area fraction along the cross-section length was calculated and normal distribution curves were fit to the data. For 5025, the flake area fraction average changes from 49% to 35% after straining. Within the local necking regions of the ink, this fraction averages about 25%. This is significant, in that both the thickness and flake fraction are known to negatively impact the resistance in these local areas. PE 874, exhibits minimal changes to thickness and maintains its mean flake fraction value of 54.5%, with a slightly higher standard deviation of 11%. But void area fraction increases to 24.7%, a 45% increase compared to the initial 17% void fraction. It is important to note that these voids do not appear to cover the full through-thickness of the ink, however their vertical height is extensive. As such, while there are no significant reductions in overall ink thickness with PE 874, the effective local thickness is reduced after the appearance of the surface cracks. Within the cross section captured, an area below a grouping of voids measures 1.4 μm in height, comparable to that of 5025. However, mean flake fraction in this area is significantly higher, at 42%.

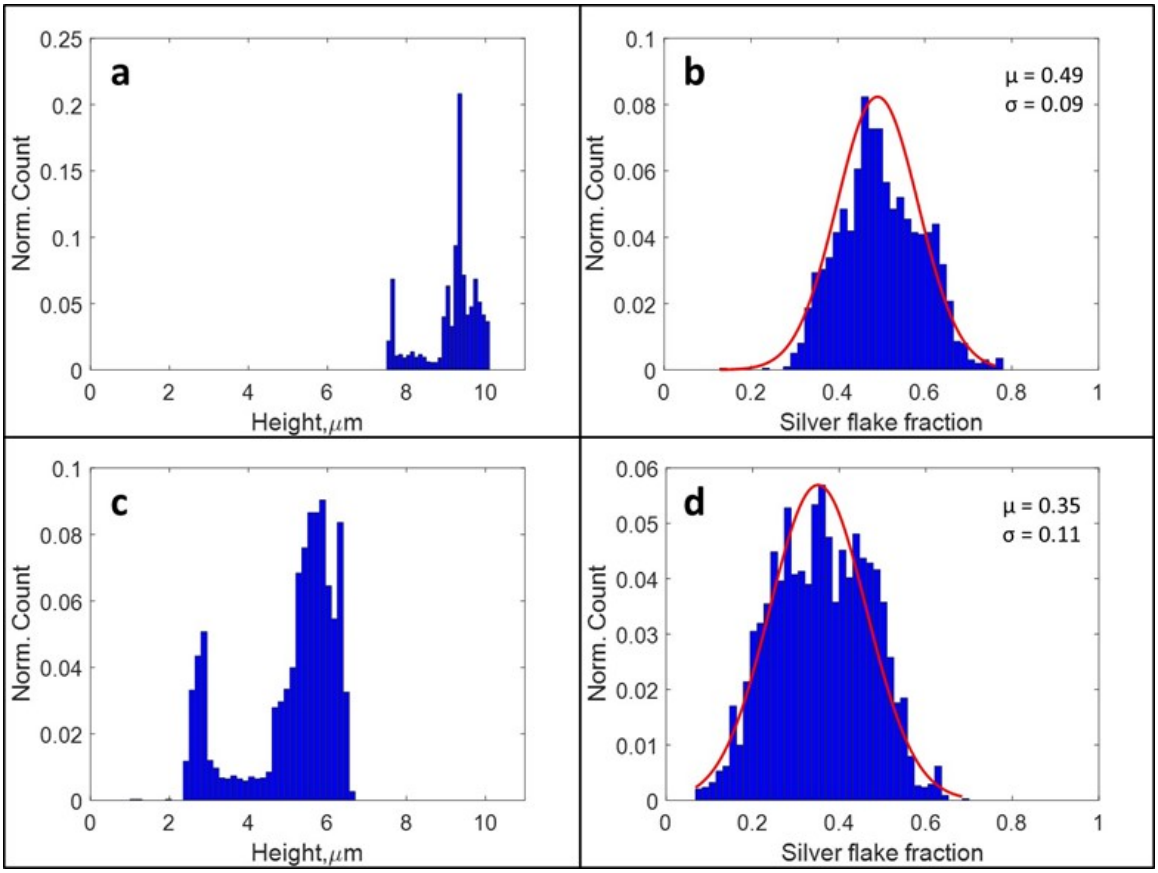

Figure 3-6: 5025 flexible ink height and flake fraction: (a) Height distribution, unstrained (b) Flake fraction, unstrained (c) Height distribution, post 35% strain (d) Flake fraction, post 35% strain

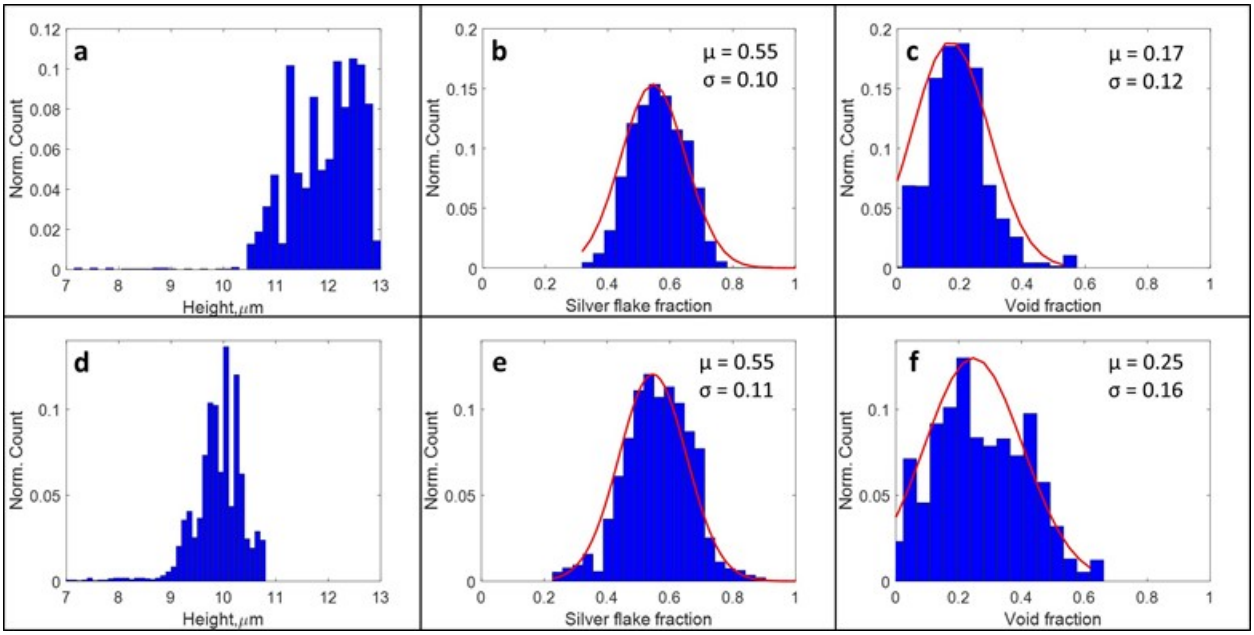

Figure 3-7: PE 874 stretchable ink height, flake, and void fraction: (a) Height distribution, unstrained (b), post 35% strain (e) Flake fraction, post 35% strain (f) Void fraction, post 35% strain

3.5 Discussion

For characterizing, the electrical conductivity of a percolating network of silver flakes within these inks, we look back to Equation 1.10. Rewritten slightly differently to yield a normalized conductivity term, we get:

$$\frac{\sigma}{\sigma_c} = 1 + \left(\frac{\sigma_m}{\sigma_c} - 1\right)\left[\frac{\varphi - \varphi_c}{\varphi_{max} - \varphi_c}\right]^s \qquad \text{Equation 3.1}$$

where, *s* has now taken the place of the original fitting exponent, and φ_{max} that of the max packing volume of Ag flakes. The change in the flake volume fraction of a sample subject to uniaxial strain is:

$$\varphi(\varepsilon, \nu) = \left(\frac{\varphi_0}{(1+\varepsilon)(1-\nu\varepsilon)}\right) \qquad \text{Equation 3.2}$$

where the denominator represents the increase in volume of the sample, ϕ_0 is the initial silver volume fraction, ε is the strain, and ν is Poisson's ratio. Equation 3.2 accounts for shrinkage in only the thickness dimension (i.e. assuming no decrease in width as a simplification). Combining Equations 3.1 and 3.2 gives the relative conductivity ratio as a function of strain, the inverse of which provided the resistivity ratio. When the line is stretched, the relationship between resistivity and resistance (see Equation 1.1) must also include the effect of strain on ink length, L and cross-sectional area, A:

$$R_\varepsilon = \left(\frac{\rho_\varepsilon L(1+\varepsilon)}{A(1-\nu\varepsilon)}\right) \qquad \text{Equation 3.3}$$

The above relations are modified to include the effects of strain localization through inclusion of a spatial inhomogeneity of the silver flake fraction, as measured in Figure 3-6 and Figure 3-7. For the unloaded 5025, the silver flake fraction can be represented by a Gaussian distribution, with a mean of 49 vol% and a standard deviation of 9%. After being strained to ε = 0.35, the flake fraction distribution shifted to a mean of 35 vol% with a standard deviation of 11%. The effect of an evolving silver flake distribution with strain can be obtained through modification of Equation 3.1. The conductivity along a printed line can divided into a series of short segments, where the loading in each segment is distributed in a Gaussian fashion. The origin of the disparate flake fraction areas may be the strain localization that creates segments that have low loading, and low conductivity, which exacerbates the increase in resistance of the printed line as a whole.

The impact of the uniform vs. localized strain on the resistance is examined for the 5025 ink through an evolving vs. non-evolving silver flake fraction distribution. For both

models, these are the parameters used for 5025: ν = 0.35, s = 2, φ_c = 0.13, σ_m/σ_c = 1e6, and φ_{max} = 0.8 (see Figure 3-8(a)). The ratio of the increase in resistance is very sensitive to factors like the percolation threshold, which is not known for the silver flakes used here. For spheres, the percolation threshold is φ_c = 0.18, but it will be lower than that for flake particles. Under uniform strain the model, per Equation 3.1, with an average loading expression [27] predicts a 2.6 times increase in resistance at 35% strain for the 5025 ink, which is much lower than the observed increase in resistance. Under localized strain, modeled by allowing the local flake fraction to follow a Gaussian distribution, the resistance is predicted to increase by a factor of 15 at 35% strain, which is similar to the experimental value (see Fig. 10(c)). Clearly incorporation of a non-uniform loading, as a way of accounting for the strain localization impact, results in a much higher increase in the resistance of a printed line. At the very least it presents better agreement, compared to the theoretical, with experimental data.

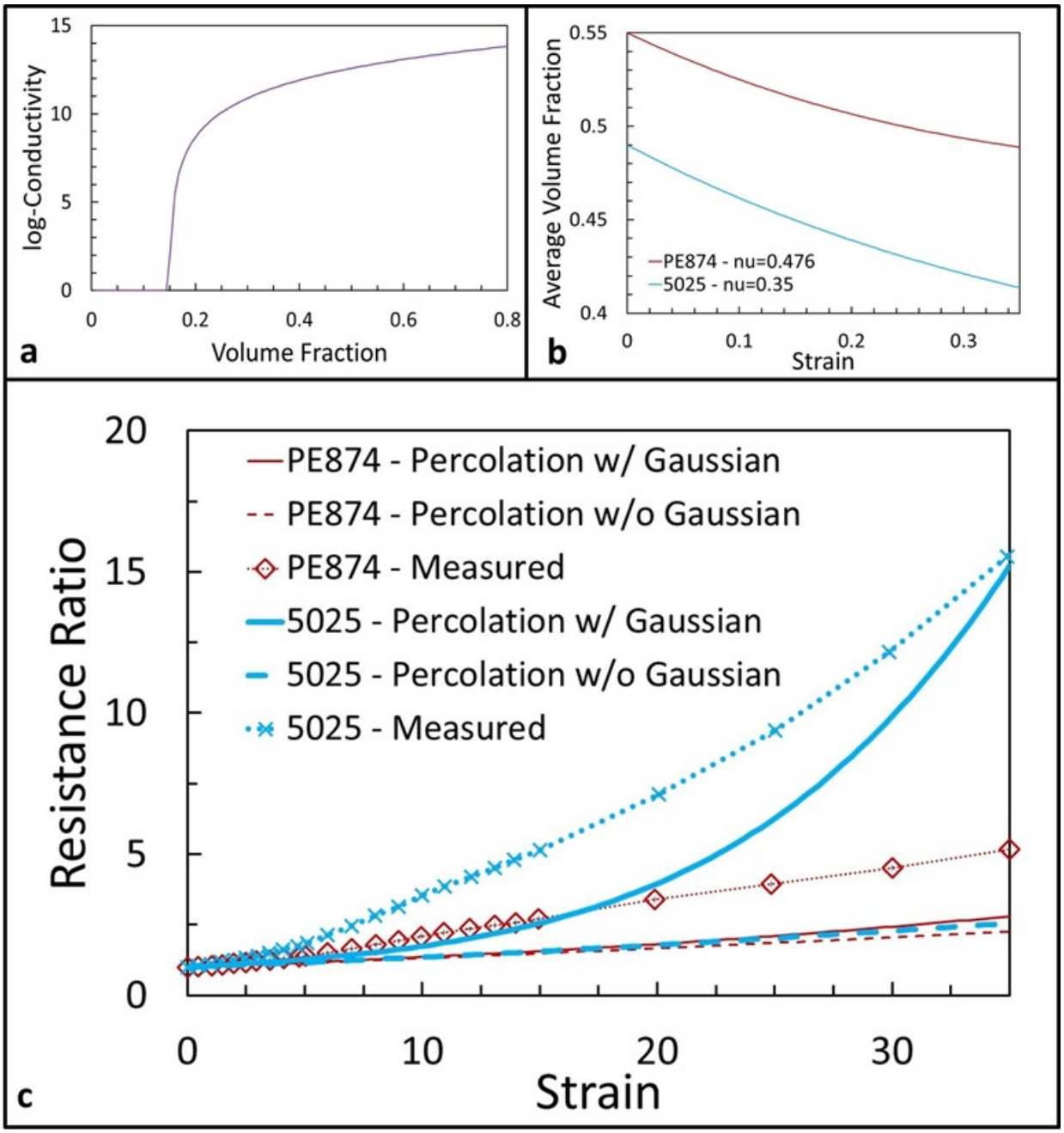

Figure 3-8: Numerical model predictions: (a) Conductivity (log scale) with increasing volume fraction for both inks (Equation 3.1) (b) Average flake volume fraction with strain (Equation 3.2) (c) Numerical model predictions of normalized resistance ratio vs strain

For the PE 874 ink only the following parameters are different from those used for 5025: an initial volume loading of 55 vol%, and Poisson's ratio of 0.476. For a non-evolving volume loading, Equation 3.1 predicts the resistance increase to be 2.3 times higher, not very different from the 2.6 resistance change for 5025. Incorporating the measured Gaussian distribution (see Figure 3-8(d)) did not result in any significant change (see Figure 3-8(c)) (2.8 vs original 2.3 at 35%) and does not wholly account for the experimental resistance ratio of 5 at 35%. The 5 times increase in resistance for PE 874 can be explained by recognizing the ink's resistance reduction is due to the appearance of surface cracks. When PE 874 is stretched, the distribution of flake volume loading did not change (see Figure 3-7(b) and 3-7(e)), which is inconsistent with Equation 3.2 predicting a decrease in flake fraction from 0.55 to 0.49 (see Figure 3-8(b)). This is likely the result of cracking (see Figure 3-4(d)), preventing deformation in adjacent areas, and therefore resulting in a constant flake fraction, and also leading to an increase in the void content (see Figure 3-7(c) and 3-7(f)). The response of this ink may be better modeled using porous metals where one phase is electrically conductive, but the void phase has no conductivity. It is known that the electrical conductivity of a metal decreases linearly with the introduction of pores at low porosity, with some curvature at higher values of porosity [32, 33]. If all the volume increase in the PE 874 is caused by an increase in void volume, then we would expect the electrical resistivity to increase linearly with the void volume, which matches the trend in the data.

3.6 Conclusions

In conclusion, this chapter highlighted the importance of the initial architecture of silver inks on the deformation and electrical behavior up to large strains (in excess of 30%).

While the investigated 5025 and PE 874 inks were expected to differ only in their polymer matrix properties, our FIB cross-sections revealed a large presence of micron-size voids in the PE 874 inks. Our in situ strain map analysis showed the formation of strain localization bands at early applied strain levels. These strain localization bands have different origins, which result in different flake volume fraction evolutions and therefore different electrical behavior. For PE 874, strain localization is associated with cracking, most likely triggered by the pre-existing voids, which leads to minimal silver flake volume fraction changes and a resistance ratio increase of 5 at 35% applied strain. Instead, for 5025, strain localization is accompanied by local necking which leads to large silver flake volume fraction decreases and a resistance ratio increase of 15 at 35% applied strain. Percolation theory can provide reasonable estimates of the resistance ratio increase with strain for 5025 if the Gaussian distribution representing the measured flake fraction (which captures non-uniform deformation) is used, compared to the use of average flake fraction (which better captures uniform deformation).

This work suggests the somewhat paradoxical conclusion that voids, which lead to cracks in the deformed inks, can be beneficial for their electrical behavior under large strains. Indeed, while presence of surface cracks means an increase in void fraction, and therefore an increase in resistance (increase in porosity), their formation prevents any significant decrease in flake volume fraction (especially in necked regions). Since these are only surface and not through-thickness cracks, their formation appears to be not as detrimental to the ink's overall electrical behavior. Investigating PE 874 inks with different initial void contents (presumably by optimizing the fabrication process) would be useful to

further understand the combined effect of voids and strain localization on electrical behavior under large strains.

CHAPTER 4. TRACE WIDTH EFFECTS ON ELECTRICAL PERFORMANCE OF SCREEN-PRINTED SILVER INKS ON ELASTOMERIC SUBSTRATES UNDER UNIAXIAL STRETCH

Submitted for Publication

Chapter 3 investigated the origins of resistance increase in a stretchable ink under strains up to 50%, which were attributed to early strain localization in the form of surface cracking. Since elongation was not continued beyond 50% applied strain, damage evolution has not been fully characterized until failure (open) occurs. Particularly, the occurrence of surface cracking warrants further investigation and particularly its interaction with trace width and line resistance changes. Therefore, in an effort to assess the current limitations of printed conductors, this chapter explores the strain thresholds, and their dependencies to trace widths, of PE 874 screen-printed onto TPU and subjected to uniaxial strain until electrical failure.

4.1 Sample Profilometry

Profilometry scans of each of the trace widths prior to elongation are shown in Figure 4-1(a). They reveal a shallow taper region of about 100-150 μm, across which print thickness in the direction of the center of the trace gradually rises from the substrate plane toward peak thickness levels. For every μm of thickness added, the taper extends approximately 14 μm toward the print line center. For w < 0.75 mm, print line thickness does not reach the nominal 8 to 10 μm. For w = 0.1 mm (resp. 0.25 and 0.5 mm), the thickness only reaches about 50% (resp. 75%) of the nominal value. When determining

resistivity values, these thickness tapers should be included by adjusting the cross-seciton area to that of a trapezoid, as shown in Figure 4-1(b).

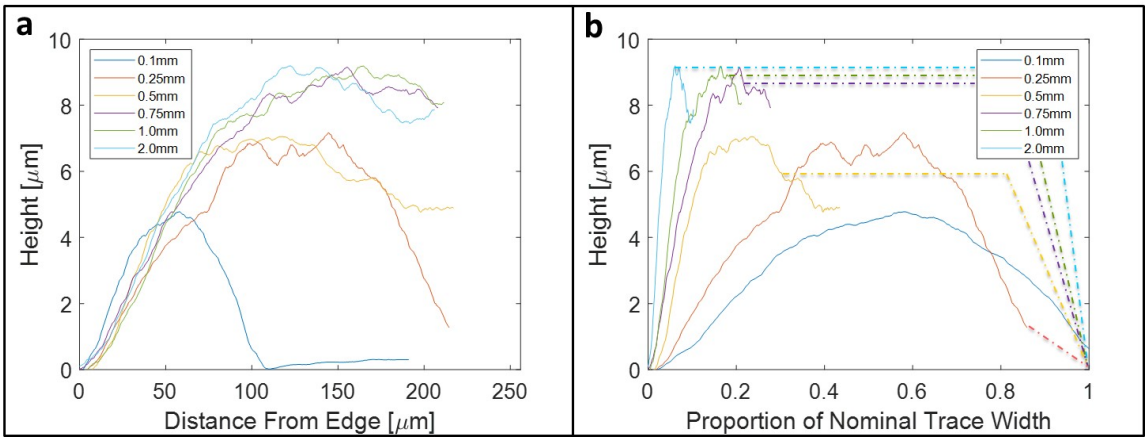

Figure 4-1: (a) Profilometry scans of untested samples, starting from edge of print line, for different specimen widths, w (b) Representaiton of print line cross section for different trace widths, w

4.2 Initial Characterization

Measured initial resistances of the print lines are shown in Figure 4-2(a). There is a high standard of deviation for w = 0.1 mm compared to the other trace widths. It should be noted that the yield of the w = 0.1 mm prints was only 10%. This means that 9 out of 10 prints of this size were open circuits in the unstrained condition, and not included in the measurements. This was due to line edge defects, which significantly reduced local trace width, resulting in discontinuities along the print length. Examples of such defects may be viewed in Appendix B. All other print sizes had 100% yield, and only specimens with measurable resistance values were used in elongation experiments.

The resistivity of the ink is calculated using Equation 4.1:

$$\rho = \frac{RA}{L} \qquad \text{Equation 4.1}$$

where R is the measured resistance, A is the cross-sectional area of the printed trace, and L is the length of the print line (76 mm). We consider two cross-sectional areas: the idealized rectangular cross-section, and a trapezoidal shape approximated from the profilometry scans.

$$A_{rec} = width \times height \qquad \text{Equation 4.2}$$

$$A_{trap} = \frac{(base_1 + base_2) \times height}{2} \qquad \text{Equation 4.3}$$

The idealized cross section uses the nominal trace width and nominal height of 10 μm. The trapezoidal approximation uses the nominal trace width as $base_1$, and the measured values for $base_2$ and height. The comparative results of Equation 4.1 can be seen in Figure 4-2(b). The idealized cross-section suggests a trace-width dependence for resistivity, which can be seen to be much higher for $w = 0.1$ mm . When we apply the trapezoidal correction using measured values, we find the resistivity to be relatively constant, at an average of 0.001±0.0002 Ω-mm, in agreement with values reported by the manufacturer (<0.0019 Ω-mm). We can conclude that trace width has no impact on resistivity, and therefore that the volume fraction of silver flakes in the taper region is likely the same as the areas of peak print line thickness.

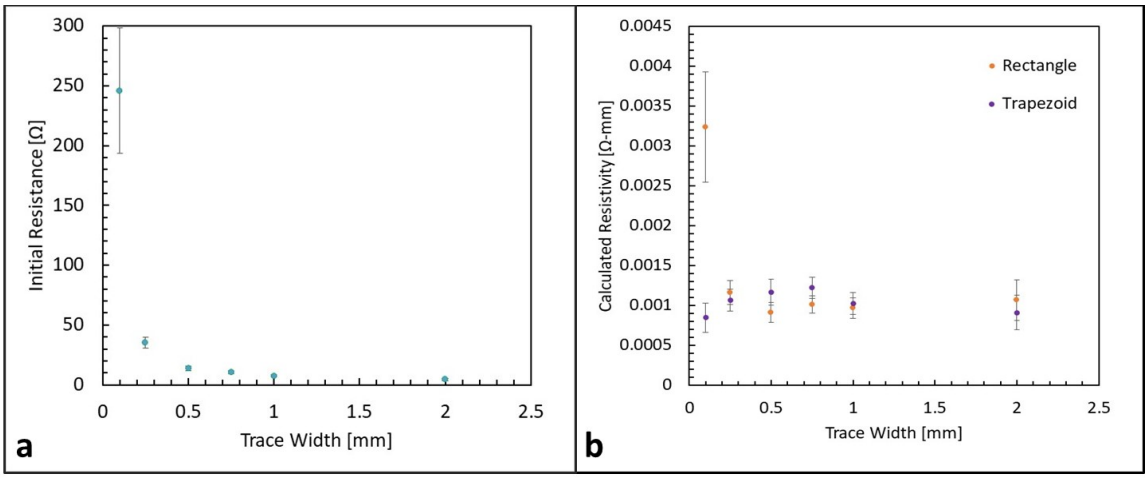

Figure 4-2: (a) Initial resistance, R_0, measurements for print lines as a function of trace width (b) Calculated resistivity values using idealized rectangular cross section and measured cross section more closely approximated to a trapezoid

To confirm that, a cross section cut from the edge of a printed trace may be seen in Figure 4-3(a). Analysis of the sectioned face (Figure 4-3(b)), revealed a 56% area fraction of silver flake inclusions, which is similar to that of the 55% bulk volume fraction reported by the manufacturer. It is also consistent with cross section analysis of the center of print lines performed in Chapter 3, which found flake fractions of approximately 55%. Figure 4-3(c) displays a portion of this cross-section at higher magnification, such that the disparity between flake, matrix, and void area is more apparent.

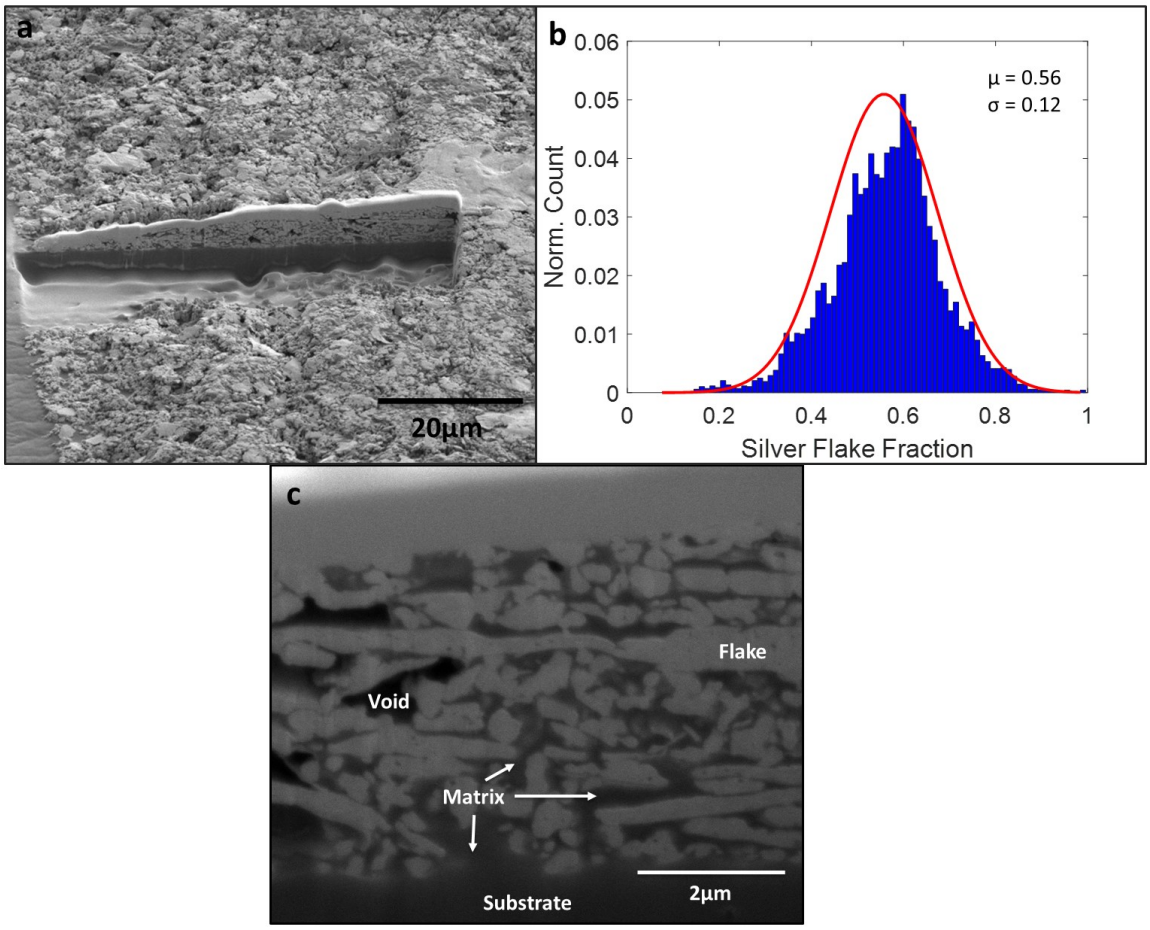

Figure 4-3: (a) Cross section from edge of PE 874 print, displaying tapered thickness (b) Calculated silver flake area fraction (c) High magnification image of PE 874 cross-section.

4.3 In Situ Results

Normalized resistance values versus applied far-field strain for the tested sample sets are plotted in Figure 4-4(a). Two idealized conductor models are also presented, and will be discussed later in this work. All trace width prints demonstrate similar trends: as elongation increases, so does the normalized resistance. Figure 4-4(b) shows a closeup within 10% applied strain indicating that over that range, the increase in normalized resistance is the same for all trace widths. For $\varepsilon_{app} > 10\%$, the resistance curves begin to

diverge, such that the lowest rates of resistance increase are associated with the widest print lines. This continues until a width-dependent threshold value, above which the resistance measurement becomes unstable (see Figure 4-4(a)). During instability, a given trace is still conductive, but the measurement values fluctuate wildly, sometimes by orders of magnitude. Eventually this behavior gives way to open circuit failure.

The respective threshold values for performance instability and open circuit measurements are presented in Figure 4-4(c). Overall, the threshold strain values increase with increasing w, and appear to reach a plateau for $w = 2$ mm, (strain thresholds are $\varepsilon_{app} = 147.8 \pm 5.1\%$ for instability, and $\varepsilon_{app} = 183.2 \pm 7.7\%$ for open circuit failure). As w decreases, the relative drop in strain threshold gets larger, especially for $w < 0.5$ mm. For $w = 0.1$ mm the line becomes unstable at $\varepsilon_{app} = 12.3 \pm 5.6\%$ and fails by $\varepsilon_{app} = 26.2 \pm 7.3\%$. These values are below the 30-50% strain range for wearable applications, and highlight the need to understand these size effects.

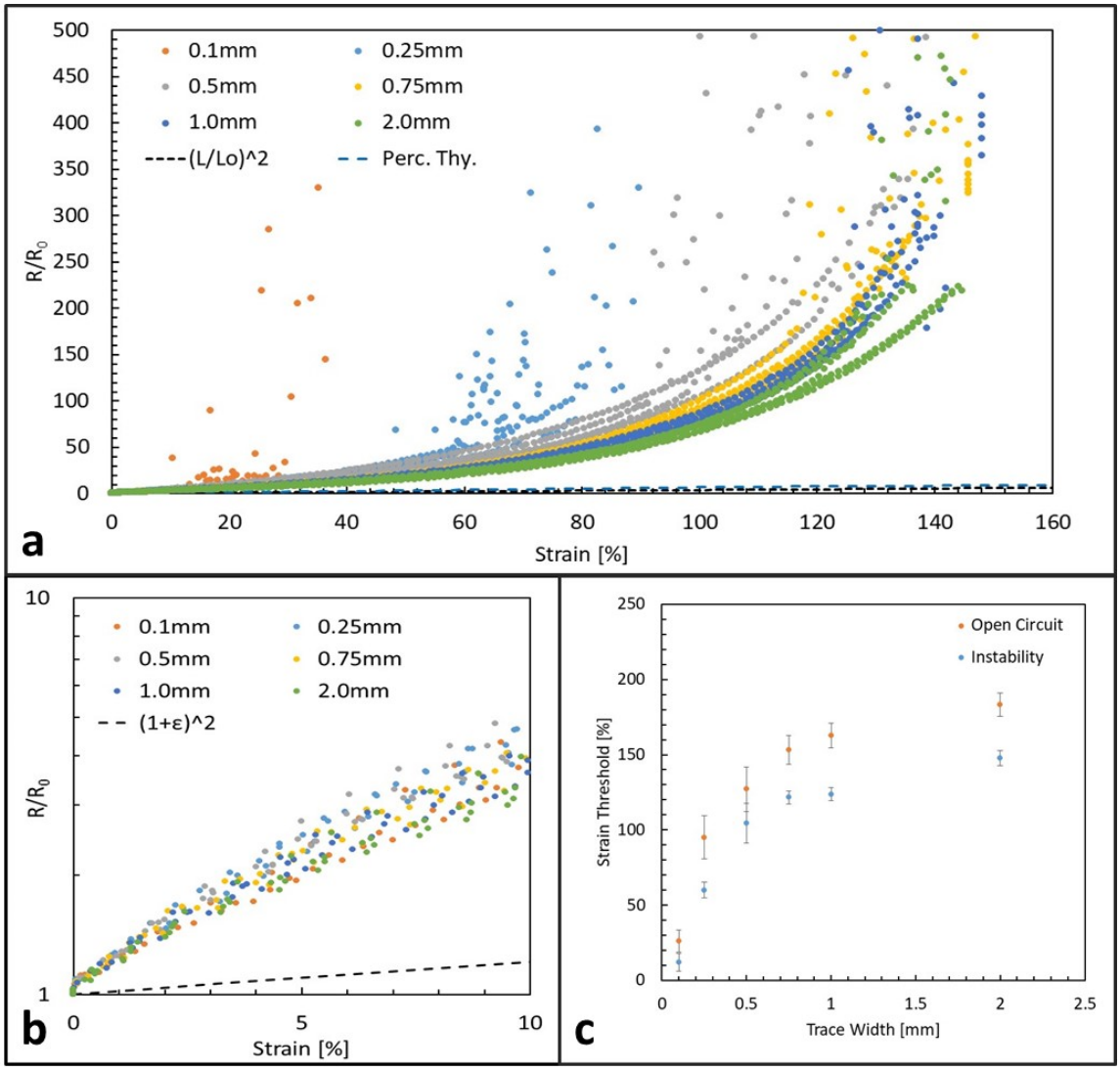

Figure 4-4: (a) Normalized resistance, R/R_0 vs. ε_{app} for tested trace widths (b) Semi-log scale normalized resistance, R/R_0 vs ε_{app} for ε_{app} = 1-10% (c) Instability and open circuit thresholds for respective trace width prints

4.4 Image Analysis

Surface scans for w = 2 mm were taken at incremental ε_{app} values up to 200%, which is beyond the threshold for open circuit failure. Some of the images, processed with associated crack pattern tracings, may be seen in Figure 4-5(a-c).

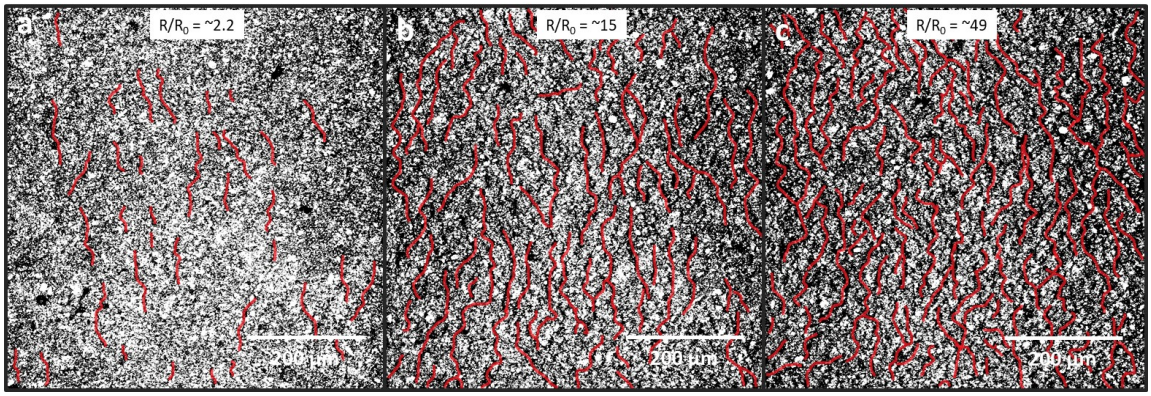

Figure 4-5: (a) w = 2 mm PE 874 on TPU, ε_{app} = 5% (b) w = 2 mm PE 874 on TPU, ε_{app} = 40% (c) w = 2 mm PE 874 on TPU, ε_{app} = 80%

Cracks were seen to nucleate as early as ε_{app} = 1%, and quickly coalesce into channels oriented perpendicular to the direction of elongation; they run across the printed trace line. This behavior may be quantified by the increase in max crack length with strain. For example, for w = 2 mm, cracks can be as long as 150 µm at ε_{app} = 5%, as seen in Figure 4-10(a). This length more than doubles at ε_{app} = 40% .

SEM images at higher strains may be seen in Figure 4-6, Figure 4-7, and Figure 4-8. While resistance was not measured during SEM image capture, the average resistance at that applied strain as measured from multiple tests for the same trace width is shown on the SEM images for reference.

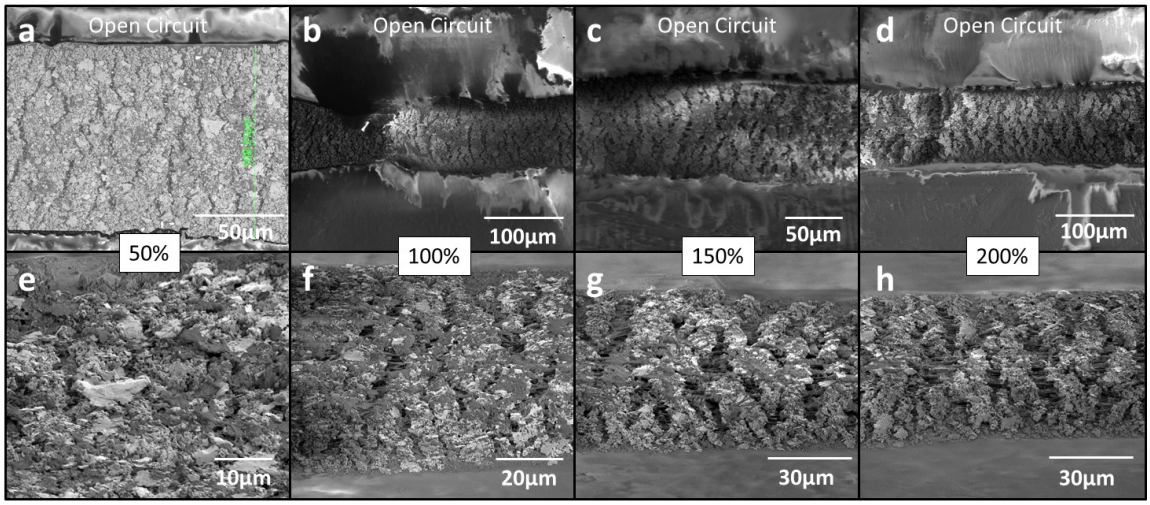

Figure 4-6: (a-d) Top-down and (e-f) inclined SEM images of ink surface (w=0.1 mm) for for ε_{app} = 50%, 100%, 150%, and 200%, respectively

Line edge roughness for w = 0.1 mm varies significantly, with some sections measuring just 50 µm across, and others exceeding the nominal value at closer to 120 µm. At ε_{app} = 50%, crack channels traverse fully across the print line. Given that this trace width completely fails electrically prior to this strain, it suggests that the cracks have contributed to the open circuit. With increasing applied strain, crack channels can be seen to widen dramatically, as the surface of the print breaks down from a cohesive print line into sequestered blocks of material.

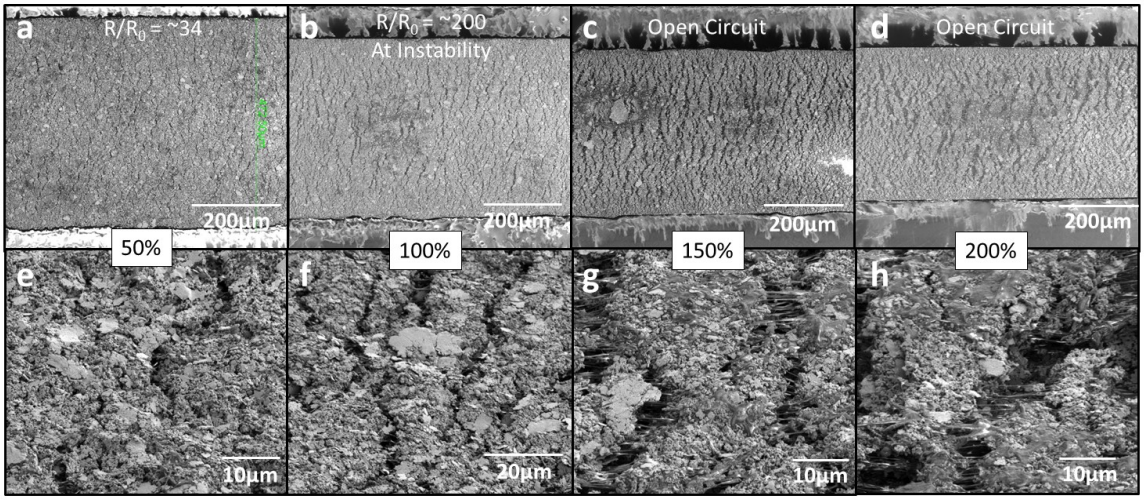

Figure 4-7: (a-d) Top-down and (e-f) inclined SEM images of ink surface (w = 0.5 mm) for ε_{app} = 50%, 100%, 150%, and 200%, respectively

For w = 0.5 mm (Fig. 9), we can see distinct crack channels at ε_{app} = 50%. At ε_{app} = 100%, crack density has increased, the channels have opened to as wide as 5 µm, and some have begun to laterally link. The trace resistance measurements vary wildly by this point, so crack geometry combined with lateral linkages are impacting the cohesiveness of conductive pathways. At ε_{app} = 150% and 200%, the circuit has failed. By this point crack openings are 10 µm, or even wider.

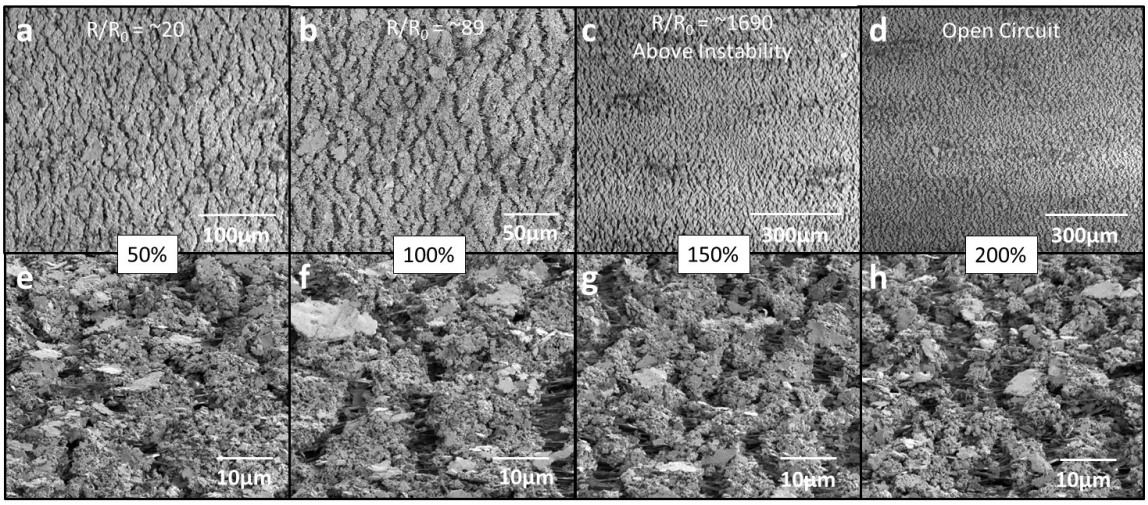

Figure 4-8: (a-d) Top-down and (e-f) inclined SEM images of ink surface (w = 2.0 mm) for ε_{app} = 50%, 100%, 150%, and 200%, respectively

The corresponding SEM images for w = 2.0 mm (see Fig. 10) reveal similar behavior to the narrower prints; surface cracks form and grow with increasing strain. At ε_{app} = 150%, just above the threshold for instability, the lateral linking of cracks is substantial. At ε_{app} = 200%, past circuit failure, the surface integrity of the print has completely broken down. Higher magnification images w = 2 mm at ε_{app} = 100% and 200% may be seen in Figure 4-9.

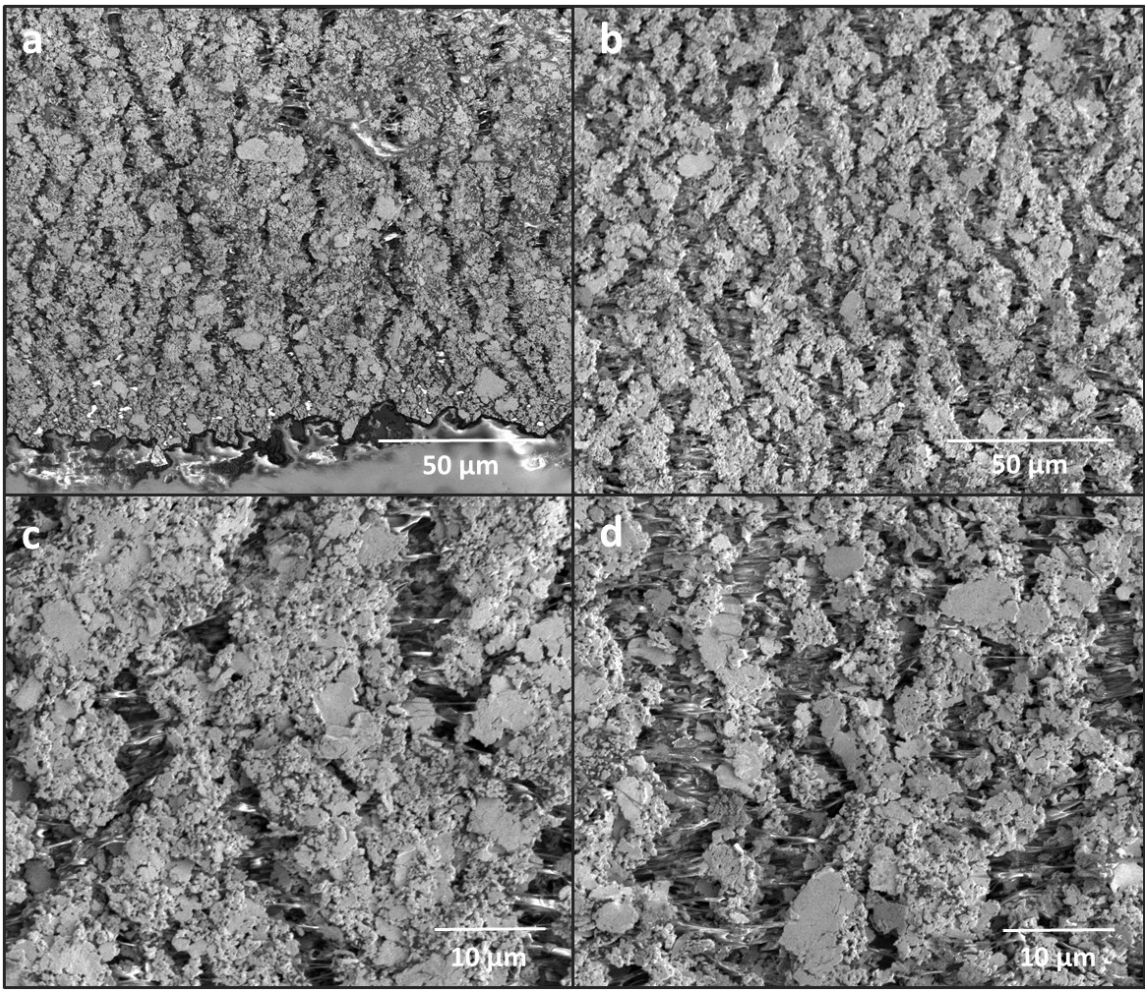

Figure 4-9: Low and high magnification SEM images of PE 874 with a 2mm trace width (a) w = 2 mm and applied strain, ε_{app} =100% (b) w = 2 mm, ε_{app} = 200% strain, showing widening of the surface cracks (c) high magnification, at ε_{app} = 100% (d) high magnification at ε_{app} = 200% strain showing crack tip openings approaching 10 µm across

These SEM images reveal that the crack openings, which measure around 5 µm at ε_{app} = 100%, have nearly doubled (~10 µm) at ε_{app} = 200%. Silver flakes are visible within the openings, suggesting potential conductivity at the bottom, closer to the substrate.

By measuring surface features identified by image analysis, we can measure in-plane dimensions such as length and width, as shown in Figure 4-10(a-c). Figure 4-10(a)

describes the peak lateral length for any surface openings found in a $w = 2$ mm trace under strain. At $\varepsilon_{app} = 5\%$, damage is already measurable to lengths of 150 μm. This steadily rises with strain, such that features are over 300 μm long at $\varepsilon_{app} = 40\%$.

Additional surface ruptures form lateral linkages (in the direction of elongation) of mature channels. This means the channel openings are not just widening with strain, they are also merging with other channels. Image filtering and analysis allows this to be quantified and displayed in Figure 4-10(b) and Figure 4-10(c), which compare relative crack sizes for $w = 2$ mm and 0.5 mm, respectively. When including lateral linkages, networked channels are considered single objects. Therefore, ΔX in Figure 4-10(b) and Figure 4-10(c) refer to the total width of an entire interconnected crack, which may be comprised of multiple channels and their connectors. This dimension is along the print line, in the direction of the applied strain and the elongation. ΔY similarly looks at the length running across a print, along the width direction. A single data point may comprise a connected formation of cracks which are vertically offset, for a larger composite length. In both $w = 2$ mm and $w = 0.5$ mm cases, crack network growth exhibits similar expansion behavior with increasing ε_{app}. From Figure 4-10(d) and Figure 4-10(e), we see the respective scatter fields overlap considerably at $\varepsilon_{app} = 50\%$, and continue to do so at $\varepsilon_{app} = 150\%$. Lateral linkages were observed in both cases, and appear to have the same along-print dimensional effect. Similarly, channel lengths continue to grow across the print.

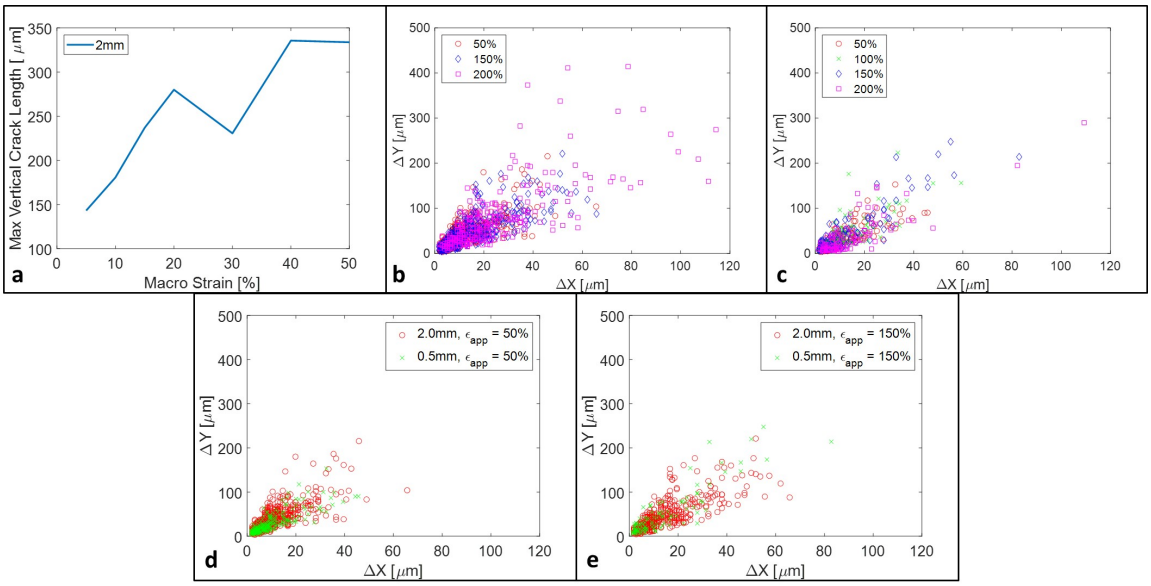

Figure 4-10: (a) Highest rupture length for w = 2 mm as a function of ε_{app}, derived from LEXT scans (b) Scatter plot of length (across print) and width (along print) measurements of damage formations in w = 2 mm PE 874 sample, derived from SEM images (c) Scatter plot of length (across print) and width (along print) measurements of damage formations in w = 0.5 mm PE 874 sample, derived from SEM images (d) Scatter plot of length (across print) and width (along print) measurements of damage formations in w = 0.5 mm and 2.0 mm PE 874 sample for ε_{app} = 50%, derived from SEM images (e) Scatter plot of length (across print) and width (along print) measurements of damage formations in w = 0.5 mm and 2.0 mm PE 874 sample for ε_{app} = 150%, derived from SEM images

4.5 Discussion

4.5.1 Comparison to Metallic Films

The observed surface damage in PE 874 with strain is reminiscent of the strain-induced cracking which also manifests in metallic thin films (thickness of around 1 μm) on polymer substrates [35, 42, 53, 84-87]. However, the strain-induced damage in metallic films is associated with propagating channel cracks whose depth is equal to the film thickness [36] and causes a sudden geometrical discontinuity that affects local resistivity.

As a result, numerous studies have shown that the normalized resistance vs strain curve follows two regimes for these systems: prior to onset of cracking, the normalized resistance follows the $(1+ \varepsilon_{app})^2$ trend [53], a geometrical model that assumes constant resistivity with ε_{app} and constant volume; and upon cracking, a departure from this model, with larger increases in normalized resistance. The onset of cracking depends on several factors, including film thickness, grain size, and substrate, and varies from ε_{app} of a few % to tens of % [42, 53, 85-87]. Upon cracking, the normalized resistance can be estimated with models incorporating average crack length and network density [88, 89]. The channel cracks quickly traverse through the specimen width with increasing ε_{app}, which explains why they fail at low strains, typically not exceeding 20% [84].

In contrast, the observed surface cracking in the stretchable PE 874 ink is significantly different in that it does not involve the propagation of sharp through thickness cracks, but is instead more reminiscent of ductile crack growth. Strain localization manifests from the outset of deformation (ε_{app} = 1%), which we previously attributed to the presence of voids, also shown in Figure 4-3. These channels of localized deformation eventually evolve into cracks that are visible at larger strains (ε_{app} = 2-4%); the depth of these cracks is only a fraction of the ink thickness when they form. As a result of this early strain localization, the normalized resistance curve for PE 874 does not follow the classical $(1+ \varepsilon_{app})^2$ trend, even before cracks can be observed; see Figure 4-4(b). This means that the electrical performance of metallic films is better (lower normalized resistance) than PE 874 at low strains (<4%). However, the trend is reversed at larger strains, due to the different nature of the observed cracking.

4.5.2 Trace Width Effects

From the initial resistance measurements and the topographical scans of the print lines, we can quantify the geometric resolution capabilities for screen printing of this PE 874 at various features sizes. Below $w = 0.75$ mm, thickness is dependent upon line width, such that a single pass print does not provide 8-10 μm of film thickness due to the edge taper. The $w = 0.1$ mm prints can only achieve half of the nominal thickness value, while the edge roughness indicates poor width control, and high variability in resistance (when functional at all), at this size. Corrected resistivity calculations, along with cross section analysis, reasonably show that ink microstructure does not change between the taper region and the peak thickness sections of the print lines.

Analysis of damage behavior shown in Figure 4-10(a-c) confirms that surface cracks both deepen and widen with increasingly applied strain. Instability is likely reached when individual crack channels approach full ink depth, or otherwise a sufficient depth and width such that any remaining silver flakes beneath the crack are too spaced apart to percolate. Lateral linkages exacerbate this effect by eliminating inter-crack conductive pathways.

With respect to trace width, we can see that cracks reach over 200 μm across a trace at $\varepsilon_{app} = 150\%$. This length represents 10-15% of the overall print width for $w = 2$ mm, but as much as 50% for $w = 0.5$ mm. Note line width decreases with increasing applied strain due to Poisson effects. In addition, the narrower lines have a lower thickness, due to the tapered region. Therefore, they are likely more sensitive to channel depth than a larger print. This explains why instability and open circuits occur earlier for narrower print lines; the depth penetrates a larger percentage of the line thickness, and the length and interconnectivity of the channels traverse a greater percentage of the line width.

For this specific ink, improvements to screen printing processes that would yield nominal thickness values in deposition may enhance reliability of the material at small feature size, such that channels must deepen further to fully sever the conductive line. Investigations into multiple pass prints may offer a short-term solution. Above all, the ink formulation should be explored to determine how to prevent surface tears. This could come from elimination of the voids found within the composite, or possible replacement of the conductive inclusions with alternatives that can be more uniformly distributed within the polymer matrix. Further exploration of the tear pattern evolution within these inks through in-situ, SEM imaging would be useful in tracking the progression of channel depth with strain as well as the local evolution of silver flake fraction in order to provide accurate modeling of resistance evolution.

4.6 Conclusions

This work has determined the effects of printed trace width on the origin of the electrical behavior of PE 874 on TPU under uniaxial stretch. The narrower prints (w = 0.1 mm) reach instability as early as ε_{app} = 12.3±5.9%, and fail completely at ε_{app} = 26.3±7.3%. This rises to ε_{app} = 121.7±4.4% and 153.1±9.6%, respectively for w = 0.75 mm, and ε_{app} = 147.8±5.1% and 183.2±7.7% for w = 2 mm. These failure thresholds are the result of strain-induced surface cracks, which sever the conducting cross sectional area of the printed line. As ε_{app} increases, the damage forms channels oriented perpendicular to the direction of elongation, which proceed to elongate across the printed line, as well as deepen into the thickness of the material. They also link laterally, forming networks measuring upwards of 400 μm long. The observed trace width effects on failure thresholds were rationalized as follows.

First, the damage geometry represents a significant proportion of printed feature size for smaller widths. For example, for w = 0.5 mm at ε_{app} = 50%, the damage network is made of interconnected cracks whose length represents 32% of total width after accounting for Poisson effects. Second, artifacts of the screen printing process further affect printed width and thickness for w < 0.75 mm. Edge roughness is observed to be several tens of μm, a significant value if the desired nominal width is a fraction of a mm. The 100-150 μm wide taper regions on either side of the printed line limit deposition thickness, meaning the surface cracks, for a given depth, have a more detrimental effect on resistance

Much of this work covers damage evolution from the 2D perspective supported by surface image capture, with inferences made about channel depth from qualitative observation. Future efforts to capture depth progression with strain, such as through *in situ* SEM, would help compose a 3D damage model. In this manner, we can determine the precise relationship between surface cracks and pre-existing voids found within the ink.

CHAPTER 5. ELECTRICAL PERFORMANCE EVOLUTION AND FATIGUE MECHANISMS OF SILVER-FILLED POLYMER INK UNDER UNIAXIAL CYCLIC STRETCH

Submitted for Publication

The evolution of the heterogeneous conductive composite ink during monotonic stretching has been presented in Chapter 3: strain localizations manifest themselves into extreme necking, in the case of 5025 ink, or surface cracking, for PE 874. Chapter 4 explored the cracking behavior in PE 874 with respect to manufactured feature sizes, and correlated strain induced damage progression with electrical performance failure thresholds.

Real world applications of these inks necessitate repeated strain cycling. This chapter explores reliability behavior for 5025 and PE 874. For 5025 we examine cycling of 0.5 mm wide prints while supported by PET, as intended by the manufacturer. Due to the limited elastic regime of PET, we maintain low mean strain and amplitudes. PE 874 was designed for greatest compatibility with TE11C. Based on the findings of Chapter 3 and Chapter 4, we examine strain values beyond the COS of a few percent for surface crack nucleation, but below the previously identified thresholds for instability or failure from uniaxial strain. Predominantly, 0.5mm wide PE 874 prints were examined, with uniaxial strain values as low as 5%, and as high as 80%. Note the recognized threshold for instability at this feature size is over 100% applied macro strain.

5.1 Fatigue Results

5.1.1 5025 Cycling

As previously discussed, the low elastic regime of PET substrate necessitated restrictions on strain amplitude when cycling 5025. As such, amplitudes did not exceed 2.5%, while mean strain was limited to 10%. Figure 5-1(a) depicts the resistance of 5025 on PET increasing with cycle count. Tests were halted after 24-48 hours, or when cyclic softening of the substrate led to buckling a minimum strain levels. No samples experienced electrical failure in the form of either instability of resistance measurement, or open circuits. Normalizing for initial relative increases expected by loading to the mean strain values (see Figure 5-1(b)), results suggest that strain amplitude is a more significant driver of resistance. At the highest mean strain of 10%, the sample survives over 20,000 cycles with $R/R_0 = 8.5$. For the same mean strain, but an amplitude of 2%, the samples reaches the same R/R_0 after only 100 cycles.

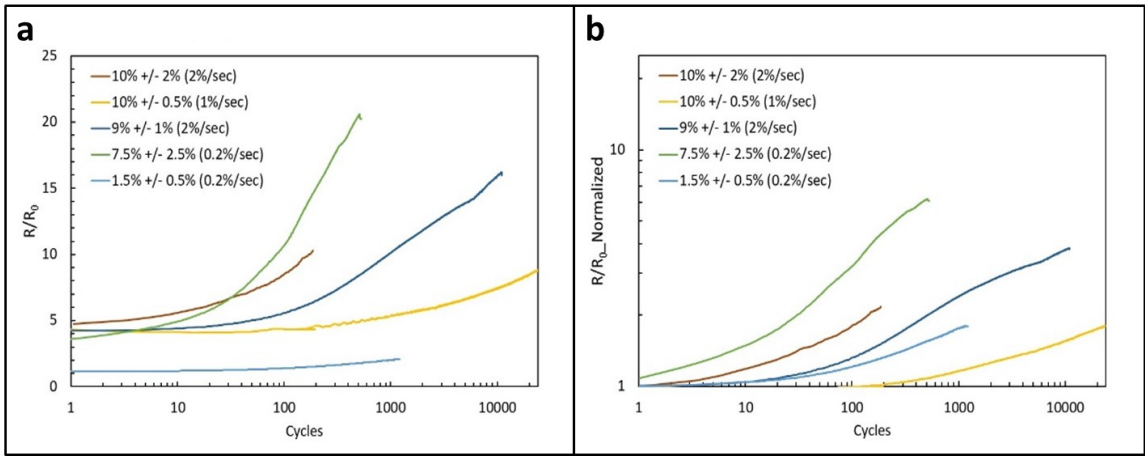

Figure 5-1: Strain cycling of $w = 0.5$ mm 5025 on PET with varying mean strains and strain amplitudes (a) Normalized resistance with cycling (b) Normalization of R/R_0 value to account for disparate mean strains between samples

When comparing samples cycled with the same amplitude, but different mean strains, there is minimal separation in resistance change as cycles progress. This is illustrated by Figure 5-2.

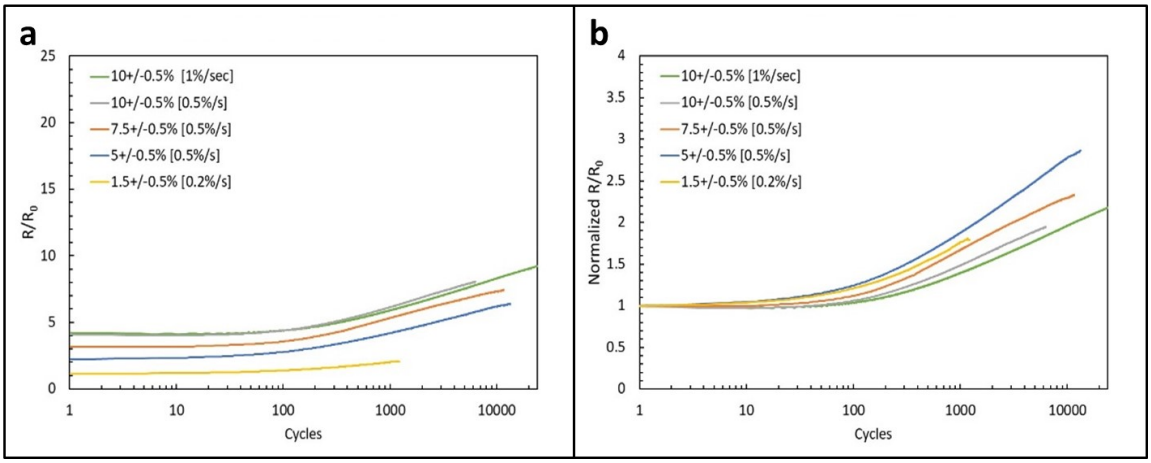

Figure 5-2: Strain cycling of w = 0.5 mm 5025 on PET with varying mean strains and common amplitudes (a) Normalized resistance with cycling (b) Normalization of R/R_0 value to account for disparate mean strains between samples

5.1.2 PE 874 Cycling

For PE 874 fatigue loading, during the first half cycle the conductive film will experience the same behavior as seen during the monotonic test. It is therefore, worthwhile to describe the surface evolution and effect on resistance during such loading. Under monotonic stretch, the normalized resistance in PE 874 increases with applied strain, as shown in Figure 5-3(a). In-plane strain maps obtained by analyzing the surface evolution using Ncorr [82] revealed that there is strain localization that occurs very early in the loading. The localization is manifested in the form of surface cracks, which can be seen in Figure 5-3(b) though 5-3(e). The network of surface cracks does not penetrate through the

thickness of the film, therefore maintaining some conductivity, although it is reduced from the unstretched configuration.

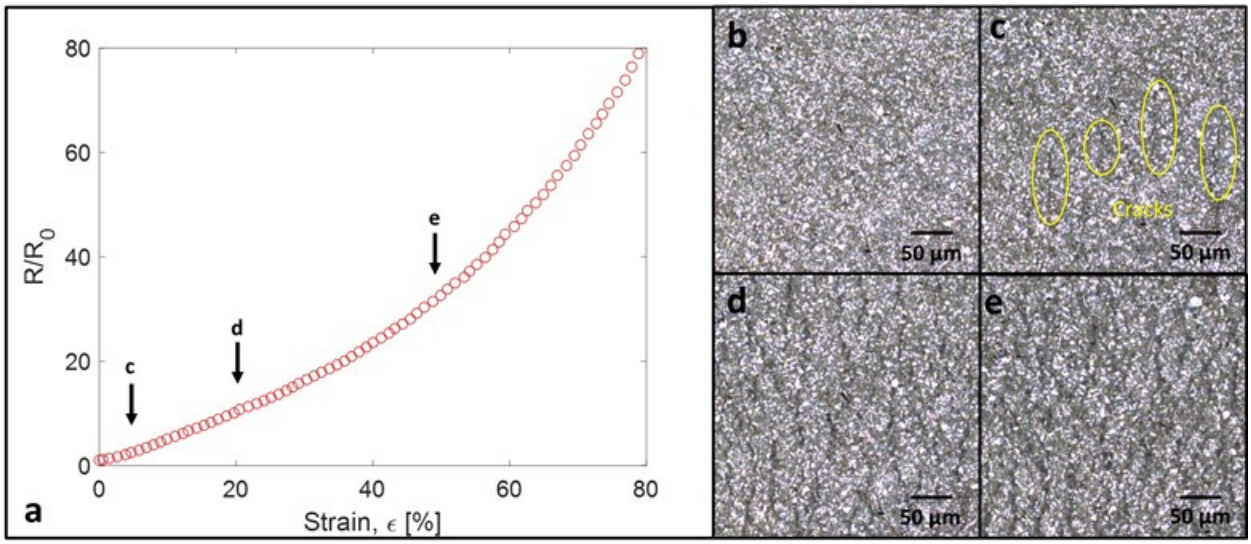

Figure 5-3: (a) Electrical response to monotonic strain for 2mm wide PE 874 printed onto TPU (b) PE 874 in test stage, undeformed (c) PE 874 with 5% applied macro strain, surface cracking begins to be visible (d) PE 874 strain field for 20% applied macro strain (e) PE 874 with 50% applied macro strain

During the first half cycle the resistance of the conductive print line increases while a network of surface cracks forms and becomes interconnected similar to what was observed in the monotonic test. As the applied strain decreases away from the peak strain value, the resistance decreases. However, under continuous cycling between two strain values, the relative resistance continues to increase from the initial (monotonic) values. Figure 5-4(a) illustrates the fatigue behavior for the first 30 cycles of a 0.5mm sample elongated between 50% and 80% applied strain. The change in resistance is added to the initial measurement for the region being stretched, and normalized against this initial measurement. Figure 5-4(b) shows this same test continued to just under 150 cycles. At approximately 75 cycles, the resistance change behavior reaches an inflection point, where

the relative difference between peak and valley resistance rises more rapidly and begins to become unstable. In many instances the measurement reads an open circuit near ε_{max}, and then returns to measurable levels at ε_{min}. This general trend is illustrated by the normalized resistance envelope outlined in red in the plot. The cyclic behavior is compared to that of a separate sample subjected to only the initial monotonic elongation and then held at ε_{max} for the duration of the test, as shown in green in Figure 5-4(c). After a brief reduction in resistance, the electrical performance of the static sample remains constant. Therefore, strain cycling of samples leads to additional increase in resistance compared to a monotonic stretch and hold.

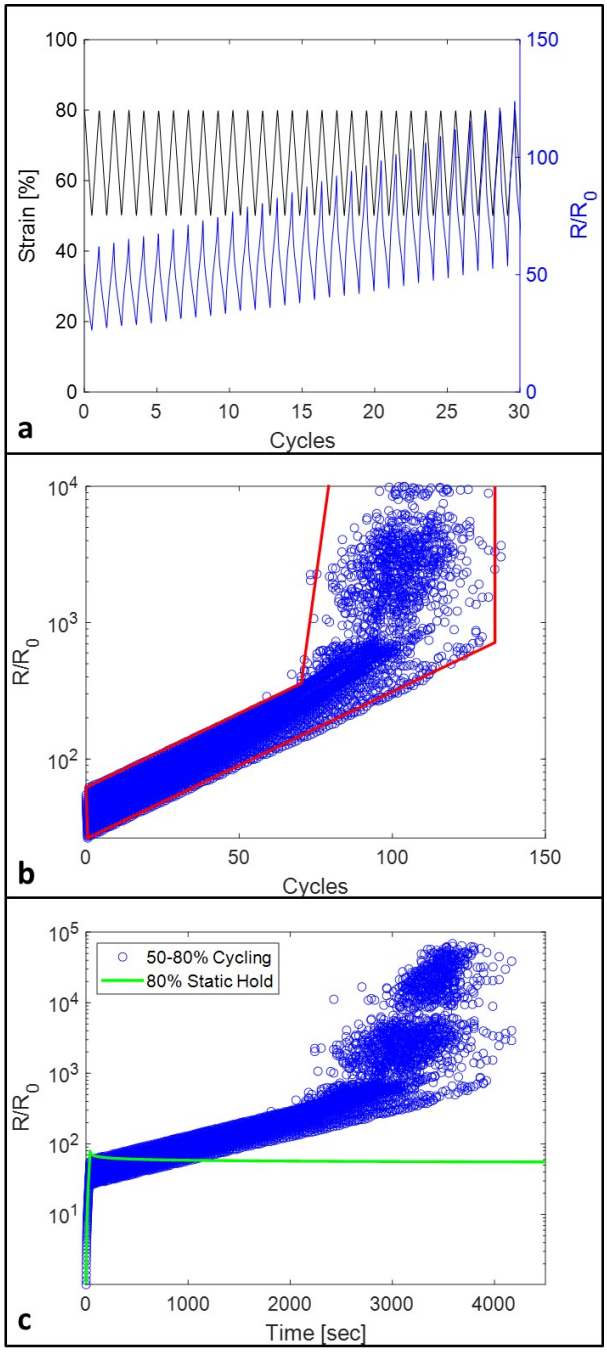

Figure 5-4: (a) First 30 cycles of 0.5mm wide PE 874 print strained between 50% and 80% (strain range: 30%, mean strain: 65%) (b) Full trial data set for 0.5mm wide sample cycled between 50% and 80% strain. The red behavior envelope encompasses the majority of the normalized resistance values, including open circuit measurements not seen in plot (c) 0.5mm wide sample cycled between 50% and 80% strain (blue), inclusive

of initial elongation from zero, superimposed by separate 0.5mm sample elongated to 80% and held at constant strain (green)

The failure limit, also known as fatigue life, N_f, is expressed as the number of strain cycles required to reach a designated performance threshold. Since the measured resistance for PE 874 samples subjected to 80% strain is nearly 80 times the pre-strained value, a threshold of $R/R_0=500$ is selected for this work as the fatigue life performance limit. This becomes the unifying metric across all of the varied experimental case parameters, which include strain amplitude, mean strain, print line width, and strain rate. By mapping the fatigue life for each experiment, one can identify the parameters of strain cycling which hold the greatest influence over resistance change behavior. Figure 5-5(a-b) show significant influence of strain amplitude, ε_a, on cycle count to reach the normalized resistance limit, from 23 cycles at 35% to an average above 500 cycles at 5%. Furthermore, sensitivity to mean strain, ε_m, seems to depend on the strain amplitude. Above ε_a = 15%, the fatigue life does not appear to depend as much on mean strain. Below ε_a = 15%, the disparities become more significant. This is illustrated by the spread of failure points in Figure 5-5(a), and the visible difference in slopes of the trend lines in Figure 5-5(b). At ε_a = 10%, a mean strain of 65% yields failure around 50 cycles. This nearly quadruples to 190 cycles with a drop to 40% mean strain or less. When ε_a = 5%, a 75% mean strain fails after just over 300 cycles but when the mean strain is 25% can extend the life to over 700. Trace width and strain amplitude are relevant parameters, but do not appear to significantly impact cycles to failure.

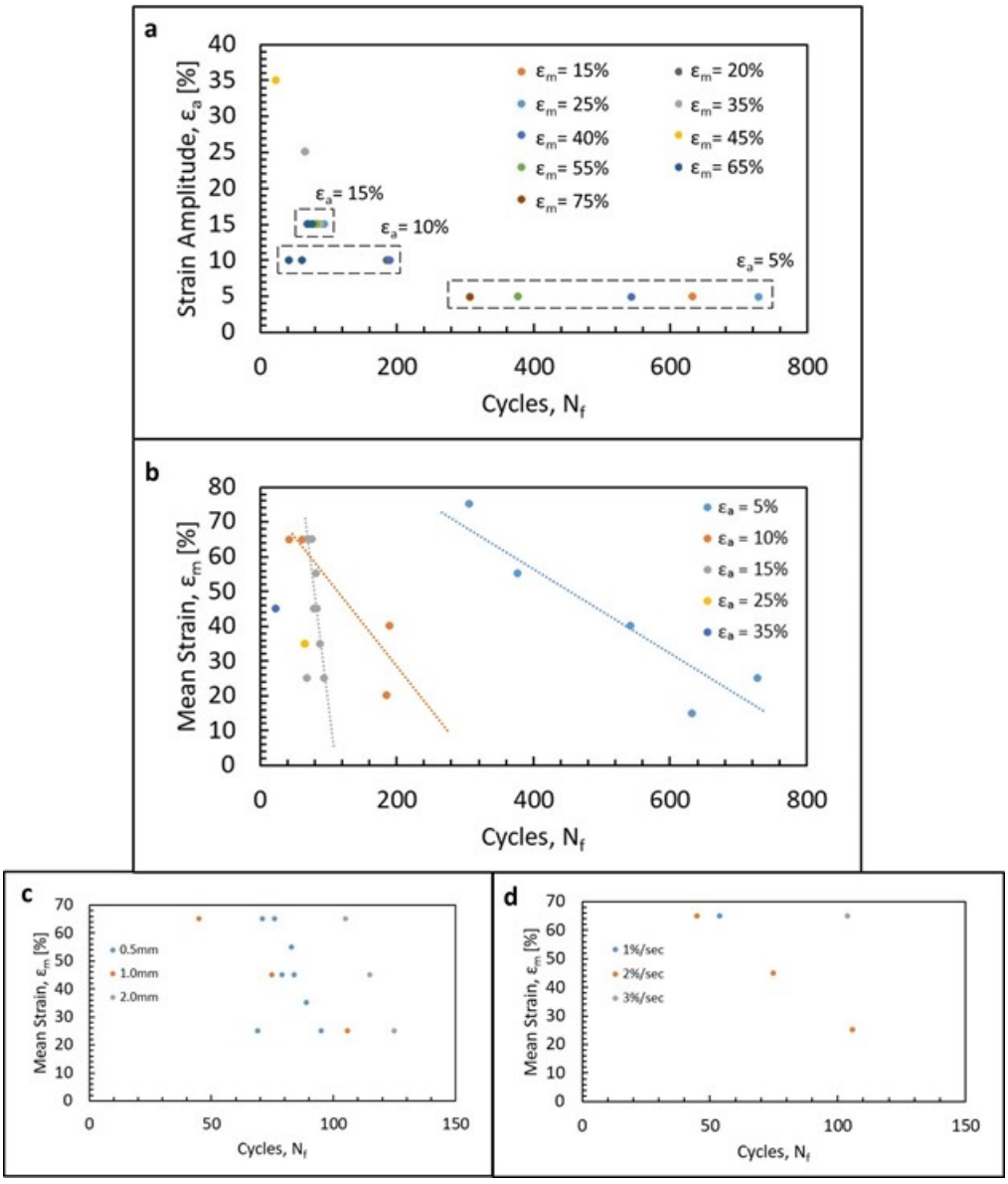

Figure 5-5: (a) Strain amplitude vs. cycles to $R/R_0 = 500$ for 0.5mm wide prints at 2%/sec strain rate (b) Strain life for 0.5mm wide prints at 2%/sec strain rate (Strain life for specimens subjected to 15% strain amplitude cycling at 2%/sec strain rate (d) Strain life for 1.0mm wide prints subjected to 15% amplitude cycling at varying strain rates.

Figure 5-6 illustrates in-situ resistance measurements for a 0.5mm wide print sample subjected to 100 cycles between 50% and 80% strain, with intermediate optical and laser profilometry scans every 10 cycles. The normalized resistance increases with cycling,

as already shown in Figure 5-4. Between cycle sets, the normalized resistance is observed to decrease. Comparison of these two experiments clearly highlights that the general resistance increase behavior is the result of strain cycling, and not time-dependent effects.

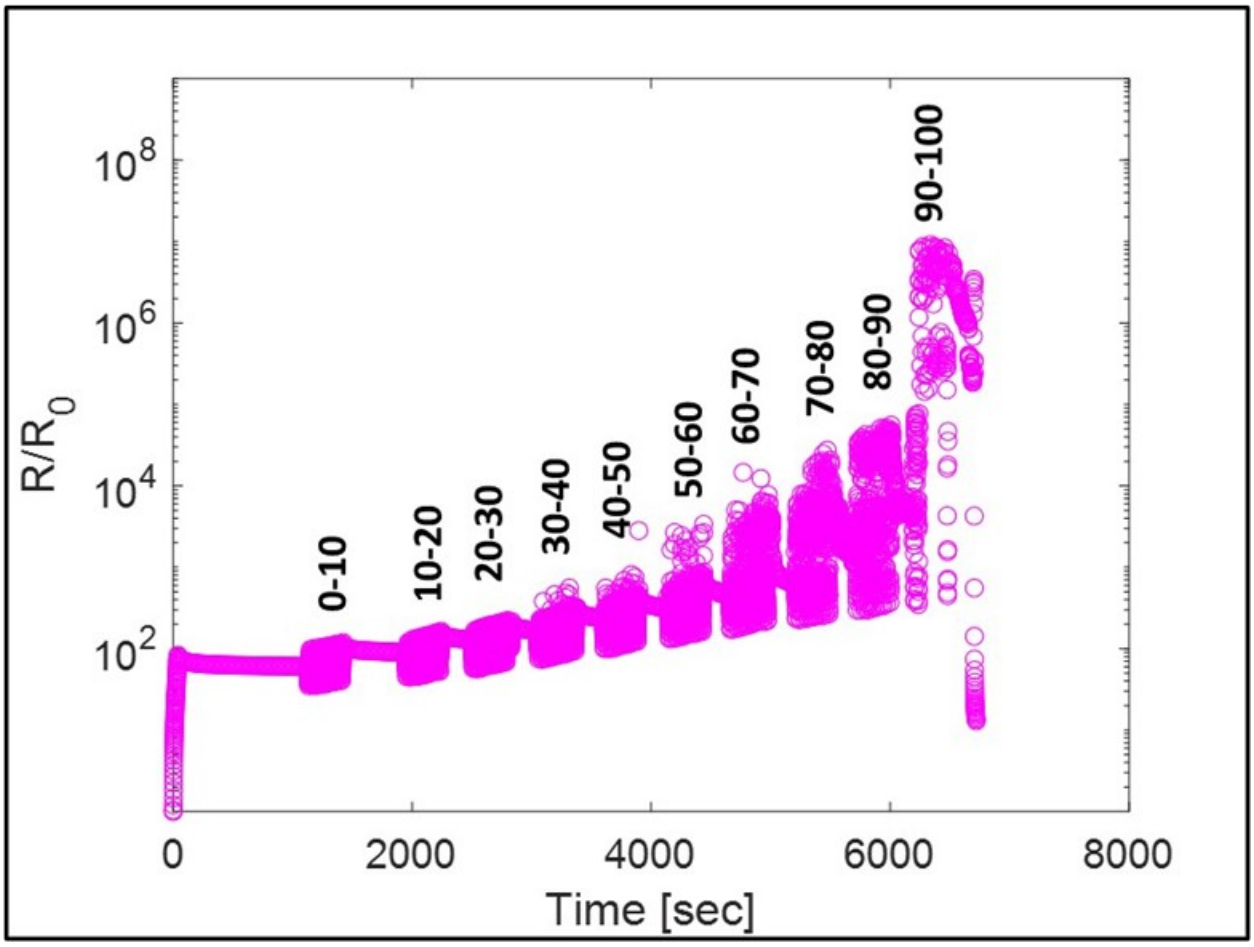

Figure 5-6: Normalized resistance behavior of 0.5mm print subjected to 100 cycles – in increments of 10 cycles – of 50% to 80% strain, with intermediate optical and laser profilometry scans

The 0.5mm wide print specimen in its unloaded state is displayed in Figure 5-7(a). When elongated to 80% strain, but before cycling commences, a network of extensive cracks is already present (Figure 5-7(b)), similar to the one shown for the monotonic stretch in Figure 2-5. Dominant crack channels are roughly oriented perpendicular to the direction

of elongation. The crack path is not a straight line, as might be seen in homogeneous metallic thin films, but bypasses around flakes. Due to the extensive cross-linking within the crack network, it is possible to trace pathways that span the entire ink line. Note, also, that the width of the hybrid ink decreases with applied strain due to the Poisson effect. Figure 5-7(c) shows the same sample after the stage has been rotated approximately 34 degrees to avoid interference with the objective lenses of the microscope.

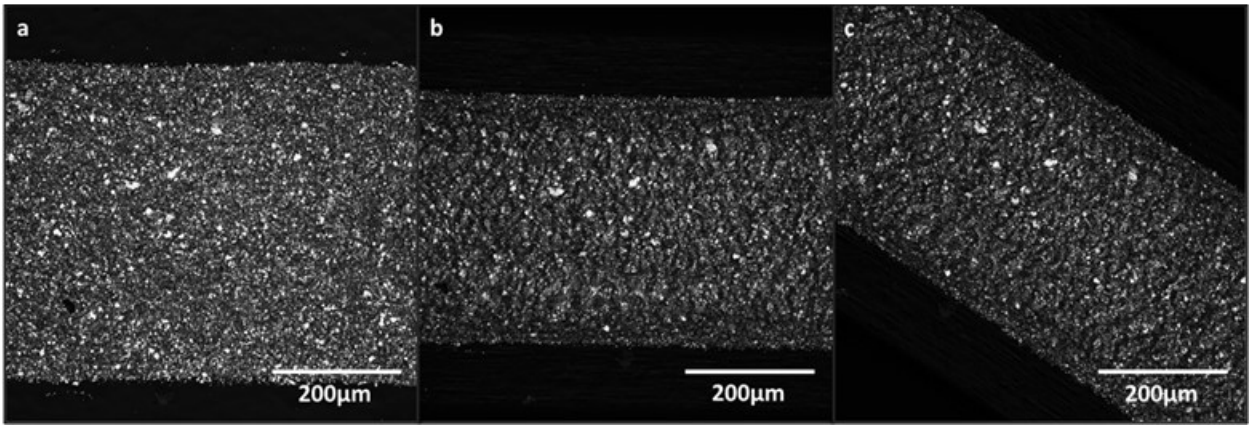

Figure 5-7: (a) 0.5mm wide print in unstrained condition (b) 0.5mm wide print elongated to 80% strain (c) 0.5mm print elongated to 80% strain, and rotated 34° to fit under confocal microscope

Figure 5-8(a) shows a 256 µm square area of the 0.5mm PE 874 print elongated to ε_{max} = 80%, but not yet cycled. Figure 5-8(b) shows the topographical image of the same approximate region following 100 strain cycles. The topographical features are compared using NCorr and the resulting displacement of the features before and after cycling is obtained. Once the respective topographies are aligned the resulting change in height between uncycled and 100 times cycled sets is compared, revealing the height delta field in Fig. 8c. These height differentials can be upwards of 8 µm, which is sufficient to

penetrate the entire thickness of the ink print when the resistance approaches that of an open circuit.

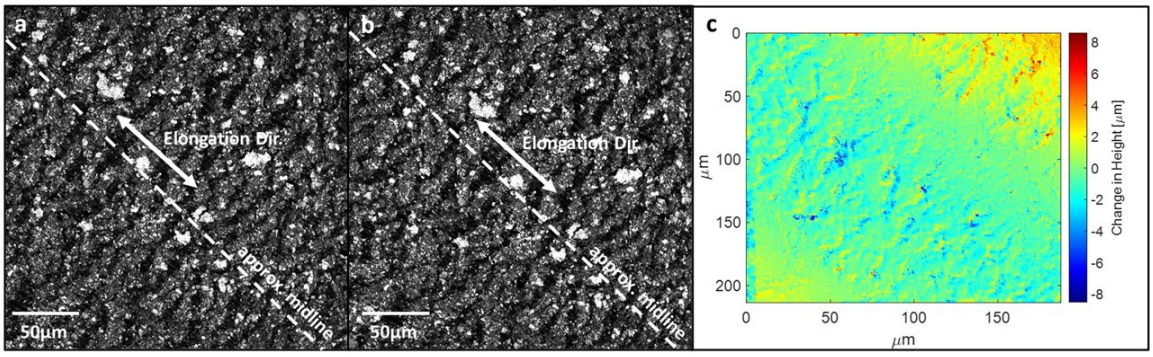

Figure 5-8: (a) 0.5mm print elongated to 80% strain, rotated, uncycled (b) 0.5mm print elongated to 80% strain, rotated, subjected to 100 strain cycles between 50% and 80% (c) Profile delta field between uncycled, and cycled specimen scans

5.2 Discussion

Results from both 5025 and PE 874 cycling suggest that strain amplitude is the most significant driver of resistance increase. This is supported by literature, which suggests strain amplitude leads to a reduction in conductivity and storage modulus due to the breakdown of conductive networks [90, 91].

Analysis of polymer matrix composites with conductive inclusions often uses percolation theory to describe the increase in resistance due to applied strain. As the material elongates, Poisson effects increase the volume of the polymer matrix by the relationship $V/V_0 = (1+\varepsilon)(1-\nu\varepsilon)^2$ where V and V_0 are final and initial volume, respectively, ε is applied macro strain, and ν is the Poisson ratio for the polymer matrix, presumed to be isotropic. By considering the inclusions to be rigid and undeformed, the

change in matrix volume due to elongation reduces the overall volume fraction of the inclusions, causing a decrease in conductivity. Cracking is not considered in this model, which explains its poor correlation to measured results for PE 874 in Chapter 3. The cracking within PE 874 is a significant contributor to electrical performance evolution with monotonic strain, and necessitates a departure from the standard percolation theory. Cracks reduce the effective cross-sectional area of the conducting line, much like in metallic films. Unlike in metallic films, however, resistance is still measurable once these networks span the full width of the trace; the line remains conductive. This indicates that the crack channels formed during the initial elongation do not penetrate fully through the film thickness and only do so after repeated cycling.

From image analysis, crack density is found to remain constant, as no new channels are observed to form between 0 and 100 cycles. The topographical scans point to a deepening of existing cracks within the conductive ink is the primary response to strain cycling. When channel depth is sufficient to penetrate the thickness of the ink, it exhibits the open circuit result commonly observed in homogeneous metallic films. However, total film penetration is not expected to happen simultaneously for every channel. Rather it is a gradual process, whereby the first occurrence among cracks can be marked by the inflection point in the resistance evolution plot. As more cracks reach full depth with continued cycling, the instability in resistance measurement becomes more pronounced.

As the applied strain is decreased from maximum, electrical conductivity returns within the specimen. This may be because the decrease in the crack tip opening displacement can possibly restore some of the broken conductive paths along the crack faces. Furthermore, the composite ink demonstrates a healing effect, whereby resistance

recovery occurs even at constant strain. Each successive round of 10 cycles applied to the sample under the confocal microscope was preceded by a period of decreasing resistance. This is likely driven by time dependent properties of the film, whereby internal stress relaxation allows for reorientation of the conductive inclusions, and the formation of new percolative pathways.

5.3 Conclusions

This chapter examined the behavioral response of both 5025 and PE 874 conductive ink when subjected to strain cycling. Both exhibit a fatigue-driven decay in electrical performance, which is accelerated by increased strain amplitudes. Surface cracks in PE 874 are created during initial elongation to ε_{max} forming an interconnected network of surface cracks. The hybrid conductive ink traces continue to remain electrically conductive for multiple cycles despite the presence of such defects. Performance failure comes from the deepening of these cracks to full film thickness. Crack deepening is affected by strain amplitude. At low enough strain amplitudes, the mean strain also influences the ink performance.

Future work will need to explore more closely the driving mechanism behind the deepening of the cracks in PE 874, and similar composite materials that exhibit such behavior. Polymer matrix failure due to fatigue, delamination between flakes and the matrix, or a combination of the two, are likely at play. Incorporation of in situ SEM into the experimental process would aid in this study.

CHAPTER 6. PRINT DEPOSITION THICKNESS AND VOID REMOVAL INVESTIGATIONS

This section explores parameters of the screen printing process, and compares theoretical film thicknesses with measured values for PE 874 ink. Exploration of size effects in CHAPTER 4 revealed the detrimental impact of the tapered thickness at the edges of prints, which reduces cross sectional area and makes the conductive line more sensitive to expanding strain-induced damage channels. Profilometry scans of double-pass, as well as triple-pass prints – printed and provided by DuPont – address how these tapers are impacted by multiple deposition steps.

CHAPTER 1 identified voids within the architecture of cured PE 874 prints. Post mortem cross section of PE 874 on PET suggested a role of these voids in influencing surface rupture due to applied strain. In an effort to further explore this impact, PE 874 samples was printed with modifications to the final curing process in an effort to eliminate these voids. DuPont provided PE 874 on TE11C which had been calendered post-cure, and in-house prints were created in lab here at Georgia Tech. These new samples were subjected to characterization per 3.2 and 3.4 for comparison against the original DuPont prints.

6.1 Double Pass and Triple Pass Profilometry Measurements

In addition to traditional single-pass prints, which dominates the experimental work discussed in this dissertation, DuPont provided additional print sets, whereby second and third deposition steps were performed. The intention was to provide thicker films at the same trace width to investigate the impact of this dimension on performance. While these

prints were not evaluated for electromechanical function, the thickness profiles are summarized in Figure 6-1.

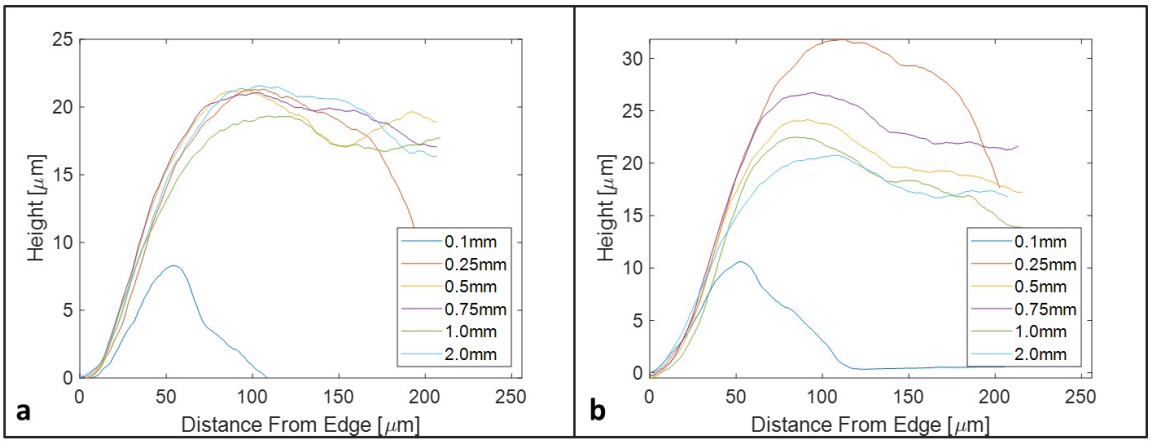

Figure 6-1: Profilometry scans for different PE 874 on TE11C widths, given (a) Two deposition steps (b) Three deposition steps

It is unknown whether any modifications were made to the relative distance between the screen and substrate between successive squeegee passes, or if additional ink was added prior to each pass. Theoretically, each pass should deposit an additional 8-10 µm on top of the previous layer. This clearly does not occur for the w = 0.1 mm prints, whose 10.8 µm peak after the third deposition step barely exceeds the 10 µm limit predicted for a single print. Qualitatively, the other widths successfully achieve a 16-20 µm thickness after the second deposition. By the third, there is significant variability in the amount of additional material added. The peak thickness value and relative additional material added from each pass is presented in Table 6-1.

Table 6-1: Peak thickness values of single, double, and triple pass print runs for each trace width, followed by relative change in peak thickness between print operations. All values reported in µm.

Trace Width	Single Pass	Double Pass	Triple Pass	2nd Pass Add	3rd Pass Add
0.1	4.78	8.31	10.60	3.53	2.29
0.25	7.17	21.33	31.81	14.16	10.48
0.5	7.05	21.20	24.16	14.15	2.96
0.75	9.15	21.08	26.72	11.93	5.63
1	9.19	19.34	22.49	10.16	3.15
2	9.19	21.59	20.76	12.40	-0.83
			Avg.	12.56	4.28

Note that the profilometry scans for each trace width were collected from separate samples, so the amount of additional material provided by deposition steps beyond the first are only approximate. As an example we would presume the "loss" of material for $w = 2.0$ mm is indicative of low deposition across one or more steps for that specific sample, rather than an actual loss of ink. Omitting the $w = 0.1$mm print, and taking the average of these peak thickness changes, we can infer from the 12.56 μm that a second pass print can reliably double the thickness of an ink pattern. The 4.28 μm average after the third pass indicates there is a complication which inhibits traditional ink deposition. A compilation of profilometry curves comparing thicknesses for common widths across different deposition amounts is presented in Figure 6-2.

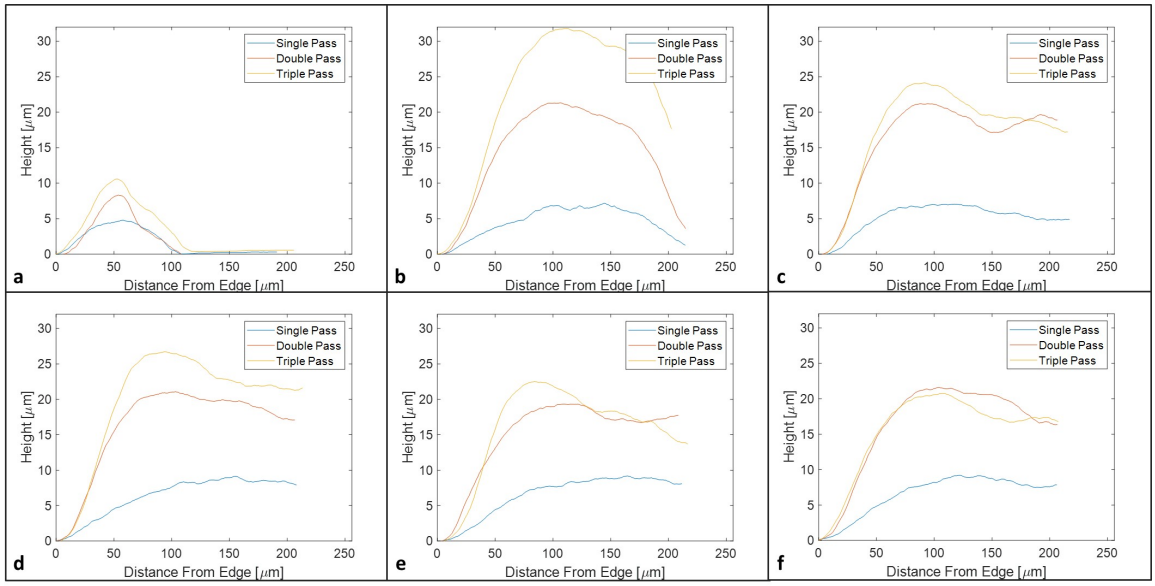

Figure 6-2: Comparison of thicknesses across different squeegee pass counts for 2 mm PE 874 on TE11C (a) w = 0.1 mm (b) w = 0.25 mm (c) w = 0.5 mm(d) w = 075 mm (e) w = 1.0 mm(f) w = 2.0 mm

Qualitatively the taper regions identified in CHAPTER 4 become steeper as thickness increases for the same print width.

6.2 Processing Modifications and Results

One of the most relevant discoveries made from initial cross-sectioning of these printed inks was the identification of voids within the cured PE 874 architecture, as described in 3.4. A potential explanation for this is the relative viscosity of the ink being sufficiently high such that any air bubbles trapped during the collapse of printed ink pillars (ref 1.2.4) are unable to escape before the curing process. Another explanation is that the volume loading of silver in the print, for the silver morphology used, is above the threshold for random loose packing. Voids are expected to appear in this case because as the ink dries, the silver structure is locked into place, dictating a certain dried coating thickness. However, there is not enough polymer binder to fill in all of the interstitial volume,

resulting in the formation of pores. This will be the case for any coating formulation where the filler particles form a jammed network, and there is not enough matrix to compensate for the open volume.

Given the potential relationship between sub-surface voids and the strain-induced surface cracking found in PE 874, it was of interest to determine if removal of the voids might yield superior electrical performance with strain.

6.2.1 Calendering

One suggestion made by DuPont was to prints through a calender setup, thereby supplying compression to the printed film, which might force collapse of the voids. This took place after samples were printed and cured. DuPont supplied a new print set of PE 874 printed onto TE11C substrate in 2020. In this batch, some sheets had been calendered either in one direction or in both directions along the length of the print design, while others were uncalendered for use as control specimens. Profilometry scans of a calendered 2mm print are presented in Figure 6-3 alongside a counterpart from the original 2018 print batch.

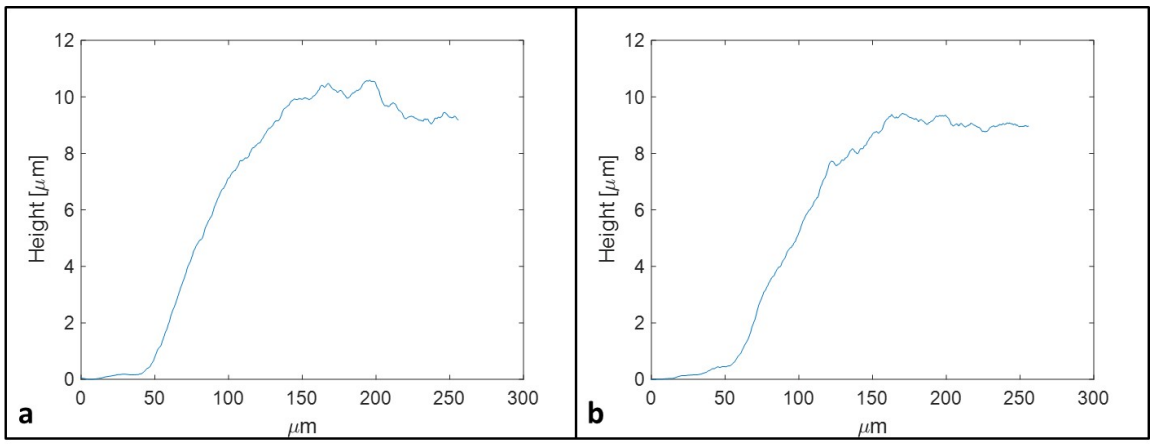

Figure 6-3: Profilometry scans of 2mm PE 874 printed onto TE11C (a) 2018 “original” print set (b) 2020 calendered sample

With the exception of the post-cure calendering, both samples were reportedly produced by the same printing process, and both fall within the nominal 8-10 μm dry thickness target reported by the manufacturer.

Resistance measurements in the unstrained condition of new print samples, both calendered and uncalendered, are compared to the electrical performance of the original prints (created in 2018) in Table 6-2. Recall that there were 10x 2mm PE 874 samples used in the size effects work presented in CHAPTER 4. These were uncalendered samples from the 2018 batch, repurposed for this chapter, and are labeled U_1 through U_10. Uncalendered samples from the 2020 batch are labeled U_11 through U_15. These prints present the lowest measurements at $R_{\varepsilon=0}$ = 4.1±1.0Ω. The uncalendered and calendered samples from the 2020 prints averaged $R_{\varepsilon=0}$ = 10.0±2.0Ω and $R_{\varepsilon=0}$ = 8.7±3.3Ω, respectively, which is more than double that of the original print set.

Table 6-2: Initial resistance values of calendered and uncalendered sample prints from 2018 and 2020

Printed in 2018 ←			Printed in 2020 →				
			Initial Resistance [Ω]				
U_1	4.8		**C_Up**	8.9		**U_11**	12.8
U_2	5.4			9.7		**U_12**	9.5
U_3	5.8		**C_UpDown**	15.3		**U_13**	9.5
U_4	3.9			6.1		**U_14**	10.8
U_5	2.9		**C_Down**	8.6		**U_15**	7.4
U_6	4.1			5.5			
U_7	3.2		**C_DownUp**	10.2			
U_8	2.8			5.3			
U_9	3.7						
U_10	3.9						
Avg.	4.1		**Avg.**	8.7		**Avg.**	10.0
Std. Dev.	1.0		**Std. Dev.**	3.3		**Std. Dev.**	2.0

These samples were monotonically tested as described in 2.2. When comparing the uncalendered 2020 prints to their 2018 counterparts (ref. Figure 6-4), electrical performance between the two print sets closely align for $0\% \leq \varepsilon_{app} \leq 75\%$. After this, the newer prints' resistance rises more steeply with strain. When adjusting to a semi-log scale for R/R_0, we see the disparity in strain location for instability field scatter.

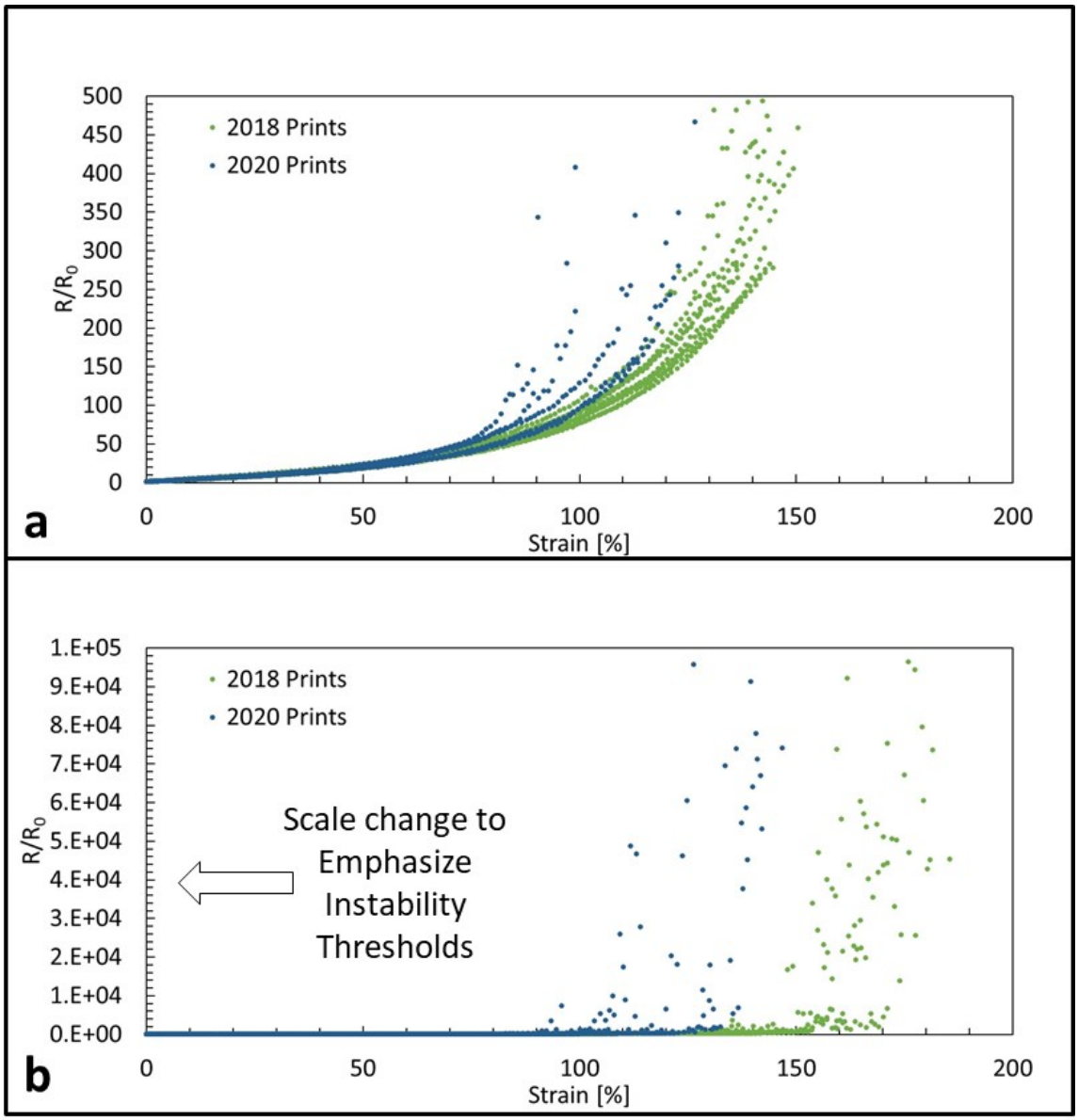

Figure 6-4: Normalized resistance, $R/R_{0,}$ vs. strain for uncalendered 2mm PE 874 on TE11C (a) linear scale (b) semi-log scale to emphasize instability field scatter with respect to ε_{app}

Combining these with the results from calendered sample testing (Figure 6-5),

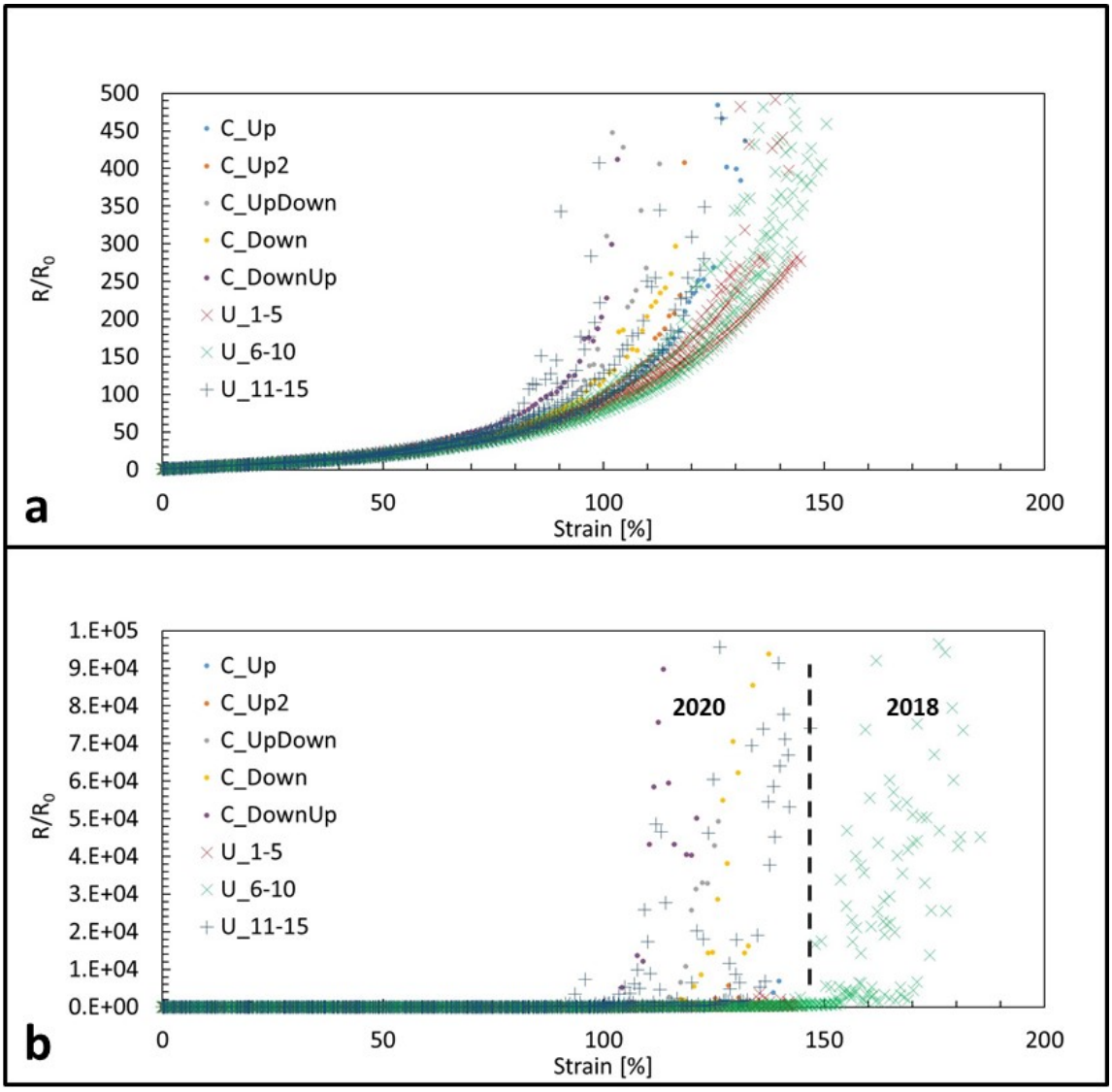

Figure 6-5: Normalized resistance, R/R_0, vs. strain for calendered and uncalendered 2 mm PE 874 on TE11C (a) linear scale (b) semi-log scale to emphasize instability field scatter with respect to ε_{app}

the performance of the calendered samples does not differ significantly with their uncalendered counterparts, and the previously identified trend of lower strain thresholds for instability and failure hold. These thresholds are summarized in Table 6-3 and Table 6-4. U_1 through U_5 are omitted from these tables because they were not subjected to sufficient elongation to reach open circuit failure.

Table 6-3: Instability threshold for uncalendered and calendered 2mm PE 874 on TE11C. The uncalendered samples are from the incumbent 2018 print set.

Printed in 2018 ←			Printed in 2020 →			
			Instability Threshold [% Strain]			
U_6	152.7		**C_Up**	124.9	**U_11**	85.819
U_7	140.2		**C_Up2**	118.5	**U_12**	121.5067
U_8	150.2		**C_UpDown**	99.7	**U_13**	124.0504
U_9	143.3		**C_Down**	105.4	**U_14**	100.2847
U_10	152.6		**C_DownUp**	103.2	**U_15**	112.8234
Avg.	147.8		**Avg.**	110.3	**Avg.**	108.8969
Std. Dev.	5.7		**Std. Dev.**	10.8	**Std. Dev.**	15.89663

Table 6-4: Open circuit threshold for uncalendered and calendered 2mm PE 874 on TE11C. The uncalendered samples are from the incumbent 2018 print set.

Printed in 2018 ←			Printed in 2020 →			
			Open Circuit Threshold [% Strain]			
U_6	187.9		**C_Up**	141.0	**U_11**	116.7495
U_7	177.3		**C_Up2**	133.8	**U_12**	148.39
U_8	187.1		**C_UpDown**	128.8	**U_13**	150.0948
U_9	171.4		**C_Down**	140.3	**U_14**	115.1095
U_10	192.3		**C_DownUp**	123.0	**U_15**	132.2361
Avg.	183.2		**Avg.**	131.5	**Avg.**	132.516
Std. Dev.	8.6		**Std. Dev.**	7.4	**Std. Dev.**	16.6782

The uncalendered 2018 prints reach instability and open circuit failure at ε_{app} = 147.8±5.7% and ε_{app} = 183.2±8.6%, respectively. The uncalendered 2020 samples do so at 110.3±10.8% and ε_{app} = 131.5±7.4%, while the calendered reach these thresholds at 110.3±10.8% and ε_{app} = 131.5±7.4%.

Both a calendered and uncalendered sample from the 2020 batch was FIB sectioned under the SEM. These sections are visible in Figure 6-6.

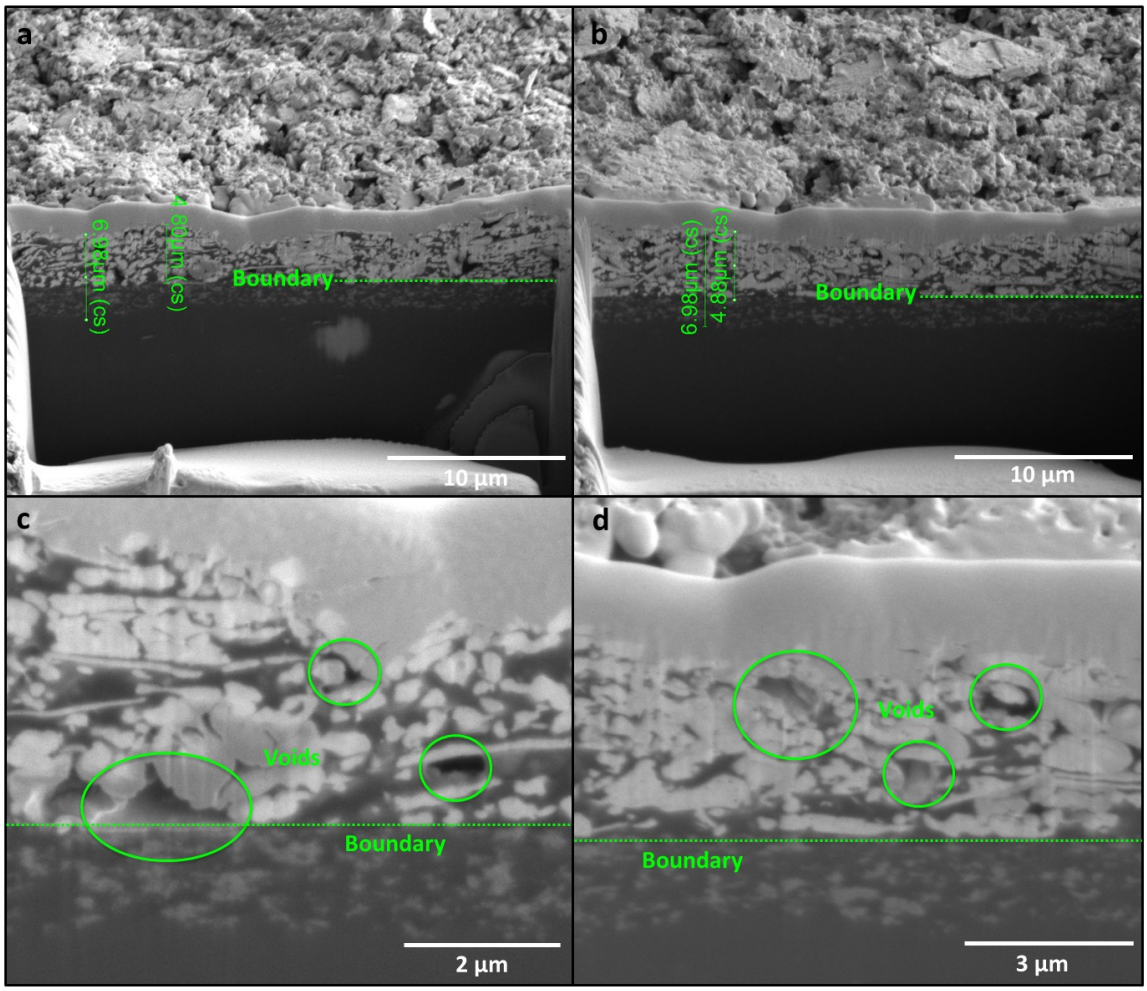

Figure 6-6: FIB cross-sections of 2mm PE 874 on TE11C, printed in 2020 (a) Uncalendered sample (b) Calendered sample (c) High mag. image of uncalendered sample, showing voids and boundary for "shaded" flake field (d) High mag. image of calendered sample, showing voids and boundary for "shaded" flake field

High magnification imaging allows for the identification of voids, found within both uncalendered and calendered samples, within the respective cross-sections. Print thicknesses are relatively equal, at about 7 µm. Just under 5 µm beneath the surface of each

print, the flake field becomes “shadowed”. These section views were compared to cross-sections of an uncalendered print from the 2018 set, which can be seen in Figure 6-7.

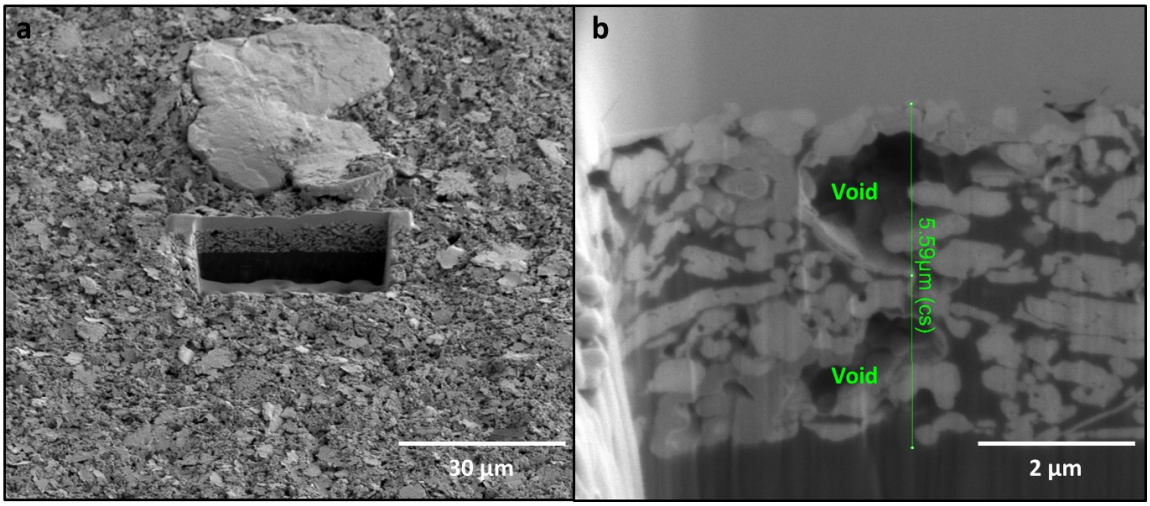

Figure 6-7: FIB cross-section of 2mm PE 874 on TE11C, printed in 2018 (a) Entire section view (b) High mag. partial section view, articulating local print thickness and presence of voids

The 2018 print section cut also presented voids, just as the calendered and uncalendered specimens from the 2020 prints. However, the incumbent specimen did not exhibit the same boundary line in section, beneath which the flake field appeared shaded. Therefore the shading phenomenon is considered to be an artifact of the later printing process, and not of the SEM imaging equipment.

Similar cross section cuts were made in each of the calendered samples, representative of each calendering direction, and analyzed for void and flake area fraction. A compilation of all such section analysis is displayed in Table 6-5. Several of these sections were taken from among the non-conducting 0.1mm print samples, which were otherwise not useable for electrical experimentation. As such they do not have measured resistance values.

Table 6-5: Compilation of area fraction analyses for PE 874 FIB cross-sections

Print Width [mm]	Substrate	Print Year	Calendered? [Y/N, Dir.]	Void Fraction [%]	Flake Fraction [%]	R_0 [Ω]	Section Width [µm]	Section Avg. Height [µm]
2	PET	2018	No	17	55	4.1	31	11.8
2	TPU	2020	No	8	55	5.9	13.6	4.5
2	TPU	2020	Yes, Down	8	58	8.6	30.3	4.4
0.1*	TPU	2018	No	9	54	N/A	27.1	3.2
0.1	TPU	2020	Yes, Up	9	53	N/A	26.6	6
0.1	TPU	2020	Yes, Up + Down	4	55	N/A	30.6	4.4
0.1	TPU	2020	Yes, Down	6	56	N/A	31.3	5.5
0.1	TPU	2020	Yes, Down + Up	5	57	N/A	31.7	6.3

*Section taken from edge of print line; captures tapered thickness

6.2.2 In-House Print and Cure

As described in 2.8, a small subset of printed samples were produced at Georgia Tech for the purpose of modifying the curing processes in an effort to eliminate voids. Given the notions that a porous architecture could be a result of either high ink viscosity, or high flake density with unfavourable packing, two methods were added to the standard curing process. The first, was to introduce the wet prints to a vacuum environment, such that the pressure differential might coax trapped air to break surface tension of the ink and escape. The second approach was to sonicate the wet prints prior to cure, with the notion that the vibrations might unlock flake structures and facilitate tighter packing. This led to four unique sample categories:

1. Hand Print, Standard Cure
2. Hand Print, Vacuum Cure
3. Hand Print, 1hr Vac. @ Room Temp, Vac. Cure
4. Hand Print, Sonicate, 2hr Vac. @ Room Temp, Sonicate, 2hr Vac, Vac. Cure

After curing, the samples were *in situ* tested per 2.2, the results of which are visible in Figure 6-8.

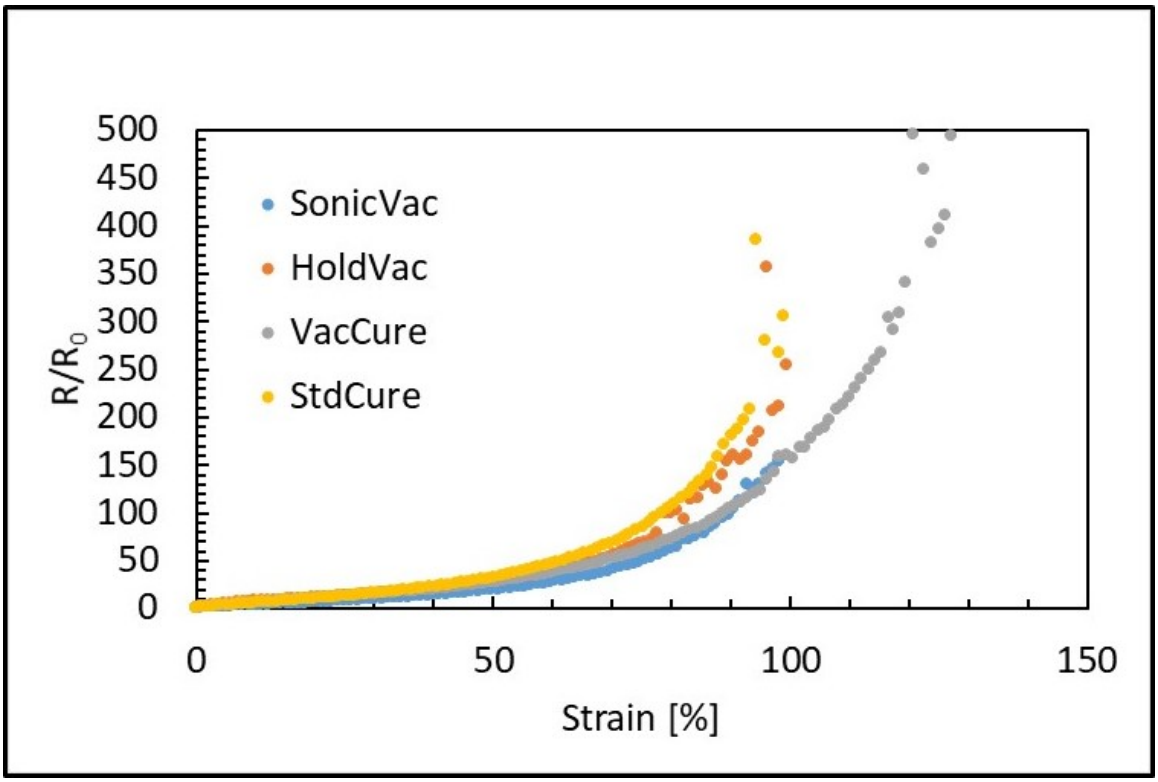

Figure 6-8: Normalized resistance vs. strain of 2mm PE 874 hand prints on polyurethane substrate, with different curing parameters

Resistance curves are very similar for $0\% \leq \varepsilon_{app} \leq 50\%$, after which they generally begin to become unstable and fail.

A sample from each printing method was also section cut to determine print thickness, and confirm whether voids were still present within the dry ink architecture. A summary of these sections may be seen in Figure 6-9. For all cure process cases, voids were found within the sample cross-sections. Additionally, measured print thicknesses were below that predicted by the manufacturer, given the parameters of the screen used. Thickness values,

along with resistance measurements in the unstrained condition, are summarized for each curing process in Table 6-5.

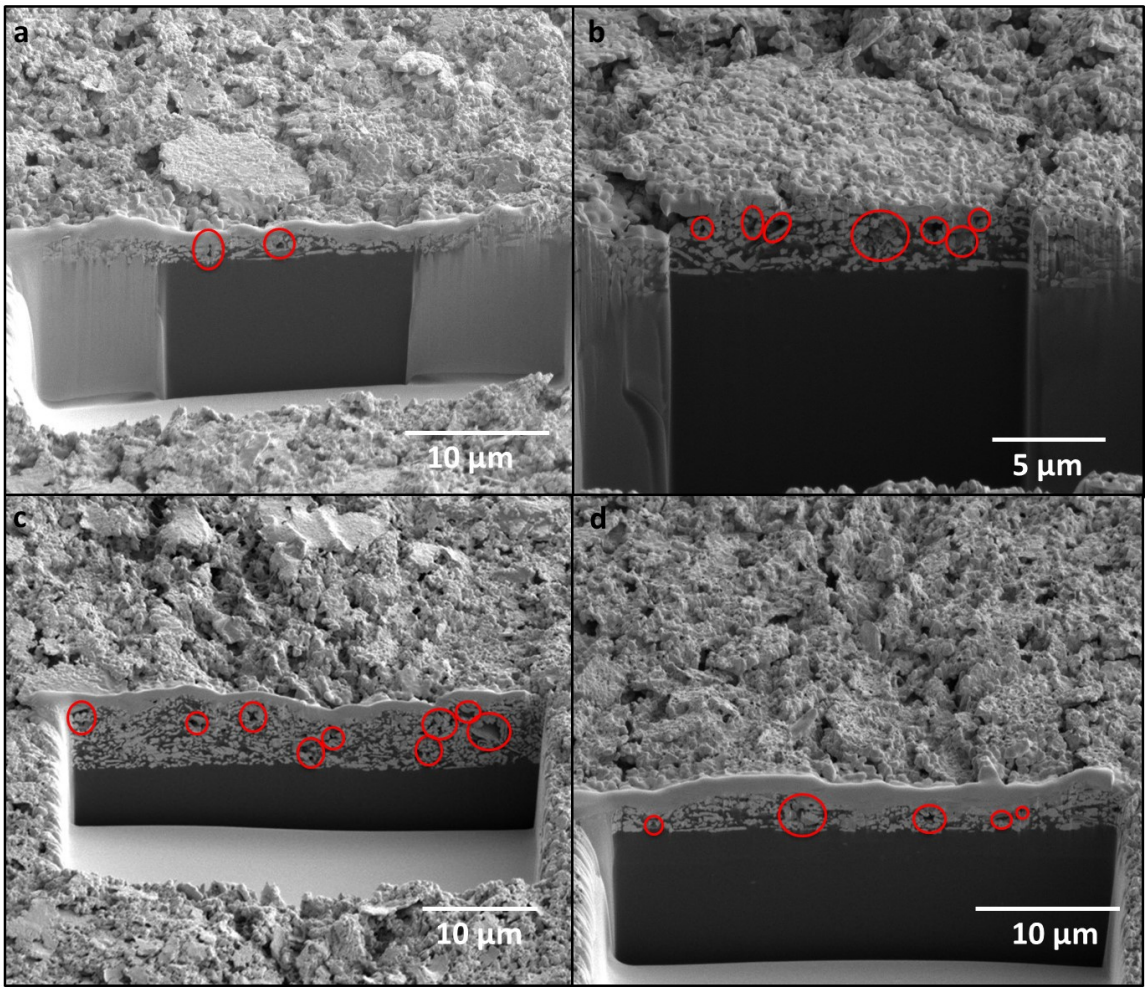

Figure 6-9: FIB cross-section SEM image showing voids (circled in red) within 2mm PE 874 on polyurethane substrate (a) Standard cure (b)Vacuum cure (c) room temp. vacuum followed by vacuum cure (d) Alternating sonication and room temperature vacuum, followed by vacuum cure

Table 6-6: Measurement summary of 2mm PE 874 on polyurethane substrate for various curing processes

Curing Process	R_0 [Ω]	Instability [% Strain]	Open Circuit [% Strain]	Section Thickness [μm]	Voids? [Y/N]
Std Cure	5.6	94.3	119.5	1.32-2.59	Yes
Vac Cure	4.4	121.6	149.1	3.36-4.66	Yes
Hold Vac	7.7	96.0	107.8	5.46-8.38	Yes
Sonic Vac	6.1	N/A	99.2	1.27-3.96	Yes

6.3 Discussion

DuPont reported the production of our test samples using a screen with 0.0016" (40.64 μm) diameter threads, at a count of 200 threads per inch. The emulsion thickness and thread material are unknown, but assuming a common emulsion thickness e = 0.0001" (2.54 μm), and stainless steel threads with rigidity coefficient a = 2.5, we can use Equation C.2 from pillar theory, and the unit conversion of 25400 μm per inch, to predict a wet deposition thickness of:

$$t_{wet} = \left(\frac{25400}{200} - 40.64\right)^2 \left((2.5 \times 40.64) + 2.54\right)\left(\frac{200}{25400}\right)^2 = 48.2\ \mu m$$

Organic solvents credited with providing fluid properties most compatible with printing are baked out during the curing phase. These solvents commonly account for 50-60% of the volume of an ink, though this does not fully explain the deficit between theoretical wet thickness and a nominal 8-10 μm dry print provided by DuPont. They cite print speed, squeegee pressure, and viscosity of the ink as relevant parameters of final print. We must also consider that this model idealizes zero loss of thickness due to pillar collapse during coalescence into a uniform film. Also note that the entirety of the filled mesh apertures are assumed to have been deposited onto the substrate, a notion that is debated by the free surface liquid transfer model.

Per the liquid transfer model, the theoretical maximum wet print thickness (ref. Equation C.9) would be:

$$H_{max} = 2 \times \frac{40.64}{2} \times \left(2 - \pi \times \frac{40.64}{2} \times \frac{200}{25400} \sqrt{1 + \left(\frac{40.64}{2} \times \frac{200}{25400} \right)^2} \right) = 60.59\ \mu m$$

Since the capillary number, Ca_{men}, and associated constant coefficients are unknown, we cannot use the general liquid model equations to calculate the scaling factor on this maximum and predict the actual deposition thickness, H_{act}. However, taking the liberty of assuming wet PE 874 has a high capillary number, we rely on Equation C.10 and Figure C-7 to approximate this scaling factor. With a unit conversion of 2.54 cm per inch, the fractional open area is calculated to be:

$$F_{open} = 1 - \frac{200}{2.54} \times 40.64 \times 10^{-4} = 0.68$$

The empirical fit curve predicts an ink transfer proportion of approximately 71%, or 43.0 μm. This is not that different from the value predicted by the pillar theory, though arguably the liquid transfer model can be further refined by the use of actual ink properties. Incomplete flooding of mesh apertures, the orientation of the screen with respect to squeegee direction of travel, and the spacing between the screen and substrate are likely to be relevant factors as well.

When considering multiple deposition steps within a print it is clear there are consistency issues, particularly in the third step. Any of the previously mentioned parameters could affect transfer of additional ink onto the substrate. Furthermore, we know that with successive prints we are no longer transferring ink to the substrate directly, but rather on top of another layer of ink. It is important to note that these samples were not

cured in between individual deposition steps, so deposited material is expected to coalesce with any prior ink layers. That having been said, free surface adhesion may differ for ink-substrate vs. ink-ink, influencing how much ink ultimately gets drawn through the screen.

The in-house prints were performed using a different screen, as described in 2.8. Under those parameters, idealized print thickness from pillar theory would be:

$$t_{wet} = \left(\frac{25400}{325} - 22.86\right)^2 \left((2.5 \times 22.86) + 12.7\right)\left(\frac{200}{25400}\right)^2 = 34.9\ \mu m$$

Free surface liquid transfer theory predicts max deposition and fractional open area of:

$$H_{max} = 2 \times \frac{22.86}{2} \times \left(2 - \pi \times \frac{22.86}{2} \times \frac{325}{25400}\sqrt{1 + \left(\frac{22.86}{2} \times \frac{325}{25400}\right)^2}\right) = 35.1\ \mu m$$

and

$$F_{open} = 1 - \frac{325}{2.54} \times 22.86 \times 10^{-4} = 0.71$$

This approximates to a transfer ratio of 71%, for a theoretical thickness of 24.9 μm. The models are going to be sensitive to the parameters of mesh density and thread diameter, but the disparity between the predicted thickness values and the average actual values of 2.9 – 5.2 μm measured from FIB cross-sections must be attributed to process parameters not captured by either one. This includes squeegee blade rigidity, pressure and speed, as well as the amount of ink used to flood the screen.

Results from the calendering investigations indicate that calendering does not significantly affect electrical performance, be it initial measured resistance, or thresholds for failure or instability. Since the calendering took place after the new prints were cured,

we can presume the effect was to elastically depress the ink material. Once compression was removed, the ink likely rebounded with no permanent change to its architecture. Of greater note is the disparity in performance between the older prints and the newer ones. One would expect larger agreement between samples produced with the same materials, and by the same processes (excluding calendering). One explanation could be relative differences in batch material properties. Favorable orientation of silver flakes for more uniform strain distribution in the 2018 prints seems unlikely. There may have been formulation differences, or environmental factors that influenced the newer prints to have lower elasticity, or weaker internal flake-matrix adhesion, which might accelerate strain-induced surface ruptures.

Considering the samples produced at Georgia Tech, each print performed up to approximately $\varepsilon_{app} = 100\%$ before reaching a compromised measurement threshold, despite thickness reductions on the order of 50%-90%. Given the high width to thickness aspect ratio of the w = 2mm design, this suggests a stronger relationship between performance and width, than with thickness. Voids were also found in each sample, regardless of cross-section thickness. Under the presumed correlation between surface rupture and void location, it is possible that voids serve to create locations of stress concentration and the nucleation points for surface ruptures. However, void breadth into the material (in the direction across the print line) may be shallow, requiring rupture channels to grow and link with others to fully sever the conducting cross-section, which scales with width.

6.4 Conclusions

This chapter explored process parameters associated with screen printing PE 874 ink onto TE11C substrate. Voids manifest within the ink architecture, even at reduced print

thicknesses. Sonication and vacuum cure operations are ineffective at eliminating them. To do so will require modifications to the ink formulation itself. Nevertheless, a print of 20% nominal thickness showed electrical instability and open circuit threshold performance comparable to samples produced using DuPont's controlled processes. This indicates thickness is less relevant than width, or perhaps void presence.

Multi-step deposition proved unreliable in producing predictable print thicknesses, even among large features such as $w = 2.0$ mm for which no positive addition to thickness could be attributed to the third deposition run. That having been said, the steeper taper regions because of repeated deposition increases the cross-sectional area of the print lines, which may be beneficial to electrical performance. *In situ* monotonic testing would reveal how the relative instability and open circuit strain thresholds have been affected by the change in cross-section.

While theoretical models exist to predict deposition thickness – and sometimes they even agree – they do not fully capture all of the relevant parameters associated with the screen printing process. Such parameters are tuned to create the proprietary processes that allow manufacturers like DuPont to enjoy high reliability of their prints.

CHAPTER 7. CONCLUSIONS AND FUTURE WORK

7.1 Conclusions

5025 and PE 874 inks were expected to conform to percolation theory, differing only by their relative polymer matrix properties that dictate Poisson effects due to elongation. On the contrary, Chapter 3 highlighted the importance of the initial architecture of silver inks on the deformation and electrical behavior. In situ strain map analysis showed the formation of strain localization bands at early applied strain levels. The origins of these bands differ, which result in different flake volume fraction evolutions and therefore different electrical behavior. FIB cross-sections revealed the significant presence of micron-size voids in the PE 874 ink. Its strain localization is associated with surface cracking, most likely triggered by these pre-existing voids. There is minimal silver flake volume fraction change with strain such that, at $\varepsilon_{app} = 35\%$, the resistance ratio increase is 5. Instead, for 5025, local necking accompanies strain localization. This engenders large silver flake volume fraction decreases and a resistance ratio increase of 15 at $\varepsilon_{app} = 35\%$. A Gaussian distribution (which captures non-uniform deformation) of measured flake fraction incorporated into to percolation theory provides reasonable estimates of the resistance ratio increase with strain for 5025, compared to the use of average flake fraction (which better captures uniform deformation).

Pre-existing voids may lead to cracks in the deformed PE 874 ink, which can actually be beneficial for their electrical behavior under large strains. While surface cracks indicate an increase in void fraction (porosity), and therefore an increase in resistance, their formation prevents any significant decrease in flake volume fraction (especially in necked

regions). As cracks do not immediately penetrate through the thickness of the ink, their formation appears to be not as detrimental to the ink's overall electrical behavior.

Chapter 4 revealed that electrical behavior of PE 874 trends with printed trace width. Narrower prints reach are more sensitive to ε_{app}, reaching instability and circuit failure sooner, because surface rupture growth and networking severs a higher proportion of conducting cross sectional area.

Stronger deposition control of thickness at small feature size may enhance reliability of the material, such that damage channels are required to more fully deepen to sever the conductive line.

Chapter 5 examined the behavioral response of PE 874 conductive ink when subjected to high strain cycling. Initial elongation to ε_{max} generates surface cracks, which form a networked channel damage pattern. Despite the presence of such defects, the hybrid conductive ink traces continue to remain electrically conductive for multiple cycles. As cracks deepen with each cycle, they approach the full thickness of the ink, leading to electrical circuit failure. Crack deepening is affected by strain amplitude. At low enough strain amplitudes, the mean strain also impacts the ink performance.

Chapter 6 provided insight into the complex variables at play when producing reliable print geometries. Edge thickness taper can be attenuated with multiple print steps, though existing models do not fully capture the mechanisms that drive fluid deposition through a screen. Despite attempts to modify the PE 874 printing process pre and post cure, porosity proved difficult to eliminate. The architecture of the ink is locked until modifications are made to its formulation, prior to printing. Pre-existing voids, such as they are, may still be beneficial in how surface cracks attenuate flake volume reduction with

strain. Furthermore, their negative effects can be overcome by increasing the width of the printed line.

7.2 Recommendations for Future Work

The findings in this work revealed many insights into electrical failure behavior of screen printed polymer supported inks subjected to uniaxial strain. However, the understanding and details of these findings can be further expanded by performing additional in-depth investigations. The following are recommendations for future research avenues:

- Applied uniaxial strain was found to localize almost immediately following the onset of elongation, manifesting as either surface cracks or extreme necking in PE 874 and 5025, respectively. However, the origin of localization has yet to be attributed to any particular property of the ink. High surface roughness could concentrate stresses, leading to “weak points” in the ink surface. Relatively dense concentrations of filler material could create non-deforming regions, leaving low density volumes to elongate more rapidly. These parameters can be simulated to offer insights into ways of attenuating strain localization and surface tears.
- Many applications of flexible electronics require biaxial, or triaxial, stretching. Such scenarios are not explored in this dissertation, however the experimental and analytical procedures described can be modified to incorporate test fixtures with greater degrees of freedom. Such investigation into broader strain parameters would provide a more comprehensive understanding of ink behavior as it relates to

mechanical response to elongation in multiple directions, and subsequent evolution of electrical performance.

- Future work will need to explore more closely the driving mechanism behind the deepening of the cracks in PE 874, and similar composite materials which exhibit such behavior. Polymer matrix failure due to fatigue, delamination between flakes and the matrix, or a combination of the two, are likely at play. Incorporation of *in situ* SEM into the experimental process would aid in this study.
- Investigating PE 874 inks with different initial void contents (presumably by optimizing the fabrication process) would be useful to further understand the combined effect of voids and strain localization on electrical behavior under large strains. Adjustments to ink formulation, such as reduced filler loading, using smaller average particles, using filler particles with lower aspect ratios, may help to eliminate voids entirely. Subsequent experimentation would reveal the specific role voids play – as more of a hindrance, or an advantage – in the ultimate failure of these inks.

APPENDIX A. ADDITIONAL STRAIN FIELDS

This appendix provides additional in-plane surface strain fields for each combination of 5025 and PE 874 ink supported by either Kapton PI, PET, or one the TPU formulations: TE11C and ST604. Strain fields were derived from optical images captured by the LEXT confocal microscope, and subsequently generated using Ncorr.

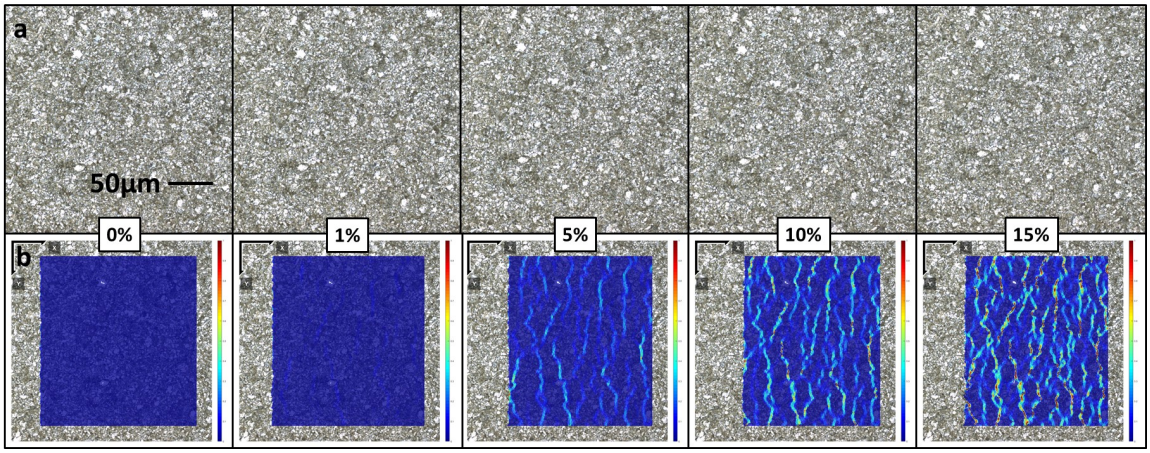

Figure A-1: Optical imaging and strain field calculations for 5025 on Kapton PI under applied uniaxial far field strain values of 0%, 1%, 5%, 10%, and 15%. (a) 5025 “flexible” ink optical surface images (b) 5025 strain field overlay

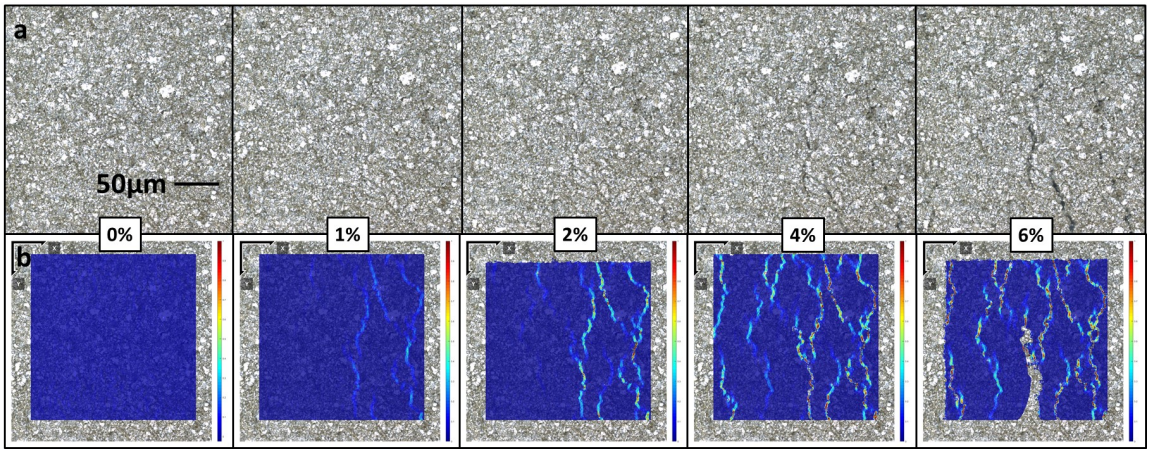

Figure A-2: Optical imaging and strain field calculations for 5025 on ST604 under applied uniaxial far field strain values of 0%, 1%, 2%, 4%, and 6%. (a) 5025 “flexible” ink optical surface images (b) 5025 strain field overlay

Strain localization in 5025 was not as evenly distributed as with PET and PI support. Strain magnitudes were extremely high for localization bands on the softer substrate. This resulted in deep cracking within the ink. The sample failed by $\varepsilon_{app} = 6\%$.

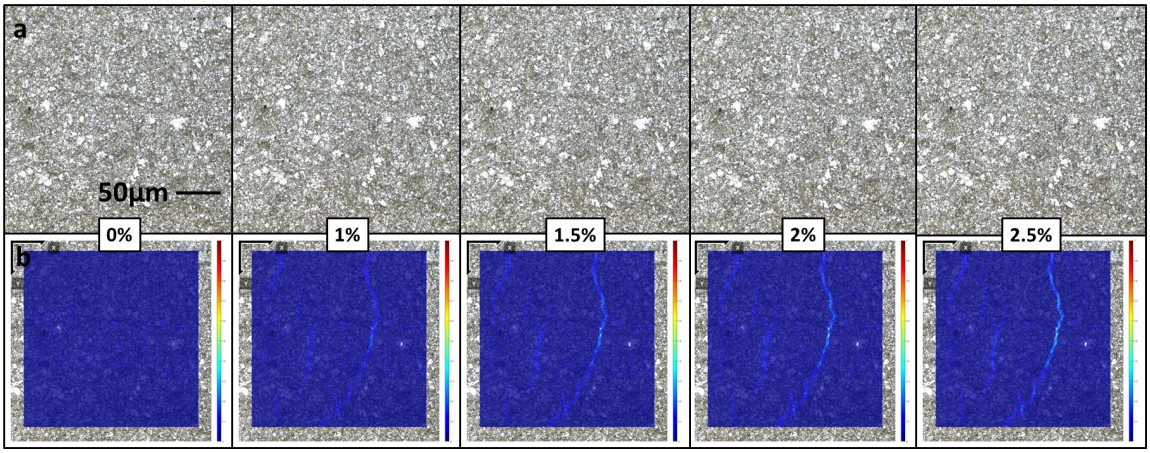

Figure A-3: Optical imaging and strain field calculations for 5025 on TE11C under applied uniaxial far field strain values of 0%, 1%, 2%, 4%, and 6%. (a) 5025 “flexible” ink optical surface images (b) 5025 strain field overlay

As with 5025 on ST604, localization in this ink is not widespread as with stronger substrates. Electrical failure in this sample occurred by ε_{app} = 2.5%. Since catastrophic damage was not apparent within the selected view window, additional investigation of the ink at failure strain was conducted, leading to the discovery of significant large crack formations elsewhere.

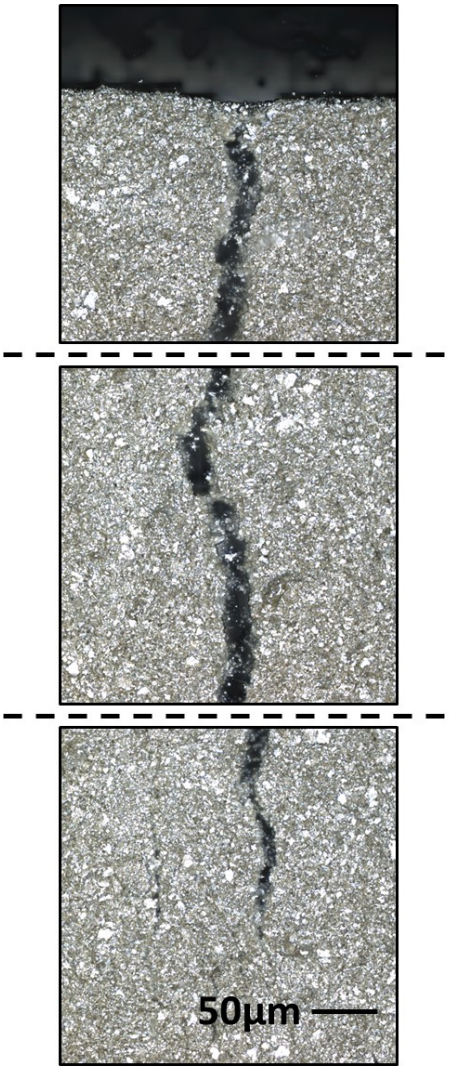

Figure A-4: Example of mechanical failure of 5025 printed onto TE 11C.

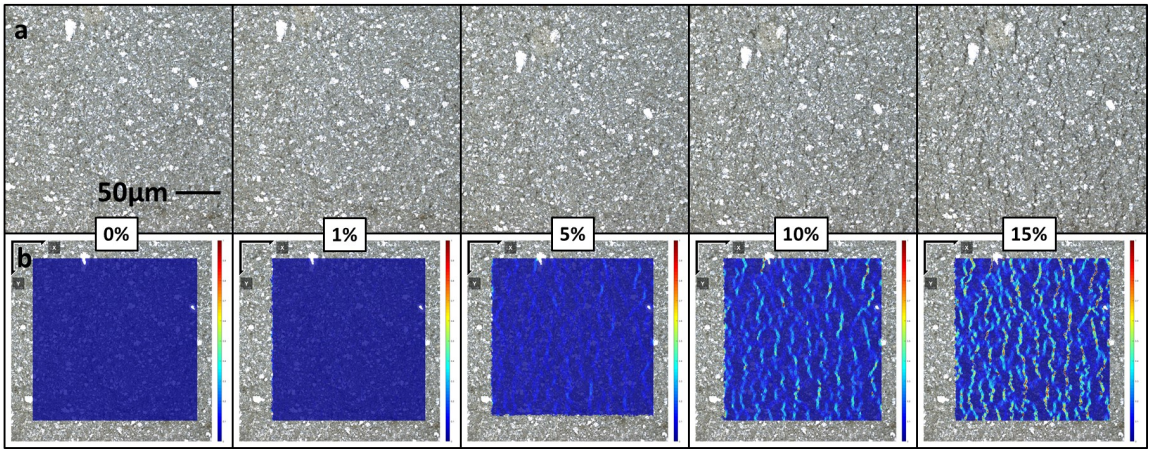

Figure A-5: Optical imaging and strain field calculations for PE 874 on Kapton PI under applied uniaxial far field strain values of 0%, 1%, 5%, 10%, and 15%. (a) PE 874 "stretchable" ink optical surface images (b) PE 874 strain field overlay

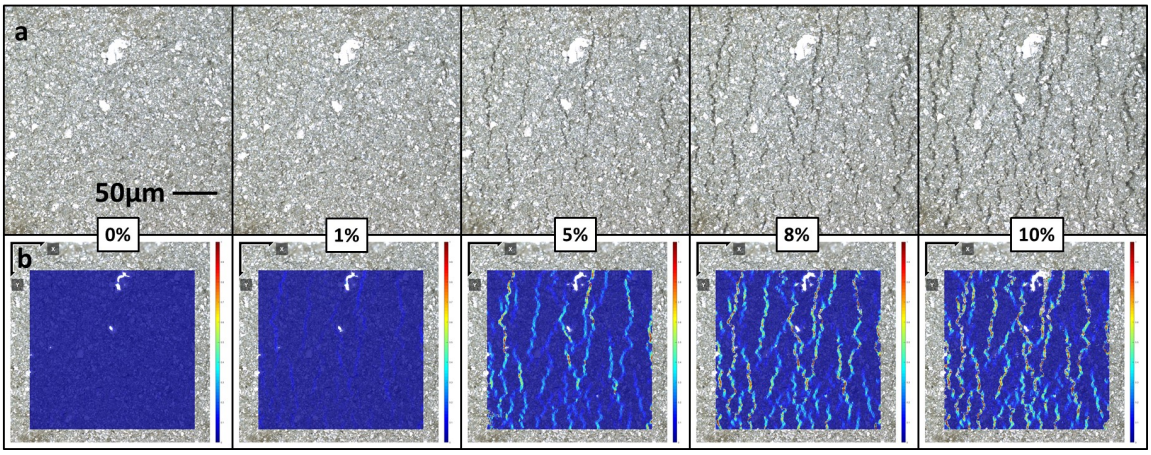

Figure A-6: Optical imaging and strain field calculations for PE 874 on TE11C under applied uniaxial far field strain values of 0%, 1%, 5%, 8%, and 10%. (a) PE 874 "stretchable" ink optical surface images (b) PE 874 strain field overlay

APPENDIX B. FAILED PRINT DEFECTS

As described in 4.2, this appendix provides examples of print defects that resulted in open circuits in the unstrained condition among w = 0.1mm prints of PE 874 on TE11C.

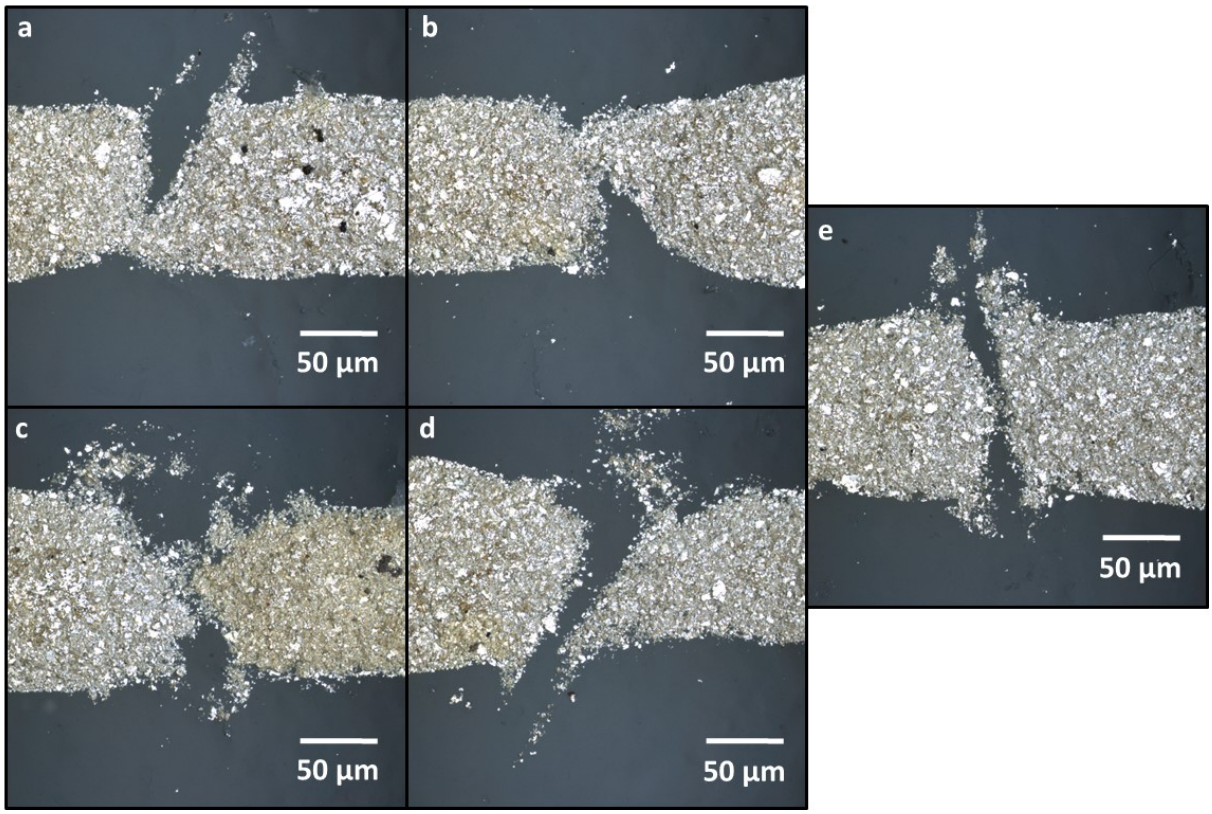

Figure B-1: Print line defects found in w = 0.1mm PE 874 on TE11C (a-b) Partial line width severed (c-e) Total conductive line width severed

APPENDIX C. SCREEN PRINTING THEORIES TO CALCULATE WET DEPOSITION THICKNESS

Screen printing has been adopted for the production of electronics, and as such requires theories to reasonably predict electrical performance via deposition thickness. This section briefly summarizes two such models: simple pillar theory [63], and free surface liquid transfer [92]. Pillar theory operates under the notion that ink is forced through the mesh screen by the squeegee. Liquid transfer theory suggests that squeegee force is not relevant, and instead ink is drawn through the mesh via contact with the substrate due to surface tension.

When considering the mesh screen, fibers having diameter, d, are uniformly inter-woven in a grid at a mesh count of T. Thickness of the mesh may be quantified by the term ad, whereby a constitutes a coefficient dependent upon the rigidity of the material used for the threads, as well as weaving tension, typically falling within the range $2 < a < 3$. A conceptual cross-section may be seen in Figure C-1.

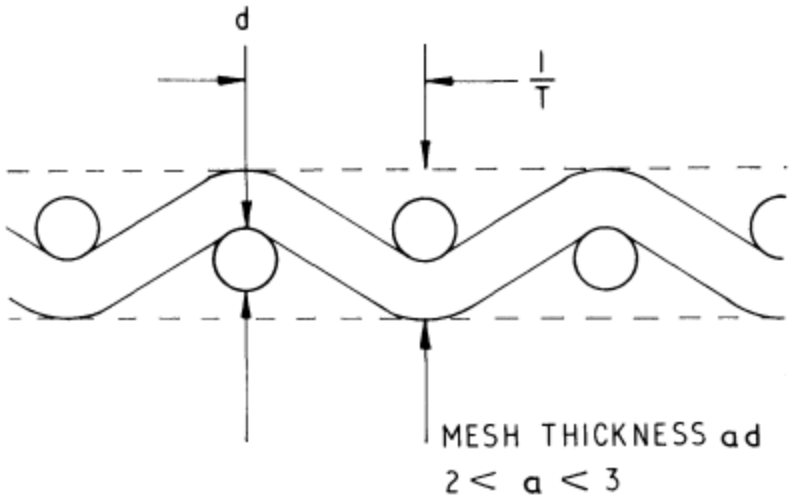

Figure C-1: Section of mesh [63]

To create the desired print pattern, the screen is saturated with an emulsion material, masked, and then photo-cured. Uncured material is then removed, clearing the appropriate apertures in the mesh grid for ink deposition. When initially printed, the ink passes through the screen as pillars, having cross-section dimensions equal to the aperture size, and height equal to the combined thickness of mesh and emulsion, *e*, such that each pillar has volume:

$$\left(\frac{1}{T} - d\right)^2 (ad + e) \qquad \text{Equation C.1 [63]}$$

Given T^2 pillars in a unit square, total ink volume, *v*, per unit area is:

$$v = \left(\frac{1}{T} - d\right)^2 (ad + e)T^2 \qquad \text{Equation C.2 [63]}$$

This is conceptualized in Figure C-2:

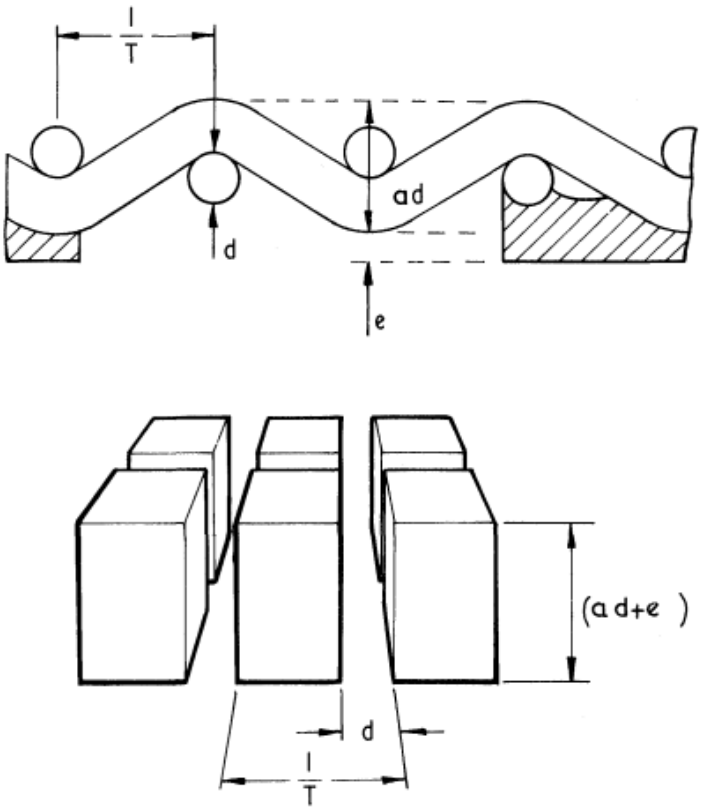

Figure C-2: Mesh cross-section with emulsion mask thickness, and subsequent deposited ink pillars [63]

Once deposited, ink pillars collapse via lateral flow, and coalesce into a continuous film. Given small enough pillar spacing, merging occurs with negligible reduction in thickness, so the wet thickness is ideally taken as equal to the pillar volume per unit area. When cured, the dry ink thickness decreases from wet thickness by some percentage based on the amount of volatile vehicle added to achieve desired ink flow characteristics, which evaporates out.

During printing, a mesh, *M*, is positioned a distance, *D*, from the substrate stage. Ink is supplied to the mesh, and a downward force, *F*, is applied to the squeegee blade, depressing the screen to a level, *L*, and placing it under tension. As the blade is moved

laterally at a velocity, *V*, it reaches the substrate stage and places the screen in contact, receiving a reaction force, *R*, from the substrate, which is dependent upon *F* and *V* and deforms the blade tip at an angle, θ. This may be seen in Figure C-3(i-iii). The level to which the blade and screen are depressed may be controlled by a stop, S, as illustrated by Figure C-3(iii) and (iv).

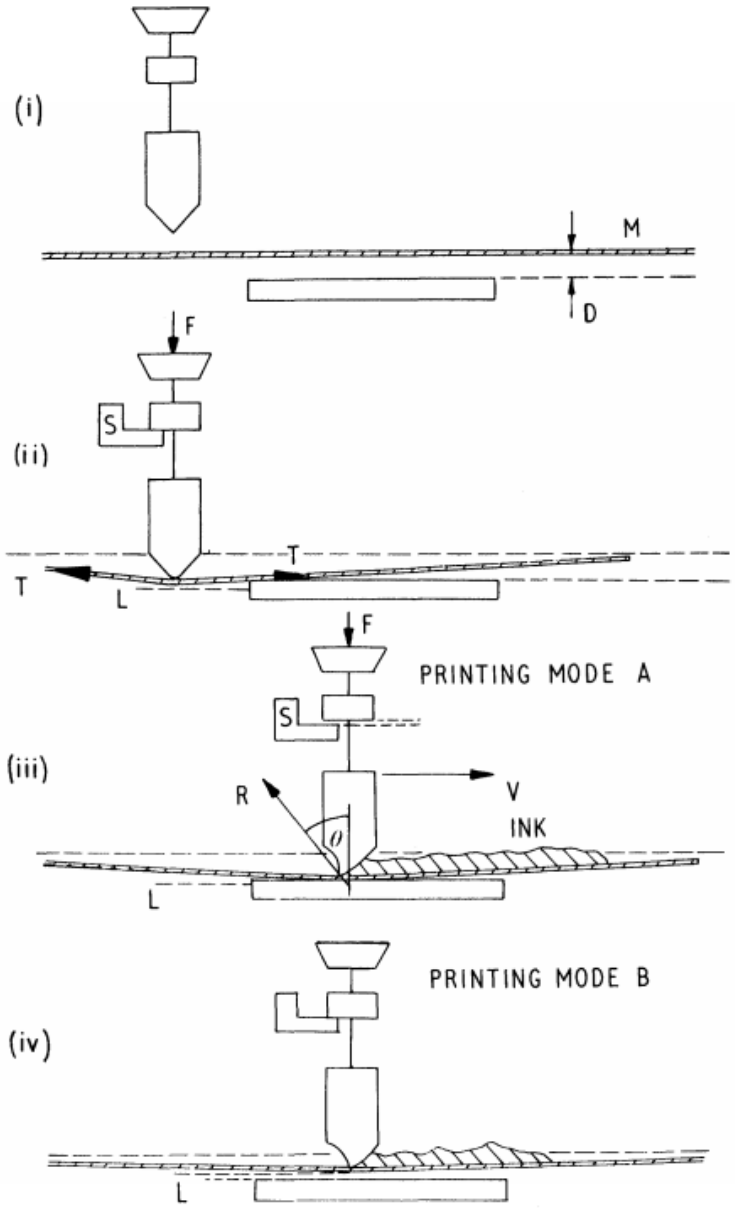

Figure C-3: The screen printing mechanism [63]

In this manner, print thickness may be adjusted by either variation of squeegee travel speed, V, the level, L, as determined by stop, S, or some combination of the two. These parameters, along with squeegee material hardness, affect the level of deformation of the blade tip. The greater the deformation, the more the tip is lifted off of the substrate, and the more ink is presumably forced through the screen as opposed to pushed forward in front of the blade. For example, a higher travel speed and a softer blade trend toward higher tip deformation, and higher print thickness. Other factors influencing squeegee blade deflection include pre-tension of the screen, orientation of the screen with respect to squeegee travel, rheological properties of the ink, and even stencil positioning on the screen as it relates to alignment with apertures in the mesh. Over time, wear of the blade tip also becomes relevant, and is often addressed by increasing force, F, to maintain print thickness.

An alternative approach to predicting print thickness comes from looking at the surface tension of the liquid ink itself [92]. Considering transfer of the ink from the mesh screen to the substrate does not occur until after the squeegee blade passes by, one can see how surface tension affects the infiltration of free surface through a screen. Ink deposition for traditional off-contact printing (see Figure C-3iii), therefore, is described in three stages, as described by Figure C-4:

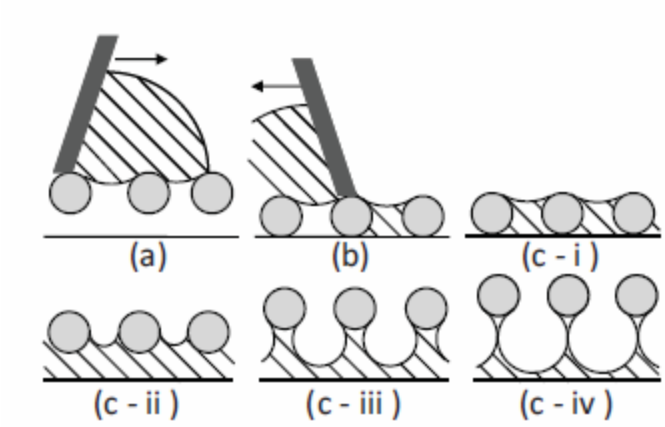

Figure C-4: Schematic showing the three stages of screen printing (a) Excess of fluid on mesh after flood stroke (b) Squeegee forces screen into contact with substrate and fills cavities with ink (c) (i-iv) Screen separates from substrate and ink is pulled from mesh [92]

As the squeegee plays no role in the final stage of printing – when the tensioned mesh retreats from contact with the substrate – previously considered parameters such as squeegee force and passing speed are not relevant. The important calculation comes from describing the behavior of the liquid bridge structures that form between the screen and substrate, and their meniscus boundaries. This is used to determine the amount of material left on the screen in residual after print.

Given a screen with cylindrical threads of radius R_{thread}, uniformly separated by a distance of $2H_0$, and oriented parallel to the squeegee blade and perpendicular to the direction of squeegee motion, provides a unit cell for a single aperture through which ink can flow.

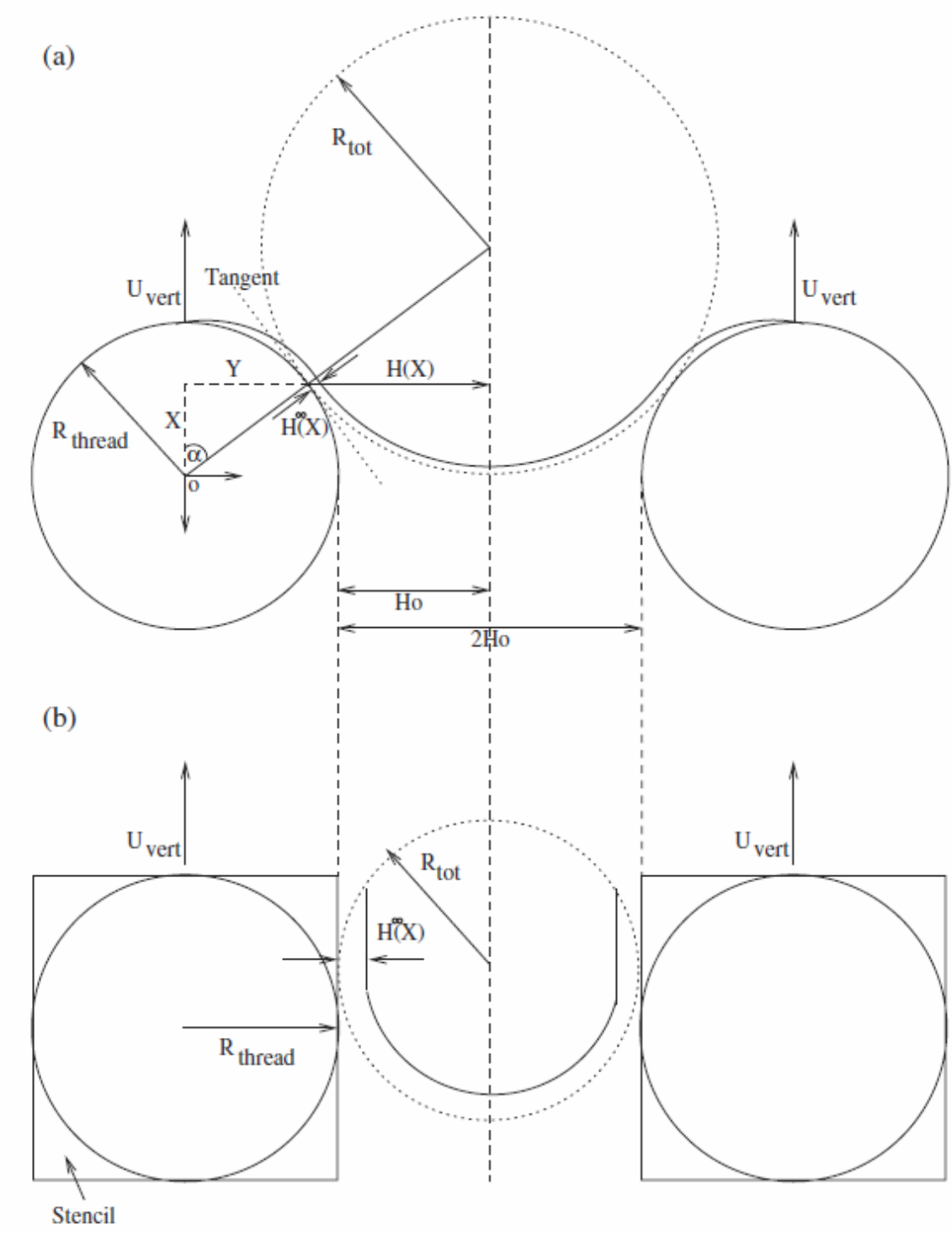

Figure C-5: Geometry of (a) 2-D mesh and (b) stenciled portion of the mesh with a single opening [92]

An idealized approach carries the following assumptions:

- The ink is incompressible, with negligible body forces, no-slip boundary conditions at the surfaces of the substrate and screen, and Reynolds number <<1, making inertial effects negligible.
- The tip of the squeegee blade is sharp and rigid, and completely fills the screen apertures, leaving a level ink surface on top.
- Screen tension only serves to keep it level between its frame and where the squeegee presses it in contact with the substrate.
- The shape of the free surface of the ink follows its radius of curvature, conforming to preserve volume. Separation occurs when free surfaces meet underneath a thread.

Using the coordinate system provided by Figure C-5, the problem is broken into two stages:

1. Calculate the free surface meniscus radius, $R_{men}(X)$, and its speed, $U_{men}(X)$, for each value of X.
2. Determine whether free surfaces have touched, indicating separation has occurred and residual ink on the mesh can be calculated.

The half-gap, H(X), for any X is:

$$H(X) = H_0 + R_{thread} - \sqrt{R_{thread}^2 - X^2} \qquad \text{Equation C.3 [92]}$$

where the minimum, H_0, is described by thread diameter, D_{thread}, and the threads per unit length, M:

$$H_0 = \frac{1}{M} - \frac{D_{thread}}{2}$$ Equation C.4 [92]

The gradient of the tangent to the thread is:

$$\frac{dY}{dX} = -\frac{X}{\sqrt{R_{thread}^2 - X^2}}$$ Equation C.5 [92]

The radius, R_{tot}, is calculated by matching its tangent to the tangent of the thread:

$$R_{tot} = H^{\infty}(X) + R_{men} = H(X)\left(1 + \left(\frac{dY}{dX}\right)^2\right)^{\frac{1}{2}}$$ Equation C.6 [92]

where $H^{\infty}(X)$ is the thickness of the film remaining on the thread. Speed of the meniscus surface boundary is then related to residual ink thickness as a function of the capillary number, Ca_{men}, given fluid viscosity, μ, and surface tension σ:

$$\frac{H^{\infty}}{R_{men}} = aCa_{men}^{b}$$ Equation C.7 [92]

Constants *a* and *b* must be evaluated analytically for the particular ink in use. Combining Eqns. 1.16 and 1.17, residual film may be expressed as:

$$H^{\infty}(X) = \frac{R_{tot} aCa_{men}^{b}}{1 + aCa_{men}^{b}}$$ Equation C.8 [92]

By integrating between the top of the thread and the point when the two menisci beneath a thread intersect, one can calculate the volume remaining on the thread. Note that this does not consider the deposition pattern of ink that actually transfers to the substrate. The

theoretical maximum printed thickness, H_{max}, given all ink transfers to the substrate is defined as:

$$H_{max} = 2R_{thread}\left(2 - \pi R_{thread} M\sqrt{1 + (2R_{thread}M)^2}\right) \qquad \text{Equation C.9 [92]}$$

Additional factors can add complications resulting in errors when calculating residual ink volume. The evolution of the meniscus is impacted by the shape of the mesh cross-section, or stencil. Square edges cause pinning of the lower meniscus, which reduces the amount of ink left on the substrate. This is illustrated in Figure C-6:

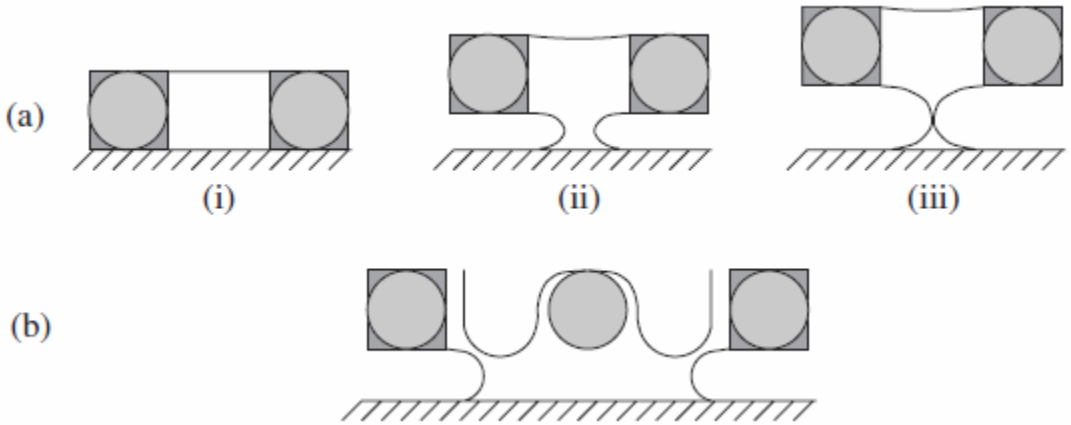

Figure C-6: Profile of the free surface when printing through a stenciled portion of the mesh with (a) single opening and (b) two openings [92]

When fluids have sufficiently high capillary numbers, their properties have negligible effect on final print thickness compared to thread count and diameter. In these cases ($Ca >$ 10), a simplified empirical model has been developed using the fractional open area of the mesh, F_{open}, which is calculated using M in threads per cm, and D_{thread} in microns:

$$F_{open} = 1 - MD_{thread} \times 10^{-4} \qquad \text{Equation C.10 [92]}$$

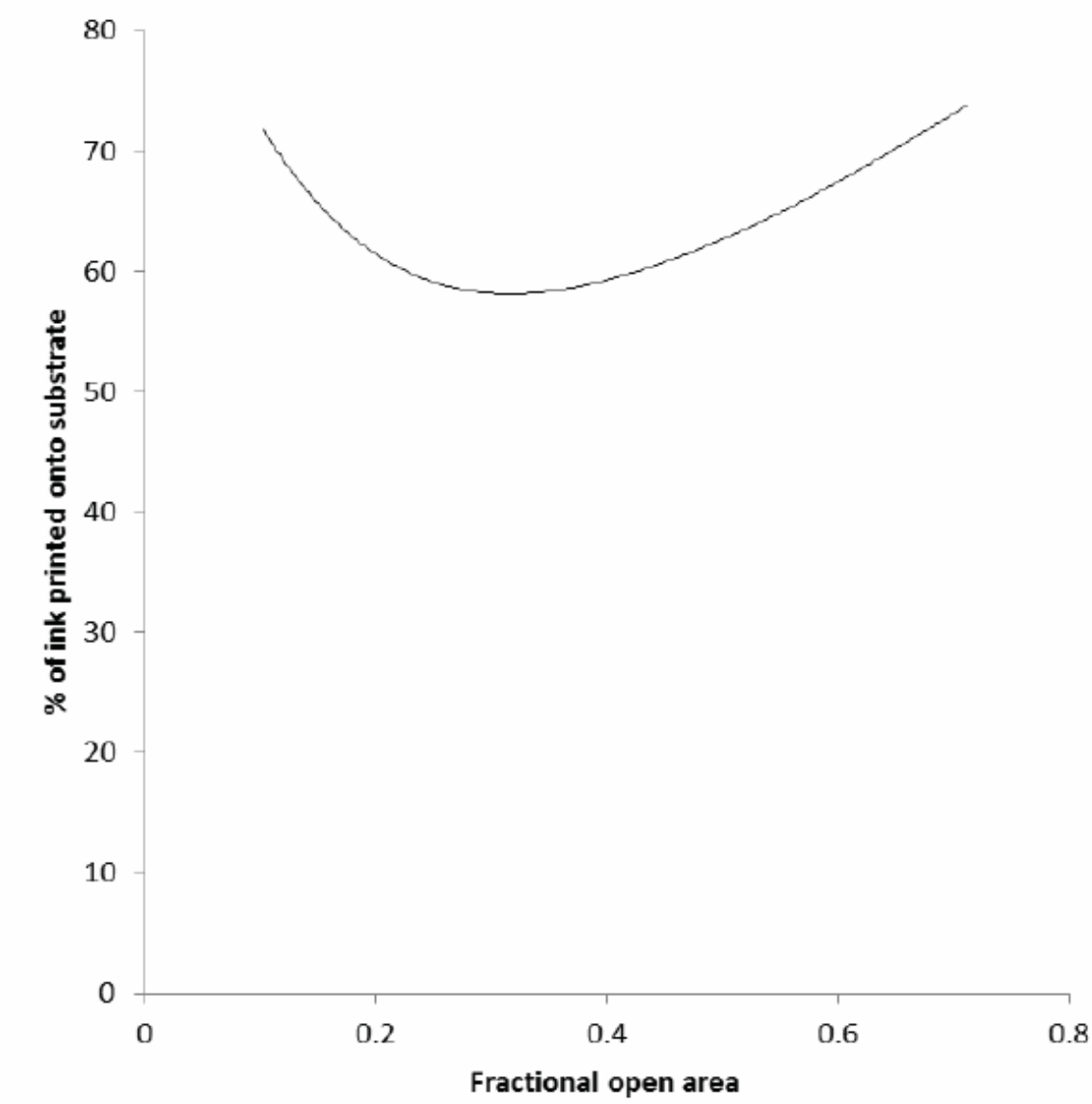

Figure C-7: Predicted transfer of fluid to the substrate at high Ca (>10) as a function of the open fraction of the mesh [92]

The percentage of ink printed onto the substrate from Figure C-7 can be applied to the theoretical maximum print thickness, H_{max}, for a reasonable approximation of actual deposition thickness.

REFERENCES

[1] Y. Liu, H. Wang, W. Zhao, M. Zhang, H. Qin, Y. Xie, Flexible, Stretchable Sensors for Wearable Health Monitoring: Sensing Mechanisms, Materials, Fabrication Strategies and Features, Sensors (Basel) 18(2) (2018) 645.

[2] D. Briand, A. Oprea, J. Courbat, N. Bârsan, Making environmental sensors on plastic foil, Materials Today 14(9) (2011) 416-423.

[3] J. Kim, A. Banks, H. Cheng, Z. Xie, S. Xu, K.-I. Jang, J.W. Lee, Z. Liu, P. Gutruf, X. Huang, P. Wei, F. Liu, K. Li, M. Dalal, R. Ghaffari, X. Feng, Y. Huang, S. Gupta, U. Paik, J.A. Rogers, Epidermal Electronics with Advanced Capabilities in Near-Field Communication, Small 11(8) (2015) 906-912.

[4] F.-R. Fan, Z.-Q. Tian, Z. Lin Wang, Flexible triboelectric generator, Nano Energy 1(2) (2012) 328-334.

[5] M.F. El-Kady, R.B. Kaner, Scalable fabrication of high-power graphene micro-supercapacitors for flexible and on-chip energy storage, Nature Communications 4 (2013) 1475.

[6] W.T. Dang, V. Vinciguerra, L. Lorenzelli, R. Dahiya, Printable stretchable interconnects, Flex Print Electron 2(1) (2017).

[7] H.-R. Lim, H.S. Kim, R. Qazi, Y.-T. Kwon, J.-W. Jeong, W.-H. Yeo, Advanced Soft Materials, Sensor Integrations, and Applications of Wearable Flexible Hybrid Electronics in Healthcare, Energy, and Environment, Adv Mater n/a(n/a) (2019) 1901924.

[8] D. McCoul, W.L. Hu, M.M. Gao, V. Mehta, Q.B. Pei, Recent Advances in Stretchable and Transparent Electronic Materials, Adv Electron Mater 2(5) (2016).

[9] A.R. Rathmell, B.J. Wiley, The Synthesis and Coating of Long, Thin Copper Nanowires to Make Flexible, Transparent Conducting Films on Plastic Substrates, Adv Mater 23(41) (2011) 4798-4803.

[10] S. De, T.M. Higgins, P.E. Lyons, E.M. Doherty, P.N. Nirmalraj, W.J. Blau, J.J. Boland, J.N. Coleman, Silver Nanowire Networks as Flexible, Transparent, Conducting Films: Extremely High DC to Optical Conductivity Ratios, Acs Nano 3(7) (2009) 1767-1774.

[11] F. Carpi, P. Chiarelli, A. Mazzoldi, D. De Rossi, Electromechanical characterisation of dielectric elastomer planar actuators: comparative evaluation of different electrode materials and different counterloads, Sensor Actuat a-Phys 107(1) (2003) 85-95.

[12] C.K. Gong, J.J. Liang, W. Hu, X.F. Niu, S.W. Ma, H.T. Hahn, Q.B. Pei, A Healable, Semitransparent Silver Nanowire-Polymer Composite Conductor, Adv Mater 25(30) (2013) 4186-4191.

[13] S. Yun, X. Niu, Z. Yu, W. Hu, P. Brochu, Q. Pei, Compliant Silver Nanowire-Polymer Composite Electrodes for Bistable Large Strain Actuation, Adv Mater 24(10) (2012) 1321-1327.

[14] T.A. Kim, H.S. Kim, S.S. Lee, M. Park, Single-walled carbon nanotube/silicone rubber composites for compliant electrodes, Carbon 50(2) (2012) 444-449.

[15] M. Vosgueritchian, D.J. Lipomi, Z.A. Bao, Highly Conductive and Transparent PEDOT:PSS Films with a Fluorosurfactant for Stretchable and Flexible Transparent Electrodes, Adv Funct Mater 22(2) (2012) 421-428.

[16] Y.H. Kim, C. Sachse, M.L. Machala, C. May, L. Muller-Meskamp, K. Leo, Highly Conductive PEDOT:PSS Electrode with Optimized Solvent and Thermal Post-Treatment for ITO-Free Organic Solar Cells, Adv Funct Mater 21(6) (2011) 1076-1081.

[17] T.S. Hansen, K. West, O. Hassager, N.B. Larsen, Highly stretchable and conductive polymer material made from poly (3,4-ethylenedioxythiophene) and polyurethane elastomers, Adv Funct Mater 17(16) (2007) 3069-3073.

[18] H. Boys, G. Frediani, S. Poslad, J. Busfield, F. Carpi, A dielectric elastomer actuator-based tactile display for multiple fingertip interaction with virtual soft bodies, Electroactive Polymer Actuators and Devices (Eapad) 2017 10163 (2017).

[19] M. Matysek, P. Lotz, T. Winterstein, H.F. Schlaak, Dielectric Elastomer Actuators for Tactile Displays, World Haptics 2009: Third Joint Eurohaptics Conference and Symposium on Haptic Interfaces for Virtual Environment and Teleoperator Systems, Proceedings (2009) 290-295.

[20] W. Yuan, T.L. Lam, J. Biggs, L.B. Hu, Z.B. Yu, S.M. Ha, D.J. Xi, M.K. Senesky, G. Gruner, Q.B. Pei, New electrode materials for dielectric elastomer actuators, Electroactive Polymer Actuators and Devices (Eapad) 2007 6524 (2007).

[21] A.P. Robinson, I. Minev, I.M. Graz, S.P. Lacour, Microstructured Silicone Substrate for Printable and Stretchable Metallic Films, Langmuir 27(8) (2011) 4279-4284.

[22] J. Jones, S.P. Lacour, S. Wagner, Z.G. Suo, Stretchable wavy metal interconnects, J Vac Sci Technol A 22(4) (2004) 1723-1725.

[23] X.L. Wang, H. Hu, Y.D. Shen, X.C. Zhou, Z.J. Zheng, Stretchable Conductors with Ultrahigh Tensile Strain and Stable Metallic Conductance Enabled by Prestrained Polyelectrolyte Nanoplatforms, Adv Mater 23(27) (2011) 3090-+.

[24] J.J. Liang, L. Li, K. Tong, Z. Ren, W. Hu, X.F. Niu, Y.S. Chen, Q.B. Pei, Silver Nanowire Percolation Network Soldered with Graphene Oxide at Room Temperature and

Its Application for Fully Stretchable Polymer Light-Emitting Diodes, Acs Nano 8(2) (2014) 1590-1600.

[25] P. Lee, J. Ham, J. Lee, S. Hong, S. Han, Y.D. Suh, S.E. Lee, J. Yeo, S.S. Lee, D. Lee, S.H. Ko, Highly Stretchable or Transparent Conductor Fabrication by a Hierarchical Multiscale Hybrid Nanocomposite, Adv Funct Mater 24(36) (2014) 5671-5678.

[26] K.Y. Chun, Y. Oh, J. Rho, J.H. Ahn, Y.J. Kim, H.R. Choi, S. Baik, Highly conductive, printable and stretchable composite films of carbon nanotubes and silver, Nat Nanotechnol 5(12) (2010) 853-857.

[27] Y.P. Mamunya, V.V. Davydenko, P. Pissis, E.V. Lebedev, Electrical and thermal conductivity of polymers filled with metal powders, European Polymer Journal 38(9) (2002) 1887-1897.

[28] Y. Sun, J.A. Rogers, Inorganic semiconductors for flexible electronics, Adv Mater 19(15) (2007) 1897-1916.

[29] A.J. Kell, C. Paquet, O. Mozenson, I. Djavani-Tabrizi, B. Deore, X. Liu, G.P. Lopinski, R. James, K. Hettak, J. Shaker, Versatile molecular silver ink platform for printed flexible electronics, Acs Appl Mater Inter 9(20) (2017) 17226-17237.

[30] D. Li, X. Liu, X. Chen, W.-Y. Lai, W. Huang, A Simple Strategy towards Highly Conductive Silver-Nanowire Inks for Screen-Printed Flexible Transparent Conductive Films and Wearable Energy-Storage Devices, Adv Mater Technol-Us 4(8) (2019) 1900196.

[31] T.S. Tran, N.K. Dutta, N.R. Choudhury, Graphene inks for printed flexible electronics: graphene dispersions, ink formulations, printing techniques and applications, Advances in colloid and interface science 261 (2018) 41-61.

[32] D. Song, A. Mahajan, E.B. Secor, M.C. Hersam, L.F. Francis, C.D. Frisbie, High-resolution transfer printing of graphene lines for fully printed, flexible electronics, Acs Nano 11(7) (2017) 7431-7439.

[33] B. Liang, J. Wei, L. Fang, Q. Cao, T. Tu, X. Ye, High Resolution Direct Writing Liquid Metal Patterns for Printed Stretchable Electronics, 2018 IEEE SENSORS, IEEE, 2018, pp. 1-4.

[34] D.W. Pashley, A study of the deformation and fracture of single-crystal gold films of high strength inside an electron microscope, Proceedings of the Royal Society of London. Series A. Mathematical and Physical Sciences 255(1281) (1960) 218-231.

[35] T. Li, Z. Huang, Z. Xi, S.P. Lacour, S. Wagner, Z. Suo, Delocalizing strain in a thin metal film on a polymer substrate, Mechanics of Materials 37(2-3) (2005) 261-273.

[36] M. George, C. Coupeau, J. Colin, J. Grilhé, Mechanical behaviour of metallic thin films on polymeric substrates and the effect of ion beam assistance on crack propagation, Acta Materialia 53(2) (2005) 411-417.

[37] Y. Xiang, T. Li, Z. Suo, J.J. Vlassak, High ductility of a metal film adherent on a polymer substrate, Appl Phys Lett 87(16) (2005) 161910.

[38] C. Katsarelis, O. Glushko, C. Tonkin, M.S. Kennedy, M.J. Cordill, Crack Initiation of Printed Lines Predicted with Digital Image Correlation, Jom 70(9) (2018) 1805-1810.

[39] A. Wyss, A.S. Sologubenko, N. Mishra, P.A. Gruber, R. Spolenak, Monitoring of stress-strain evolution in thin films by reflection anisotropy spectroscopy and synchrotron X-ray diffraction, Journal of Materials Science 52(11) (2017) 6741-6753.

[40] O. Glushko, A. Klug, E.J.W. List-Kratochvil, M.J. Cordill, Monotonic and cyclic mechanical reliability of metallization lines on polymer substrates, Journal of Materials Research 32(9) (2017) 1760-1769.

[41] B.J. Kim, H.A.S. Shin, J.H. Lee, T.Y. Yang, T. Haas, P. Gruber, I.S. Choi, O. Kraft, Y.C. Joo, Effect of film thickness on the stretchability and fatigue resistance of Cu films on polymer substrates, Journal of Materials Research 29(23) (2014) 2827-2834.

[42] N. Lambricht, T. Pardoen, S. Yunus, Giant stretchability of thin gold films on rough elastomeric substrates, Acta materialia 61(2) (2013) 540-547.

[43] G.D. Sim, S. Won, C.Y. Jin, I. Park, S.B. Lee, J.J. Vlassak, Improving the stretchability of as-deposited Ag coatings on poly-ethylene-terephthalate substrates through use of an acrylic primer, Journal of Applied Physics 109(7) (2011) 5.

[44] N.S. Lu, Z.G. Suo, J.J. Vlassak, The effect of film thickness on the failure strain of polymer-supported metal films, Acta Materialia 58(5) (2010) 1679-1687.

[45] N.S. Lu, X. Wang, Z.G. Suo, J. Vlassak, Failure by simultaneous grain growth, strain localization, and interface debonding in metal films on polymer substrates, Journal of Materials Research 24(2) (2009) 379-385.

[46] N.S. Lu, X. Wang, Z.G. Suo, J. Vlassak, Metal films on polymer substrates stretched beyond 50%, Appl. Phys. Lett. 91(22) (2007) 3.

[47] T. Ibru, K. Kalaitzidou, J.K. Baldwin, A.J.S.m. Antoniou, Stress-induced surface instabilities and defects in thin films sputter deposited on compliant substrates, 13(22) (2017) 4035-4046.

[48] K. Harris, A. Elias, H.-J. Chung, Flexible electronics under strain: a review of mechanical characterization and durability enhancement strategies, J Mater Sci 51(6) (2016) 2771-2805.

[49] O. Kraft, M. Hommel, E. Arzt, X-ray diffraction as a tool to study the mechanical behaviour of thin films, Materials Science and Engineering: A 288(2) (2000) 209-216.

[50] B. Erdem Alaca, M.T.A. Saif, H. Sehitoglu, On the interface debond at the edge of a thin film on a thick substrate, Acta Materialia 50(5) (2002) 1197-1209.

[51] R.M. Niu, G. Liu, C. Wang, G. Zhang, X.D. Ding, J. Sun, Thickness dependent critical strain in submicron Cu films adherent to polymer substrate, Appl Phys Lett 90(16) (2007) 161907.

[52] F. Macionczyk, W. Brückner, Tensile testing of AlCu thin films on polyimide foils, Journal of Applied Physics 86(9) (1999) 4922-4929.

[53] N. Lu, X. Wang, Z. Suo, J. Vlassak, Metal films on polymer substrates stretched beyond 50%, Appl Phys Lett 91(22) (2007) 221909.

[54] Y. Arafat, I. Dutta, R. Panat, Super-stretchable metallic interconnects on polymer with a linear strain of up to 100%, Appl Phys Lett 107(8) (2015) 081906.

[55] S. Yang, E. Ng, N. Lu, Indium Tin Oxide (ITO) serpentine ribbons on soft substrates stretched beyond 100%, Extreme Mechanics Letters 2 (2015) 37-45.

[56] X.-L. Ou, J. Feng, M. Xu, H.-B. Sun, Semitransparent and flexible perovskite solar cell with high visible transmittance based on ultrathin metallic electrodes, Optics Letters 42(10) (2017) 1958-1961.

[57] F.-R. Fan, Z.-Q. Tian, Z.L. Wang, Flexible triboelectric generator, Nano Energy 1(2) (2012) 328-334.

[58] J. Kim, Z. Wang, W.S. Kim, Stretchable RFID for wireless strain sensing with silver nano ink, IEEE Sens. J. 14(12) (2014) 4395-4401.

[59] Y. Khan, M. Garg, Q. Gui, M. Schadt, A. Gaikwad, D. Han, N.A. Yamamoto, P. Hart, R. Welte, W. Wilson, Flexible hybrid electronics: Direct interfacing of soft and hard electronics for wearable health monitoring, Adv Funct Mater 26(47) (2016) 8764-8775.

[60] S. Claramunt, O. Monereo, M. Boix, R. Leghrib, J. Prades, A. Cornet, P. Merino, C. Merino, A. Cirera, Flexible gas sensor array with an embedded heater based on metal decorated carbon nanofibres, Sensors and Actuators B: Chemical 187 (2013) 401-406.

[61] J. Lee, S. Kim, J. Lee, D. Yang, B.C. Park, S. Ryu, I. Park, A stretchable strain sensor based on a metal nanoparticle thin film for human motion detection, Nanoscale 6(20) (2014) 11932-11939.

[62] M. Segev-Bar, H. Haick, Flexible sensors based on nanoparticles, Acs Nano 7(10) (2013) 8366-8378.

[63] R.J. Horwood, Towards a Better Understanding of Screen Print Thickness Control, ElectroComponent Science and Technology 1 (1974) 423186.

[64] D.J. Lipomi, Z. Bao, Stretchable, elastic materials and devices for solar energy conversion, Energ Environ Sci 4(9) (2011) 3314-3328.

[65] A. Almusallam, K. Yang, D. Zhu, R. Torah, J. Tudor, S. Beeby, Development of a low temperature PZT/polymer paste for screen printed flexible electronics applications, SENSORS, 2014 IEEE, IEEE, 2014, pp. 2183-2186.

[66] M. Sumita, K. Sakata, S. Asai, K. Miyasaka, H. Nakagawa, Dispersion of fillers and the electrical conductivity of polymer blends filled with carbon black, Polymer bulletin 25(2) (1991) 265-271.

[67] Y.J. Jung, S. Kar, S. Talapatra, C. Soldano, G. Viswanathan, X. Li, Z. Yao, F.S. Ou, A. Avadhanula, R. Vajtai, Aligned carbon nanotube− polymer hybrid architectures for diverse flexible electronic applications, Nano Lett 6(3) (2006) 413-418.

[68] S. Merilampi, T. Laine-Ma, P. Ruuskanen, The characterization of electrically conductive silver ink patterns on flexible substrates, Microelectronics reliability 49(7) (2009) 782-790.

[69] T. Araki, M. Nogi, K. Suganuma, M. Kogure, O. Kirihara, Printable and stretchable conductive wirings comprising silver flakes and elastomers, IEEE Electron Device Lett. 32(10) (2011) 1424-1426.

[70] Y. Kim, J. Zhu, B. Yeom, M. Di Prima, X. Su, J.-G. Kim, S.J. Yoo, C. Uher, N.A. Kotov, Stretchable nanoparticle conductors with self-organized conductive pathways, Nature 500 (2013) 59.

[71] P. Lall, K. Goyal, B. Leever, S. Miller, Reliability of Additively Printed Traces on Polymer Substrates Subjected to Mechanical Stretching, 2019 18th IEEE Intersociety Conference on Thermal and Thermomechanical Phenomena in Electronic Systems (ITherm), IEEE, 2019, pp. 643-648.

[72] B. Garakani, K.U. Sandakelum Somarathna, D.L. Weerawarne, M.D. Poliks, A. Alizadeh, Reliability of screen-printed conductors and resistors during fatigue cycling on flexible substrate, International Symposium on Microelectronics, International Microelectronics Assembly and Packaging Society, 2019, pp. 000139-000146.

[73] G. Paul, R. Torah, K. Yang, S. Beeby, J. Tudor, An investigation into the durability of screen-printed conductive tracks on textiles, Measurement Science and Technology 25(2) (2014) 025006.

[74] T. Happonen, J. Häkkinen, T. Fabritius, Cyclic bending reliability of silk screen printed silver traces on plastic and paper substrates, IEEE Transactions on Device and Materials Reliability 15(3) (2015) 394-401.

[75] T. Araki, T. Sugahara, M. Nogi, K. Suganuma, Effect of void volume and silver loading on strain response of electrical resistance in silver flakes/polyurethane composite for stretchable conductors, Japanese Journal of Applied Physics 51(11S) (2012) 11PD01.

[76] DuPont, DuPont 5025, 2014.

[77] DuPont, Dupont PE873 Stretchable Silver Conductor, Dupont, 2014, pp. 1-2.

[78] DuPont, Dupont Intexar TE-11C Base Film For Wearables Applications, 2017, pp. 1-2.

[79] L. Scientific, TST350 Temperature Controlled Tensile Stress Testing Stage: User Guide.
https://static1.squarespace.com/static/556d800ae4b0e8f91507450c/t/56cf394886db43237cbed222/1456421216282/TST350_T95_manual.pdf).

[80] G.D. Sim, Y. Hwangbo, H.H. Kim, S.B. Lee, J.J. Vlassak, Fatigue of polymer-supported Ag thin films, Scripta Materialia 66(11) (2012) 915-918.

[81] Y. Leterrier, A. Mottet, N. Bouquet, D. Gilliéron, P. Dumont, A. Pinyol, L. Lalande, J.H. Waller, J.A.E. Månson, Mechanical integrity of thin inorganic coatings on polymer substrates under quasi-static, thermal and fatigue loadings, Thin Solid Films 519(5) (2010) 1729-1737.

[82] J. Blaber, B. Adair, A. Antoniou, Ncorr: Open-Source 2D Digital Image Correlation Matlab Software, Experimental Mechanics 55(6) (2015) 1105-1122.

[83] U. National Institute of Health, ImageJ, in: W. Rasbund (Ed.) Image J, Image Processing and Analysis in Java, Bethesda, MD, pp. Java 1.8.0_112 (64-bit).

[84] O. Glushko, A. Klug, E.J. List-Kratochvil, M.J. Cordill, Monotonic and cyclic mechanical reliability of metallization lines on polymer substrates, arXiv preprint arXiv:1904.04529 (2019).

[85] N. Lu, Z. Suo, J.J. Vlassak, The effect of film thickness on the failure strain of polymer-supported metal films, Acta Materialia 58(5) (2010) 1679-1687.

[86] N. Lu, X. Wang, Z. Suo, J. Vlassak, Failure by simultaneous grain growth, strain localization, and interface debonding in metal films on polymer substrates, Journal of Materials Research 24(2) (2009) 379-385.

[87] G.-D. Sim, S. Won, C.-y. Jin, I. Park, S.-B. Lee, J.J. Vlassak, Improving the stretchability of as-deposited Ag coatings on poly-ethylene-terephthalate substrates through use of an acrylic primer, Journal of Applied Physics 109(7) (2011) 073511.

[88] O. Glushko, P. Kraker, M.J. Cordill, Explicit relationship between electrical and topological degradation of polymer-supported metal films subjected to mechanical loading, Appl Phys Lett 110(19) (2017) 191904.

[89] O. Glushko, B. Putz, M.J. Cordill, Determining effective crack lengths from electrical measurements in polymer-supported thin films, Thin Solid Films 699 (2020) 137906.

[90] C. Brosseau, A. Mdarhri, A. Vidal, Mechanical fatigue and dielectric relaxation of carbon black/polymer composites, Journal of Applied Physics 104(7) (2008) 074105.

[91] N.C. Das, T.K. Chaki, D. Khastgir, Effect of axial stretching on electrical resistivity of short carbon fibre and carbon black filled conductive rubber composites, Polymer International 51(2) (2002) 156-163.

[92] N. Kapur, S.J. Abbott, E.D. Dolden, P.H. Gaskell, Predicting the behavior of screen printing, IEEE Transactions on Components, Packaging and Manufacturing Technology 3(3) (2013) 508-515.